



City Research Online

City, University of London Institutional Repository

Citation: Hashim, Z. Q. (2019). A bioimpedance - based re-configurable electrode method for early detection of arteriosclerosis indicators. (Unpublished Doctoral thesis, City, University of London)

This is the accepted version of the paper.

This version of the publication may differ from the final published version.

Permanent repository link: <https://openaccess.city.ac.uk/id/eprint/24878/>

Link to published version:

Copyright: City Research Online aims to make research outputs of City, University of London available to a wider audience. Copyright and Moral Rights remain with the author(s) and/or copyright holders. URLs from City Research Online may be freely distributed and linked to.

Reuse: Copies of full items can be used for personal research or study, educational, or not-for-profit purposes without prior permission or charge. Provided that the authors, title and full bibliographic details are credited, a hyperlink and/or URL is given for the original metadata page and the content is not changed in any way.

A bioimpedance - based re-configurable electrode method for early detection of arteriosclerosis indicators

Zaheer Q. Hashim

This dissertation is submitted for the degree of
Doctor of Philosophy



City, University of London

School of Mathematics, Computer Science and Engineering

Research Centre for Biomedical Engineering

November 2019

Contents

| | |
|--|--------------|
| Contents | ii |
| List of Figures | vii |
| List of Tables | xi |
| Acknowledgements | xiii |
| Declaration | xv |
| Abstract | xvi |
| Glossaries | xviii |
| List of Publications | 1 |
| 1 Introduction | 2 |
| 1.1 Motivation | 5 |
| 1.2 Aims and Objectives | 6 |
| 1.3 Novelty | 7 |
| 1.4 Thesis Structure | 8 |
| 2 Background Theory | 10 |
| 2.1 Circulatory System and Associated Medical Conditions | 10 |
| 2.1.1 Circulatory System Biology | 10 |
| 2.1.2 Circulatory System Medical Conditions | 12 |

| | | |
|----------|---|-----------|
| 2.2 | Diagnostic Methods for Circulatory Conditions | 13 |
| 2.3 | Bio-impedance Principles, Diagnosis Systems & Methods | 22 |
| 2.3.1 | Fundamental Bio-impedance Principles | 22 |
| 2.3.2 | Methods | 25 |
| 2.3.3 | Clinical Applications | 29 |
| 2.3.4 | Commercially Available Systems | 30 |
| 2.4 | Bio-potential Electrodes and Topologies | 32 |
| 2.4.1 | Bio-potential Electrodes | 32 |
| 2.4.2 | Electrode Topologies | 39 |
| 2.5 | Multi-electrode Arrays | 42 |
| 2.6 | (Experimental and Simulatory) Biological Models | 44 |
| 2.6.1 | Finite Element Modelling (FEM) | 44 |
| 2.6.2 | Phantoms | 45 |
| 2.7 | Conclusion | 48 |
| 3 | Dynamically Re-sizeable Electrodes (DRE) | 49 |
| 3.1 | Method | 49 |
| 3.2 | Geometric Model Parameters | 51 |
| 3.2.1 | Initial Model | 51 |
| 3.2.2 | Final Model | 52 |
| 3.2.3 | Tissue Parameters | 53 |
| 3.3 | Electrode Design | 55 |
| 3.4 | Lumped-impedance Simplified Representation | 55 |
| 3.5 | SSVT scanning Sequence and Localised Measurements | 59 |
| 3.6 | FEM Simulations | 60 |
| 3.7 | Experimental Setup | 62 |
| 3.7.1 | Circuit Design | 62 |
| 3.7.2 | Micro-controller Program | 64 |
| 3.7.3 | Impedance Analyser Setup | 65 |
| 3.7.4 | Data Acquisition Program | 66 |

| | | |
|----------|--|-----------|
| 3.7.5 | Gelatin Phantom Design and Manufacturing | 67 |
| 3.7.6 | Experimental Procedure | 68 |
| 3.8 | RESULTS AND DISCUSSION | 69 |
| 3.8.1 | Initial Model Results | 69 |
| 3.8.2 | Research Question (1): Segment Identification | 69 |
| 3.8.3 | Research Question (2): Measurement Sensitivity | 77 |
| 3.9 | Conclusion | 79 |
| 4 | Intelligent Re-configurable Electrode Method (IREM) Simulation | 81 |
| 4.1 | Method | 82 |
| 4.2 | Electrical Impedance Calculation in Simulation | 85 |
| 4.3 | Stage 1: Simplified Design | 85 |
| 4.3.1 | Intelligent Re-configurable Electrode Method (IREM) Pixelated MEA Setup for Model A | 85 |
| 4.3.2 | Localised Impedance Simulation. | 86 |
| 4.3.3 | Results: Model A | 87 |
| 4.4 | Stage 2: Parameter Identification | 89 |
| 4.4.1 | Simulation Setup | 89 |
| 4.4.2 | Detection of Vessels at Different Depths | 91 |
| 4.4.3 | Detection of Vessel with Varying Vessel Thickness | 91 |
| 4.4.4 | Changing Electrode Size with Fixed Centre to Centre Spacing | 92 |
| 4.4.5 | Changing Electrode Size with Fixed Edge To Edge Spacing | 92 |
| 4.4.6 | Changing electrode spacing with fixed electrode size | 93 |
| 4.4.7 | Localised Measurements with Different Electrode Grouping and positioning | 93 |
| 4.4.8 | Results: Model B | 95 |
| 4.5 | Stage 3: 2D Simulation | 103 |
| 4.5.1 | 2D Model Setup | 103 |
| 4.5.2 | 2D simulation results | 104 |
| 4.6 | Stage 4: Main Model Setup | 108 |

| | | |
|----------|--|------------|
| 4.6.1 | Single Pixel Variable Tetrapole (SPVT) Scanning Sequence | 108 |
| 4.6.2 | Image Analysis and Feature Recognition | 111 |
| 4.7 | Simulation Procedure | 113 |
| 4.7.1 | Parameters Variations | 113 |
| 4.7.2 | Expanded Bifurcation Model | 114 |
| 4.7.3 | Main Model: Identification of Vessel Orientation | 115 |
| 4.7.4 | Main Model: Vessel Detection at different Depth | 116 |
| 4.7.5 | Main Model: Feature Detection | 117 |
| 4.8 | Discussion | 121 |
| 4.9 | Conclusion | 122 |
| 5 | IREM Experimental verification and Flow Measurements | 123 |
| 5.1 | Method | 124 |
| 5.2 | IREM Block Diagram | 124 |
| 5.3 | IREM Circuit Design | 125 |
| 5.3.1 | Electrode Array | 129 |
| 5.3.2 | Micro-controller Program | 129 |
| 5.3.3 | CPLD Program | 133 |
| 5.3.4 | Full Automation | 135 |
| 5.4 | Experimental Setup | 136 |
| 5.5 | Phantom Design | 137 |
| 5.6 | Flow Experiment Setup | 138 |
| 5.7 | Flow Phantom Design | 139 |
| 5.7.1 | Impedance Analyzer Setup | 139 |
| 5.7.2 | Data Acquisition Program | 140 |
| 5.8 | Experimental Procedure | 140 |
| 5.9 | Flow Experiment Procedure | 141 |
| 5.10 | Results and Discussion | 143 |
| 5.10.1 | IREM Scanning Sequence | 143 |
| 5.10.2 | Flow Parameter Variation | 144 |

| | |
|--|------------|
| 5.11 Conclusion | 147 |
| 6 Using IREM for Occlusion Detection | 148 |
| 6.1 Occlusion Study Method | 149 |
| 6.2 Occlusion Scanning Simulation | 149 |
| 6.3 Occluded Flow Phantom Design | 150 |
| 6.4 Occluded Flow Experimental Procedure | 151 |
| 6.5 Results and Discussion | 151 |
| 6.5.1 Detection of Occlusion | 151 |
| 6.5.2 Occlusion flow Study | 153 |
| 6.6 Conclusion | 155 |
| 7 Conclusion And Future Work | 156 |
| 7.1 Conclusion | 156 |
| 7.2 Future work | 159 |
| Bibliography | 160 |
| A Appendix A | 173 |
| B Appendix B | 179 |
| B.1 MATLAB programs | 179 |
| B.1.1 LCR Data Accusation Program | 179 |
| B.1.2 Prototype 1 Scan Program | 180 |
| B.1.3 Pre-programmed sequence | 180 |
| B.1.4 Full Automation | 185 |
| B.1.5 Sending function | 188 |
| B.1.6 Coordinate Scan Function | 216 |
| B.1.7 LCR meter connection function | 218 |
| B.1.8 LCR meter disconnection function | 218 |
| B.1.9 Image estimation function | 219 |

List of Figures

| | | |
|------|---|----|
| 1.1 | Ischemic stroke. | 3 |
| 2.1 | Blood vessel structure | 11 |
| 2.2 | Carotid Ultrasonography implementation and results | 15 |
| 2.3 | CT scanner | 16 |
| 2.4 | MRI scanner | 17 |
| 2.5 | Placement of PPG sensor | 18 |
| 2.6 | Impedance plethysmography electrode placement | 20 |
| 2.7 | Current paths through tissue | 23 |
| 2.8 | Electrical model of cell membrane | 23 |
| 2.9 | Frequency dispersion | 24 |
| 2.10 | EIT electrode placement | 26 |
| 2.11 | Current injection and voltage measurement in EIT | 27 |
| 2.12 | EIT measurement and simple imaging procedure | 28 |
| 2.13 | Electrode/electrolyte interface | 33 |
| 2.14 | Measured voltage ΔV with six different electrode metals | 35 |
| 2.15 | Compound electrodes | 37 |
| 2.16 | Electrodes with varying size | 38 |
| 2.17 | Electrodes with varying spacing | 38 |
| 2.18 | Bi-polar topology | 39 |
| 2.19 | Tri-polar topology | 40 |
| 2.20 | Tetra-polar topology | 41 |

| | | |
|------|--|----|
| 2.21 | Simplified sensitivity distribution | 41 |
| 2.22 | Multi-electrode arrays | 43 |
| 3.1 | Simplified diagram showing the positioning of electrodes | 50 |
| 3.2 | Initial model top view | 52 |
| 3.3 | Overall dimensions for 3D simulation model | 53 |
| 3.4 | Model parameter overview | 54 |
| 3.5 | Simplified lumped impedance model | 57 |
| 3.6 | DRE block diagram and circuit diagram | 63 |
| 3.7 | DRE Gelatin phantom | 67 |
| 3.8 | Conductivity variation with varying electrode lengths(ℓ_e) | 70 |
| 3.9 | Scaling and Normalising data | 71 |
| 3.10 | Blood vessel detection process (simulation data) | 73 |
| 3.11 | Blood vessel detection process (simulation data) | 74 |
| 3.12 | Blood vessel detection process (experimental data) | 75 |
| 3.13 | Scan result plotted against electrode segments used to obtain results for detecting electrode segments overlapping the blood vessel | 75 |
| 3.14 | SSVT orientation ϕ vs the scaled normalized data | 76 |
| 3.15 | Conductivity vs impedance plot for Stripe vs pseudo-stripe electrodes . . | 78 |
| 3.16 | Conductivity vs impedance plot | 79 |
| 4.1 | Model A with IREM array, and localised electrode configuration | 86 |
| 4.2 | Model A: impedance scan plot | 88 |
| 4.3 | Model A: comparison of tetrapolar configurations | 89 |
| 4.4 | Model B setup | 90 |
| 4.5 | Model B: relative position of blood vessel from skin layer | 91 |
| 4.6 | Model B: relative thickness of the blood vessel | 92 |
| 4.7 | Model B: variation of electrode diameter fixed centre to centre spacing . . | 92 |
| 4.8 | Model B: variation of electrode diameter fixed edge spacing | 93 |
| 4.9 | Model B: localised measurements taken using single electrodes | 94 |

| | |
|--|-----|
| 4.10 Model B: localised measurements taken using two electrodes diagonally grouped together | 95 |
| 4.11 Model B: localised measurements taken using four electrodes grouped to- gether | 96 |
| 4.12 Model B: vessel detection at different depths | 97 |
| 4.13 Model B: impedance measurements for different vessel diameters at a fixed depth of 3 <i>mm</i> | 97 |
| 4.14 Model B: changing electrode size with a fixed centre to centre spacing . . | 98 |
| 4.15 Model B: changing electrode size with fixed edge to edge spacing | 99 |
| 4.16 Model B: changing electrode spacing with fixed electrode size | 100 |
| 4.17 Model B: localised impedance measurements with single electrodes at dif- ferent positions | 101 |
| 4.18 Model B: localised impedance measurements with diagonally grouped at different positions | 102 |
| 4.19 Model B: localised impedance measurements with four electrode groups at different positions | 102 |
| 4.20 2D simulation model | 104 |
| 4.21 2D Simulation parallel electrode configuration results. | 106 |
| 4.22 2D Simulation perpendicular electrode configuration results. | 107 |
| 4.23 Main model setup | 109 |
| 4.24 Single pixel variable tetrapole scanning sequence | 110 |
| 4.25 Expanded bifurcation model | 115 |
| 4.26 Main model: 3D simulation Vessel detection | 116 |
| 4.27 Main model: simulation vessel boundaries | 117 |
| 4.28 Main model: bifurcation vessel detection | 119 |
| 4.29 Expanded bifurcation model: expanded array bifurcation vessel detection | 120 |
| 5.1 IREM block diagram | 126 |
| 5.2 IREM circuit design | 127 |
| 5.3 Phantom positioning over the electrode array used for experimentation . | 129 |

| | | |
|------|--|-----|
| 5.4 | Flow chart for the micro-controller program | 132 |
| 5.5 | Program for first cycle of switching program | 133 |
| 5.6 | Design for the serial to parallel converter | 134 |
| 5.7 | Relation between impedance and temperature over time | 142 |
| 5.8 | Localised electrode groupings for flow study | 142 |
| 5.9 | IREM experiment scan result | 143 |
| 5.10 | Pressure vs impedance measurement | 145 |
| 5.11 | Single pulse after averaging multiple pulses | 146 |
| 5.12 | Variation of SV and BPM | 146 |
| 6.1 | Expanded model: Occlusion positioning | 150 |
| 6.2 | 3D simulation: 20% occlusion scan result after processing | 152 |
| 6.3 | 3D simulation: 20% occlusion scan result after processing in a bifurcation | 153 |
| 6.4 | Flow study with occlusion | 154 |
| 6.5 | Ratio of two peaks with the dicrotic notch | 154 |
| A.1 | Prototype 1 DRE electrode circuit design | 174 |
| A.2 | Prototype 1 DRE user interface board circuit design | 174 |
| A.3 | Design for CPLD program. | 175 |
| A.4 | IREM prototype 3 daughter board circuit design | 176 |
| A.5 | IREM prototype 2 circuit design | 177 |
| A.6 | IREM prototype 3 father board circuit design | 178 |

List of Tables

| | | |
|-----|---|-----|
| 2.1 | Diagnostic method comparison | 21 |
| 2.2 | Commercially available systems | 32 |
| 2.3 | Electronic Conductor Materials | 35 |
| 2.4 | Some MEA applications and uses | 44 |
| 3.1 | Different layers and their conductivity and concentration | 68 |
| 3.2 | Expected segments vs identified segments | 76 |
| 4.1 | Summary of different simulation stages | 84 |
| 4.2 | Orientation extracted with respect to the actual | 115 |
| 4.3 | Model B: vessel diameter actual vs measured | 117 |
| 5.1 | NaCl Concentration | 137 |
| 5.2 | New NaCl Concentration | 139 |
| 5.3 | Blood vessel Orientation, expected vs measured | 144 |
| 6.1 | Circumference of tube and the occlusions | 151 |
| 6.2 | Actual versus measured occlusion percentage in a straight line vessel . . . | 152 |
| 6.3 | Actual versus measured occlusion percentage in a bifurcation | 153 |

Acknowledgements

First and foremost, I would like to thank God for providing me with this wonderful opportunity to carry out this research.

I would like to express my greatest thanks to Dr. Iasonas F. Triantis, my supervisor, for the guidance, the support, the knowledge, the collaboration and the friendship throughout my PhD. I am grateful for all of these and for his very important contribution to the work done in this project.

I would also like to express my thanks and appreciation to Prof. Panayiotis A. Kyriacou, my second supervisor, for the guidance, the support, the knowledge, the collaboration and the friendship throughout my PhD.

I would like to thank Prof. Panayiotis Liatsis for his help in developing the image analysis program.

I would like to thank Dr. Loukas Constantinou, Dr. Enayetur Rahman, Dr. José Alonso Solis Lemus, and Dr. Mohammad Mamouei for the guidance and knowledge they provided during my PhD.

I would like to thank my parents for their guidance and support throughout my life, and encouraging me in all my endeavours. I would like to thank Jasim, my elder brother, for his support throughout my academic career. I would also like to thank my aunt Yasmin, for providing me with living accommodations.

I would like to thank in alphabetical order, Aishwari, Azmeena, Nayab and Nystha by best friends, for their support and encouragement. I want to say a huge thank you for being there for me and supporting my effort through the tough times.

I would like to thank my colleagues and good friends from the research centre for

biomedical engineering (RCBE) for their good company during relaxing coffee breaks accompanied with our strictly technical and scientific conversations.

Declaration

I hereby declare that the work presented in this thesis is my own work. Any idea, result, or illustration originating from other subjects work has been acknowledged in the text by referencing to the original author. This thesis has never been published or submitted elsewhere for obtaining an academic degree or professional qualification. This dissertation is my own work and contains nothing which is the outcome of work done in collaboration with others, except as specified in the text and Acknowledgements.

I grant power of discretion to the Librarian at City, University of London to allow the thesis to be copied in whole or in part without further reference. This permission covers only single copies made for study purposes, subject to normal conditions of acknowledgement.

Zaheer Q. Hashim

November 2019

Abstract

Arteriosclerosis is a medical condition that is associated with the stiffening of arteries due to the loss of elasticity as a result of ageing and is often asymptomatic. It occurs in almost every person and can lead to life-threatening diseases, including heart attacks and strokes. Approximately 50% of all stroke cases world-wide result from asymptomatic atherosclerosis - a type of arteriosclerosis - of the carotid artery. The standard non-invasive methods for detection of atherosclerosis are ultrasonography, computed tomography and magnetic resonance imaging. Only confirmed symptomatic cases are referred for such examinations. This is because these methods are either expensive, heavily operator dependent, not always accurately handled, potentially harmful, significantly cumbersome, or only available at well-equipped medical centres. Therefore, there is a need for routine screening of major arteries like the carotid artery. Doing so might help identify potentially millions of cases that are either asymptomatic or symptomatic patients in rural areas or who are poor. This thesis describes how bio-impedance can overcome the limitations of the aforementioned methods - without attempting to replace them in terms of clinical validity or accuracy - to eventually provide indicative outcomes for routine screening that would allow even asymptomatic patients to be referred for further clinical assessment if needed. Work done includes the design, implementation and evaluation, through idealised FEM simulations and phantom experiments, of a bio-impedance-based re-configurable electrode method for early detection of arteriosclerosis indicators. It utilises impedance measurements taken from an array of electrodes by means of a novel scanning method, to transcutaneously detect vascular structures as well as vascular occlusions. It also explores the possibility of grouping multiple small

electrodes to form re-configurable electrodes, in terms of size, shape and position. The results from simulations and experiments demonstrate that the proposed scanning method can overcome the need for accurate electrode placement by identifying vessel orientation and features and by selecting the electrode that are more relevant to the targeted vascular structure with high accuracy. The results also show that the resulting localised electrodes exhibit approximately 25% improved sensitivity when compared to conventional electrodes. It was also confirmed that occlusions could be detected both through area scans with an accuracy of 98% as well as through localised flow measurements.

Glossaries

| | |
|--------------|---|
| α | alpha |
| β | beta |
| ℓ_e | Length of electrode |
| ℓ_m | Length of model |
| ℓ_t | Length of tetrapole |
| ϵ_r | Relative permittivity |
| γ | gamma |
| Ω | measure of resistance |
| σ | Conductivity |
| h_m | Height of model |
| J'_{cc} | Current density fields when injecting current using CC electrodes |
| J'_{reci} | Current density fields when injecting current using PU electrodes |
| S/m | Measure of electric conductance |
| w_e | Width of electrode |

| | |
|---------|------------------------------------|
| w_m | Width of model |
| AC | Alternating current |
| ACG | Admittance cardiography |
| ACT | Adaptive current tomography |
| Ag/AgCl | Silver/silver chloride |
| ATE | Artificial tissue emulating |
| ATE | artificial tissue emulating |
| BIS | Bio-impedance spectroscopy |
| BP | Blood pressure |
| BPM | Beats per minute |
| CC | Current carrying/injection |
| CEMRA | Contrast enhanced MRA |
| CLK | Clock |
| CO | Cardiac output |
| CPLD | Complex programmable logic device |
| CTA | Computed tomography angiography |
| CVA | Cerebrovascular accident |
| DC | Direct current |
| DIP | Dual inline package |
| DRE | Dynamically re-sizeable electrodes |
| EIS | Electrical impedance spectroscopy |

| | |
|------|--|
| EIT | Electrical impedance tomography |
| FEM | Finite element modelling |
| IC | Integrated circuit |
| ICG | Impedance cardiography |
| IPG | Impedance plethysmography |
| IREM | Intelligent Re-configurable Electrode Method |
| IS | Impedance spectroscopy |
| MEA | Multi-electrode array |
| MRA | Magnetic resonance angiography |
| MRI | Magnetic resonance imaging |
| MUX | Multiplexer |
| PB | Push button |
| PCB | Printed circuit board |
| PPG | Photo plethysmography |
| PU | Pick up |
| SDI | Serial data input |
| SNR | Signal to noise ratio |
| SPI | Serial peripheral interface |
| SPVT | Single pixel variable tetrapole |
| SSVT | Single segment variable tetrapole |
| SV | Stroke volume |

| | |
|---------|---|
| TOF-MRA | Time of flight MRA |
| UART | Universal asynchronous receiver transmitter |
| US | Ultrasonography |

List of Publications

The academic contributions made during the time this research was carried out are listed below:

Journal Publications

- Z. Q. Hashim, L. Constantinou, and I. F. Triantis, "Modelling dynamically re-sizeable electrodes (DRE) for targeted transcutaneous measurements in impedance plethysmography" Transactions in Biomedical Circuits and Systems (TBioCAS), (Accepted for publication).
- Z. Q. Hashim, P. Liatsis, E. Rahman, P.A. Kyriacou and I. F. Triantis, "A bioimpedance method to allow frequent screening for carotid atherosclerosis using FEM and gelatin phantom models" Transactions in Biomedical Circuits and Systems (TBioCAS), (Submitted for publication).

Conference Publications

- Z. Q. Hashim, L. Constantinou, P. A. Kyriacou, and I. F. Triantis, A novel approach to transcutaneous localization of blood vessels using a dynamically reconfigurable electrode (DRE) array, Biomedical Circuits and Systems Conference (BioCAS), 2016 IEEE, vol. 44, pp. 424427, 2016.

Chapter 1

Introduction

Arteriosclerosis is an age-related medical condition that occurs in everyone but rarely causes any symptoms [1]. It refers to diseases that affect the arteries that lead to them losing their elasticity causing their physical properties to change, which can occur in any artery in the body. Arteriosclerosis can lead to some life-threatening complications, for example, kidney disease, high blood pressure, coronary heart disease, coronary thrombosis and stroke [1]. Stroke, in particular, is one of the leading causes of death and severe disability worldwide [2], with about 15 million people suffering from strokes annually around the world. Of these cases, 63% are caused by a type of arteriosclerosis, namely atherosclerosis [3] occurring in the carotid artery. Atherosclerosis is a degenerative disease, involving masses of cholesterol that accumulate on the artery wall, narrowing its lumen [4, 5, 6]. At times the accumulation can rupture, causing clots to form, which can then break off and block smaller arteries in the brain leading to strokes, as shown in figure 1.1. Although carotid atherosclerosis can become symptomatic - mostly in people over 40 years of age - it is very often asymptomatic [7]. More specifically, approximately 80% of atherosclerosis-related stroke cases are asymptomatic. In addition to these patients, there are a lot of people around the world that even with symptoms don't have access to any diagnostic facility, either because these regions are remote or because they are poor [8, 9, 10]. Further to these cases, there is also evidence that early detection of atherosclerosis can save lives [3]. All of these factors indicate that routine checks should

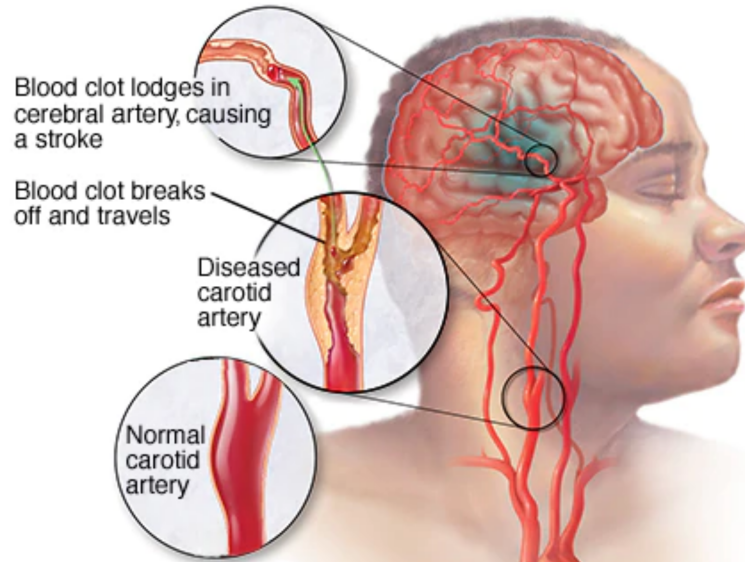


Figure 1.1: Ischemic stroke. A diseased carotid artery and cause of stroke are shown (figure from [11])

be part of mainstream medical practice, if there was a diagnostic method that would allow for this.

The standard methods most often used for detection of arteriosclerosis include ultrasonography (US), computed tomography (CT) and magnetic resonance imaging (MRI). To date, the non-invasive gold standard for detecting and monitoring carotid atherosclerosis, once symptoms appear, is ultrasound (or ultrasonography) (US). Detection is done by monitoring two factors, the morphology of the artery lumen and the plethysmographic profile, both of which are obtained from the same hand-held sensor [3]. US, is quick, non-invasive and has measurement accuracy greater than 90% [3, 12, 13]. However, it is only implemented when symptoms arise, because it is bulky and operator dependent, hence it requires the operator to have proper training, after which the maximum accuracy obtained is still around 76% to 83% [13, 14]. The requirement of a trained operator restricts its availability making it expensive, albeit not as expensive as CT and MRI. CT, offers excellent spatial resolution, superior contrast resolution and speed. It is relatively operator-independent and also allows the measurement of the size of the stenosis, making it the most desirable method for diagnosis. Still, this method is expensive to implement, only takes static measurements, exposes the patient to radiation and

uses iodine as contrast medium intravenously, limiting the frequency of implementation [12, 15, 16]. MRI, has reproducibility, good sensitivity, not heavily operator dependent, and uses no radiation. However, it is expensive to implement, bulky, not readily available, and cannot be implemented on all patients. [17]. Either because they are expensive, heavily operator dependent, not very accurate, can be harmful to patients, extremely bulky and cumbersome, only well-equipped medical centres have these methods available and only confirmed symptomatic cases are referred for such examinations. However, this is potentially costing the lives to millions of people that belong to the three categories mentioned earlier, i.e. people that can't get access to these expensive settings, or that could be saved if early detection was possible. Therefore, it is desirable to have a cheap, non-harmful, operator-independent, compact system that would give an indication to identify patients that require to be further assessed and could be used as part of routine checks for early detection. Such a system should be available at every general practitioner (GP) or medical practice or even available to private individuals. It can also be used in areas where medical facilities are not that advanced. With such a system in place and therefore, routine tests on all patients that visit a doctor, up to 80% of the 15 million cases worldwide [3] can be detected early and treated. Therefore, this system would have the potential to save up to 12 million lives annually.

Measuring the electrical impedance of biological tissue also known as Bio-impedance spectroscopy (BIS) or electrical impedance spectroscopy (EIS) or when used for imaging electrical impedance tomography (EIT), has the potential to be used as the diagnostic method that fits the above criteria. This method is non-invasive, easy to implement, inexpensive, quick, and uses non-ionizing radiation, making it safe to use continuously [18]. It has been used to take plethysmographic measurements to monitor cardiac output and also to detect the pulsatile flow of blood in limbs [19, 20, 21]. It has also been used to take tomographic measurements for monitoring inflation of the lungs during mechanically aided respiration [22, 23, 24]. Impedance measurements have also shown potential in mapping the area of wounds in chronic ulcers in diabetic patients [25]. There have been simulation studies showing detection of atherosclerotic plaque by taking impedance measurements along the blood vessel [26]. However, taking impedance plethysmographic

measurements for a specific artery requires the measurement electrodes to be positioned over the artery of interest with a specific spacing between the electrodes [27]. EIT measurements, on the other hand, are mostly taken across the thorax for monitoring lung inflation, there has yet to be any studies showing the use of EIT for observing the morphology of the blood vessel.

Therefore, there is a need for a method or a device that has electrodes that can be accurately placed on the site of interest, which then scans the area, detects the artery and checks the morphology of the artery. It then take focused plethysmographic measurements from the desired artery to look at the flow profile to identify occlusions. This thesis describes how bio-impedance can overcome the limitations of the aforementioned methods - without attempting to replace them in terms of clinical validity or accuracy - to eventually provide indicative outcomes for routine screening that would allow even asymptomatic patients to be refereed for further clinical assessment if needed. This work uses two indicators for detection of atherosclerosis: one is the variation of the form of the plethysmographic signal, and the other is the change in the morphology of the artery. The change in the morphology is assessed through impedance measurements, taken from an array of electrodes employing a unique scanning method, to detect vascular structures as well as vascular occlusions transcutaneously. This research will also explore the possibility of grouping multiple small electrodes to form an electrode of a larger effective area. The possibility of using impedance measurements as an early detection system will be tested through: simulations and experiments on specific scenarios using custom models, phantoms, and circuitry.

1.1 Motivation

Due to the silent nature of arteriosclerosis and its associated life-threatening diseases, there is a need for routine screening of major arteries like the carotid artery. Doing so might help identify potentially millions of cases that are either asymptomatic or symptomatic patients in rural areas or who are poor. However, these needs are not being met by the current diagnostic methods. This is because they are either: expensive or

heavily operator dependent or not very accurate or can be harmful to patients or extremely bulky and cumbersome. In consequence, only well-equipped medical centres have these methods and only confirmed symptomatic cases get referred for such examinations. Therefore, there is a need for a rapid, potentially inexpensive, safe and operator-independent diagnostic method, which will ultimately allow for frequent routine tests to be carried out. Such a method will allow for the diagnosis of asymptomatic cases and eventually for the early diagnosis of carotid atherosclerosis. Early diagnosis can lead to medical intervention towards lifestyle alterations such as dietary changes and exercise or surgical intervention where needed, to monitor or better control the progression of arteriosclerosis related diseases.

1.2 Aims and Objectives

This thesis aims to develop and assess the merits of a method that makes it possible for electrodes to be reconfigured automatically. This will allow electrodes to be localised only to the vessels of interest, taking measurements that are relevant to indicators of arteriosclerosis. There were two main objectives; to assess it through simulations and to assess a part of it experimentally.

For assessing the method experimentally the following sub-objectives needed to be accomplished:

- Design and develop an addressing system that interfaces between the impedance measurement circuitry and an electrode array.
- Design the addressing system to have the ability to control each electrode in the array.
- Allocate multiple electrodes to act as a single electrode.
- Program the system so it changes the size, spacing, position and topology of the electrodes automatically without the need for manually replacing or re-positioning the electrodes used.

- Build phantoms matching the simulations models to assess the addressing system.
- Build phantoms to incorporating flow to assess localised measurements taken using the addressing system.

For assessing the method through simulations the following sub-objectives needed to be accomplished:

- Conduct finite element modelling simulations that would compare different electrode configurations.
- Look at idealised biological models.
- Identify the electrical properties of tissue to be used in simulations.
- Assess the method to identify features of the vascular structure such as orientation and bifurcations in simulations.
- Identify occlusions in the vascular structure including in bifurcations.
- Take localised measurements such as flow rate of blood and possibly the pressure variations due to occlusion.

1.3 Novelty

1. According to literature [19, 28, 29, 30], bioimpedance electrodes that are localised relative to a targeted structure have been shown to achieve better results than electrodes that cover a large area. However, these electrodes need to be manually positioned on the vascular area of interest, and the electrodes are not cut to size. Here for the first time, a method is presented whereby independent of the manual placement of the electrode array on top of the skin over the vascular structure. This method can automatically locate the structure of interest, then identify appropriate electrode size and spacing, and tailor-cut electrodes to fit precisely over the vesicular structure. Results from tailor-cut electrodes show better sensitivity than larger localised electrodes.

2. This work presents a novel way of utilising multi-electrode arrays to form larger "effective" electrodes whose geometry and size can be automatically re-configured to adapt to a targeted structure.
3. Using such effective electrodes to form tetrapoles for impedance measurements allows for an additional novelty: adjusting both the location of each electrode and the distance between them without having to physically relocate them.
4. While tomography typically involves electrodes surrounding an targeted volume, here a novel tetrapolar surface or planar mapping method is presented that overlays four different scanning orientations to achieve a better resolution.
5. This thesis utilises the above methods for a novel application; namely imaging vascular structures using impedance measurements, including identification of occlusions and vascular characteristics such as bifurcations.
6. Finally, the hardware design and implementation of the above points resulted to a novel system that can perform automatic reconfiguration of electrode arrays to allow for re-sizeable, re-locating and re-shaping electrodes for bioimpedance planar mapping and localised bioimpedance measurements.

1.4 Thesis Structure

In chapter 2, the physiology of vascular structures, some of the diseases associated with them, most commonly used diagnostic methods, introduction to impedance measurements and its clinical applications are explained. Bio-potential electrodes and their topologies are also discussed along with multi-electrode arrays and different ways to model biology. Chapter 3, explores the use of a simplified scan to identify electrodes positioned over a vascular structure. This chapter also assesses the influence of impedance measurements taken using different electrode geometries. Chapter 4 explores, through simulations, the use of multi-electrode arrays for locating vascular structures and identifying their features. Chapter 5 presents the design of a custom circuitry for experimental

verification of results obtained in chapter 4 as well as flow measurements using localised electrodes. Chapter 6 further explores the scanning and localisation features to identify occlusions in vascular structures. The results and conclusions associated with each approach are shown in their respective chapters. Chapter 7 provides the general conclusions of the thesis and future work.

Chapter 2

Background Theory

This chapter briefly touches on the relevant theory that this thesis uses to make assumptions and decisions based on the previous work carried out in this field.

2.1 Circulatory System and Associated Medical Conditions

2.1.1 Circulatory System Biology

The cardiovascular system plays a vital role in the body. It transports blood to and from the heart, allowing the transfer of gasses and nutrients in blood to the surrounding tissues. The waste material and carbon dioxide from the tissues is defused into the blood, which transports it to the relevant organs for excretion. It is also responsible for thermoregulation, acid-base balance and protection against diseases [5, 6, 4, 31]. The cardiovascular system consists of the heart, the arteries, the arteriole, the capillaries, the venules and the veins. The heart is the central pump and the main motor in this system. Arteries are made up of three layers: (1) the tunica interna: an endothelium layer, (2) the tunica media: a thick middle layer comprising of smooth muscles and elastic fibres, (3) the tunica externa: consisting of elastic and collagen fibres. The main purpose of arteries is transporting blood away from the heart. The muscle and elastic fibres allow for the artery to expand and recoil. When the heart contracts, blood is pumped out,

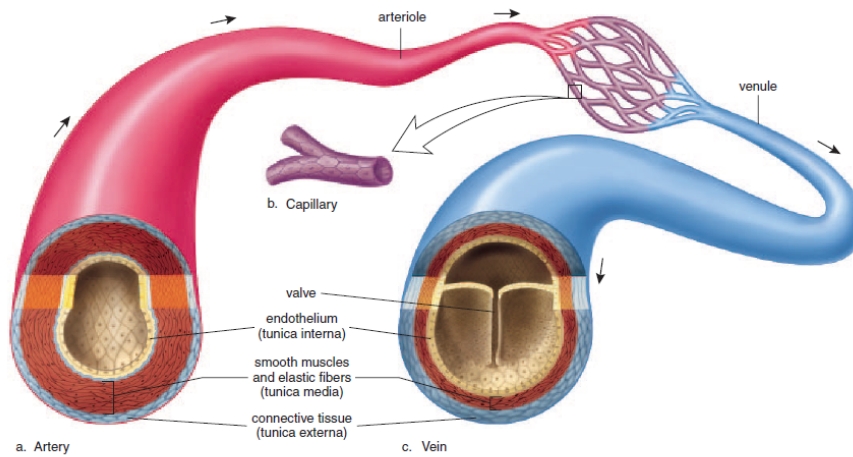


Figure 2.1: Blood vessel structure. The three layers of the artery and vein are displayed. The tunica interna is the endothelium layer; the tunica media is the elastic fibres and smooth muscle tissues; the tunica externa is composed of connective tissue. a. Arteries have a thicker wall than veins because they have a thicker middle layer than veins; this is to maintain BP. b. Capillary walls are one-cell-thick endothelium, enabling gas and material exchange to take place. c. Veins are larger in diameter than arteries. [6]

and the artery expands. When the heart is at rest, the artery recoils, allowing blood to flow at high velocity to the rest of the body. The middle layer of these vessels contain some elastic tissue and mostly smooth muscles. The lumen (cavity) of the arteriole decreases or expands as muscle fibres contract or relax, affecting blood distribution and blood pressure. Arterioles further split into capillaries. These microscopic vessels have a single-layered wall comprising of endothelial cells which makes it possible for the exchange of nutrients and gases to take place. Venules drain blood from the capillaries, then join together to form veins which carry de-oxygenated blood back to the heart. Veins also have three layers, similar to arteries; however, they are much thinner than that of arteries because the middle layer contains less muscle and elastic fibres. Figure 2.1 shows the wall structure of the arteries and veins, also depicting the connection between them.

The circulation of blood in this vascular network is usually measured using two defined parameters: (1) Cardiac output (CO) is the volume of blood pumped out of the heart over a defined period time, (2) Stroke Volume (SV) is the amount of blood pumped out of the heart per contraction. CO is calculated by using the formula below

2.1 [4].

$$CO = SV \times Heartbeat/min \quad (2.1)$$

The parameters mentioned above reflects the working conditions of the circulatory system and help identify any abnormalities.

2.1.2 Circulatory System Medical Conditions

The circulatory system is vital for normal functioning of the body. However, it can be affected by abnormalities or medical conditions, arteriosclerosis being one of them. Arteriosclerosis, commonly known as "hardening of the arteries", it is a term used to collectively identify diseases that affect arteries causing them to lose their elasticity and causes physical properties of the artery to change [4, 5, 6]. It occurs when arteries grow thick and stiff and restrict blood flow to organs and tissues in the body. It is usually an age-related disease that occur in everyone but rarely causes any symptoms and can be accompanied by a number of diseases such as kidney disease, high blood pressure, coronary heart disease and coronary thrombosis [1]. Some diseases which are categorised under arteriosclerosis are discussed below:

- **Atherosclerosis:** it is associated with the narrowing of the lumen (inner diameter) of an artery. Atherosclerosis is a degenerative disease where masses of cholesterol accumulate on the artery wall, which then solidifies to form plaque. Over time the plaque deposits mature and increases in size, making the artery wall less compliant. It causes the lumen of the artery wall to narrow making it's surface rough, where clots may form [4, 5, 6]. In some cases, the lumen of the artery can be completely occluded, preventing perfusion of certain organs such as the heart and the brain [5]. Atherosclerosis of the carotid artery, also known as carotid artery stenosis becomes symptomatic in people after 40 years of age. However, asymptomatic stenosis starts to occur from an earlier age [7]
- **Aneurysm:** it occurs when a part of the artery wall becomes weak and bulges out, forming a sac or a bubble which is called an aneurysm [4, 6]. Some possible

causes for an aneurysm to form are atherosclerosis, congenital conditions, infections or traumas [5]. Aneurysms most frequently occur in arteries leading to the brain, cerebral arteries, points along the aorta and the abdominal region [4, 5, 6]. Ruptures of any of these aneurysms can be life-threatening. Aneurysms can be asymptomatic, however, sometimes are detected during diagnosis of other purposes or through angiogram [4].

These medical conditions can lead to strokes, also known as cerebrovascular accidents (CVA), often caused when arteries in the brain are damaged, resulting in lack of oxygen to that part of the brain [4, 6]. Lack of oxygen can cause a section of the brain to die, leading to paralysis or death [6]. 80% of strokes are caused due to blockages in the arterioles in the brain; these blockages can be caused by atherosclerosis, completely blocking the artery or by blood clots which originate from other sections of a larger artery suffering from atherosclerosis such as the carotid artery [4, 6]. Fifteen million people around the world annually are affected by strokes, 67% to 83% of which are ischemic, 75% of such cases being caused by carotid occlusion, which is very often asymptomatic [3]. Strokes can also be caused by haemorrhaging; this usually happens when an aneurysm in the cerebral artery ruptures, releasing blood into brain tissue, causing damage to neurons due to excessive pressure and lack of oxygen [4].

2.2 Diagnostic Methods for Circulatory Conditions

Most of the above mentioned medical conditions, if identified in the early stages, can be treated, or the progression of the condition can be controlled. For this purpose, diagnostic methods have been developed, such as Ultrasound (US), computed tomography (CT), and magnetic resonance imaging (MRI) which will be described in this section.

- **Ultrasonography(US):** also know as doppler ultrasonography, sonography, ultrasound and doppler ultrasound. It has become the most commonly used method (gold standard) worldwide for assessing carotid artery disease [32]. It is quick, non-invasive, highly accurate and fairly in-expensive [13]. US works by emitting a

narrow beam of high-frequency sound waves into the tissue through the skin using transducers and then senses the echos created by the sound waves bouncing off of different biological tissue interfaces using the same transducer. The intensity of the echo and the time taken for the echo to reach the sensor are then used by dedicated algorithms to create an image of the cross sectional area along the path of the sound beam [33]. For US, a probe(also called wand) is usually placed on the skin over the area of interest to generate an image of the tissue at that site. These wands usually have multiple transducers positioned such that sweeping scans can be taken, the wands come in different shapes and sizes as US is used for diagnoses of other medical conditions as well [33].

Even-though US is very quick, as it displays the results almost immediately, is non-invasive and has greater than 90% accuracy [3]; It still suffers from some challenges; it depends on the operator for positioning of the US wand, which determines the orientations and quality of the image generated. The operator is also responsible for interpreting the generated image and distinguishes whether the results are accurate or have artefacts. Therefore the results obtained can vary depending on the diagnostician [33]. Thus, requiring the operator to be adequately trained to administer US, limiting the number of people that can operate and implement US. Therefore, US is only available in hospitals with dedicated departments, and is not part of regular checkups [3, 7]. Majority of the time, US is applied to patients who already have symptoms of atherosclerosis or have suffered strokes. Since the majority of strokes are caused by asymptomatic atherosclerosis, it would be beneficial to include US scans as part of regular checkups for patients over the age of 40 for early detection and progression monitoring of atherosclerosis. However, implementing regular checkups is both financially and practically not feasible as the cost of running such tests on regular bases would be too high, and the number of skilled operators is limited, this would increase the time taken to test every one [3, 7]. Therefore, there is a need for a method that is fast, inexpensive, and not heavily operator dependent that can be implemented by anyone as a preliminary

test to identify patients that need to be further tested with US or other detection modalities. Figure 2.2 'a' shows the process of a US scan of a carotid artery being performed. Here it can be seen that the wand is being held on the neck of the patient by the operator to locate the artery, the image generated from the US is shown in 'b', and the waveform generated as a result of flowing blood in the artery is shown in 'c'.

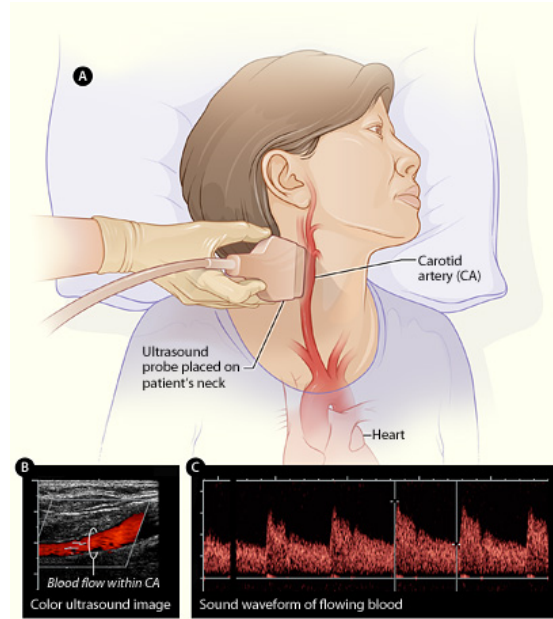


Figure 2.2: Carotid Ultrasonography implementation and results. a) shows the positioning of the wand by the operator over the sight of interest. b) shows the colour image generated from the results of US. c) shows the sound waveform representing the flow of blood in the artery. [34]

- **Computed tomography angiography (CTA):** Another method for detecting atherosclerosis is CTA; it uses x-ray images of the head and neck from different axis to create an image of the vascular structure. It is implemented by laying the patient horizontally and inserting them into the device. The device consists of an X-ray emitter and the detectors positioned diametrically opposite each other. Taking measurements as both the emitter and detectors are symmetrically rotated. Images are generated using algorithms based on the attenuation of the emitted signal [35]. It also uses iodine is used as a contrast material injected intravenously; this is done to make the vascular structure more distinguishable from the surrounding

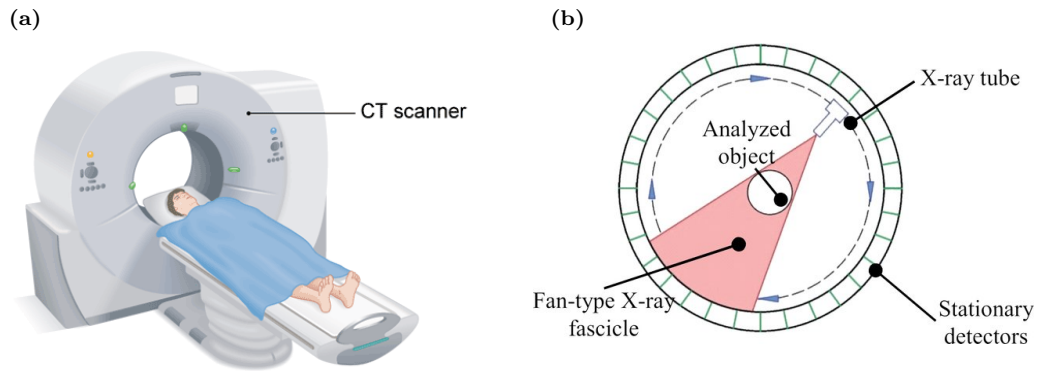


Figure 2.3: CT scanner. a) shows the CT scanner [36]. b) shows the working principle of the CT scanner [37] where the transmitter and the detectors are rotated synchronously

tissue[15].

CTA has great spatial resolution, superior contrast resolution and speed. It is relatively operator-independent and also allows the measurement of the size of the stenosis making it the most desirable method for diagnosis [12, 15, 16]. However, this method is expensive, only takes static measurements. Most often, it is used when the patient has already suffered a stroke and or is showing symptoms of atherosclerosis. The use of iodine contrast medium intravenously and radiation also limits the frequency of implementation of this method [12, 15, 16].

- **Magnetic resonance imaging (MRI):** As the name suggests MRI depends on the magnetic properties of the nuclei of certain atoms. More specifically, the hydrogen nucleus which is present in water molecules and therefore present in all biological tissue is used [17]. MRI uses radio waves, to rotate the hydrogen nuclei, which then oscillate in the magnetic field while returning to equilibrium causing the emission of a radio signal. These signals are detected using antennas (coils) and used to generate detailed images [17]. Figure 2.4 shows the cutaway of the MRI scanner along with the position of the patient, showing the internal magnet, the radio frequency coil, and the gradient coils.

Magnetic resonance angiography (MRA) is the term used when angiographic measurements are taken through MRI.. It is divided into two main categories: time

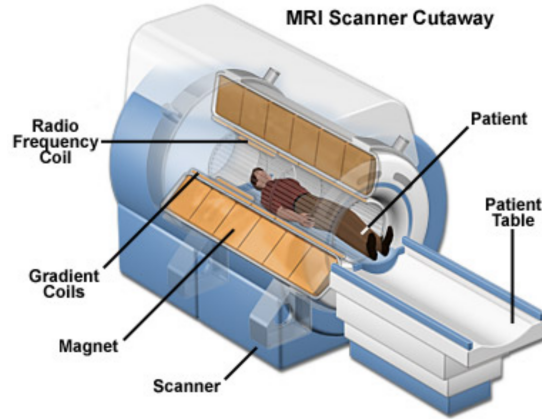


Figure 2.4: MRI scanner. The cutaway of the MRI scanner is shown and the magnets, gradient coils and the position of the patient can be seen [38]

of flight MRA (TOF-MRA) and contrast-enhanced MRA (CEMRA). TOF-MRA is the quicker of the two methods, where a single measurement is taken for each slice to generate an image. TOF-MRA only provides qualitative assessment of flow velocity and has incomplete background suppression, therefore suitable only for visualising moderate-sized arteries [17]. CEMRA on the other-hand takes at least two measurements: one as a reference measurement to subtract from the second measurement. It generates a flow enhanced image where the surrounding tissue information is suppressed, and the vascular structures are more clearly visible. CEMRA takes longer to perform than TOF-MRA as multiple scans need to be made; it also requires the velocity of blood in order to acquire accurate measurements[17].

Overall, MRA can generate a reproducible three-dimensional image with good sensitivity for detecting carotid stenosis; it is less operator dependent and has no radiation. However, MRA is expensive, is less readily available, cannot be performed on all patient for various reasons [12].

- **Photo plethysmography (PPG):** This method relies on the reflection, scattering and absorption of light. As the absorption and reflection of light in vascular tissue vary with arterial pulsation, this causes variations in the intensity of light. Light intensity variations can be detected using photo-detectors. Transmission and

reflection are the two main models used in PPG. In the transmission model, the emitter and detector are positioned on opposite sides of tissue. Its use is limited to peripheral areas, such as the finger, earlobe or toe where the distance between the emitter and detector is small. In the reflection model, the light source and detector are placed adjacent to one another, taking measurements from reflected light. The reflection model, virtually allowing it to be used on any vascular tissue; however, the location of the vascular tissue needs to be known along with its depth from the sensor. In both models, the photodetector measures the intensity of reflected and backscattered light, relating it to the change in blood volume. The detected signal has an AC and DC components, the AC component corresponds to the cardiac cycle, and the DC component corresponds to the nature of the material through which the light travels. By using different wavelengths, different analytes in blood can be deduced; for example, oxygen saturation can be obtained by using red and near-infrared light [39]. The positioning of the light source (LED) and the photo-detector for the transmission and reflectance model are shown in figure 2.5. PPG is mainly used for monitoring: changes in blood volume, pulse oximetry (oxygen levels in blood), vascular diagnostics, and to find the beat to beat blood pressure. It is quick, inexpensive, non-invasive and safe to use over long periods. However, it suffers from motion artefacts calibration assumptions, probe placement, and is affected by skin pigmentation [39].

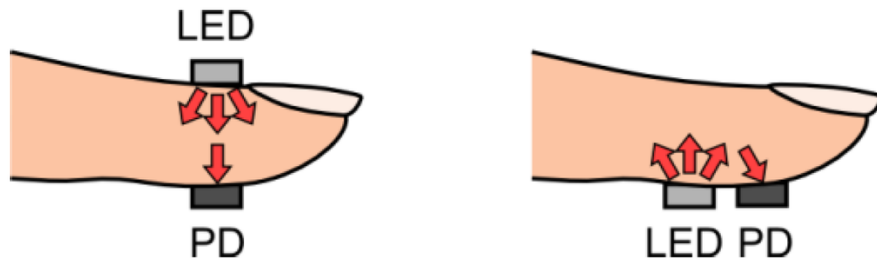


Figure 2.5: Placement of Light-emitting diode (LED) and photo-detector (PD) for transmission-mode and reflectance-mode used in PPG [40]

- **Impedance plethysmography (IPG):** IPG is an uncomplicated, non invasive and potentially portable and inexpensive method for measuring cardiac functions

such as SV, CO etc [41]. It is also known as impedance cardiography (ICG) or admittance cardiography (ACG) when applied to the thorax [19, 27, 42]. IPG relies on the electrical properties of tissue to monitor changes in blood volume in the human limbs or thorax. This is possible as blood is the most conductive tissue therefore as the volume of blood varies so does the total conductivity of the tissue being monitored[43].

IPG measurements are usually taken by attaching four electrodes (highly conductive contacts) on the surface of skin. Using two electrodes a small AC current is applied (usually $1 - 5\text{ mA}$ in amplitude) and the resulting potential is measured using the remaining electrodes. Using the applied current and the measured voltage the impedance of the tissue is calculated [19, 27, 29, 30, 42, 43, 44]. The impedance measurement process will be further described later on in this chapter. IPG measurements are usually taken from the thorax or the limbs [19, 27, 29, 30, 42, 43, 44]. There are two main types of electrodes used for taking IPG measurements, band electrodes which comprise of long strips of metallic tape which are wrapped around the circumference of the body [19, 29, 30]. Spot electrodes are the second type, majority of the time these electrodes are the same electrodes used for electrocardiograms. Both types of electrodes have their own advantages and limitations, the band electrodes have a larger contact area as they wrap around the body which also gives it a smaller contact impedance (described later on) and they can handle high currents[19, 29, 30]. However, the process of wrapping the electrodes around the body makes them difficult to apply, the measurements are susceptible to motion artifacts, usage over extended periods of time causes discomfort to the patients and the measurements taken using them is the average of the total volume change therefore they lack specificity and the magnitude of change obtained due to volume is overshadowed by the magnitude of the surrounding tissue[19, 29, 30]. Spot electrodes on the other hand are easier to apply and can be used for extended periods of time without causing too much discomfort to the patients. It is not susceptible to motion artifacts and produces a larger magnitude of change in response

to changes in volume[19, 29, 30]. However, spot electrodes are harder to position as the area they need to be applied need to be known, as there is less surface area to the electrodes the contact impedance is much higher than their counterparts, they can handle a lower injected current and the baseline of the measurements a higher than those obtained when using band electrodes [19, 29, 30].

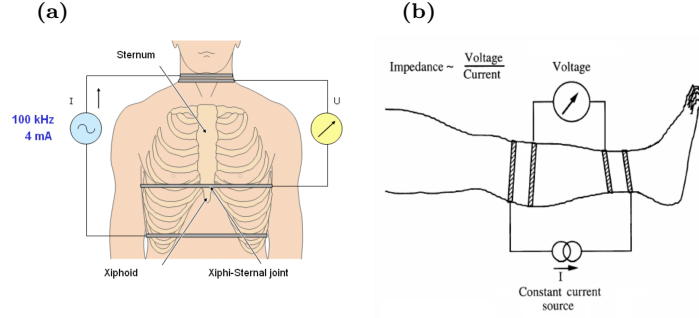


Figure 2.6: Impedance plethysmography electrode placement. a) shows band electrode placement on the thorax [44], b) shows band electrode placements over a limb [45]

Most of the above mentioned methods (Excluding PPG and IPG) are expensive, heavily operator dependent, not very accurate, can be harmful to patients, extremely bulky and cumbersome, thus they exist only in well-equipped medical centres and only confirmed symptomatic cases are referred for such examinations (table 2.1). However, this is potentially costing the lives to millions of people that can't get access to these expensive settings or that could be saved if early detection was possible. Therefore, it is desirable to have a cheap, safe, operator-independent, compact system that would give an indication to identify patients that require to be further assessed and could be used as part of routine checks for early detection. Bio-impedance is a potential tool that fits these criteria and is discussed below.

Table 2.1: Diagnostic method comparison

| Method | Cost | Size | Operator Dependence | Availability | Type of Measurement | Imaging Sensitivity | Portability | Safe to Implement |
|--------|--------|--------|------------------------|--------------|--------------------------|------------------------|-------------|----------------------|
| US | Medium | Medium | High | Medium | Imaging, Flow monitoring | High | Low | High |
| CT | High | Large | High | Medium | Imaging | High | Low | Medium |
| MRI | High | Large | High | Medium | Imaging | High | Low | High |
| PPG | Low | Small | Low | High | Flow monitoring | N/A | High | High |
| IPG | Low | Small | Low | High | Flow monitoring | N/A | High | High |

2.3 Bio-impedance Principles, Diagnosis Systems & Methods

2.3.1 Fundamental Bio-impedance Principles

Impedance Measurement Principles

Applying an AC voltage to a material induces current to flow through the material, by taking the ratio of the applied voltage and the induced current, the impedance of the material can be obtained. To apply the signal, electrodes must be placed on the surface of the material under test. In most applications, two to four electrodes are used to take measurements (the number of electrodes and their topologies will be discussed later in this chapter). In most cases that use four electrodes, two electrodes are used to apply a small AC signal (current or voltage) referred to as current carrying (CC) electrodes; the remaining two electrodes are used to measure the resulting signal referred to as pick up (PU) electrodes. Using Ohm's law and the applied and measured signals, the impedance of the material is obtained. This principle applies to almost all materials; hence impedance measurements are not only used in laboratories but also in lots of industrial and geological processes [18, 46, 47, 48].

Impedance measurements are used in many industrial applications, as the electrical impedance of different material correlate with different properties of the material, such as, water content in food production, structural properties of geological samples, finding abnormalities in a substance with known impedance in laboratories, and other industrial applications such as: quality control of paint, emulsion, electroplating, thin-film manufacturing, material fabrication, corrosion, mechanical performance of engines, and others [46, 49].

Tissue Impedance

Biological tissue exhibits both capacitive and resistive properties. Therefore tissue impedance contains both conducting and dielectric terms. The conductivity term (σ) accounts for the movement of free charges, and the relative permittivity term (ϵ_r) ac-

counts for the movement of bound charges in the dielectric due to an applied electrical field. Tissue comprise of multiple cells which are covered by a membrane. The membrane of cells behaves as a capacitor blocking dc and low-frequency current, however, allows high-frequency current to pass through it. The internal structure of the cell, on the other hand, allow all currents to pass through them; which applies to the fluids outside the cells as well. The electrical model of the cell membrane and the internal and external fluids is shown in figure 2.8. This behaviour causes the low-frequency current to flow around the cell and high-frequency current to pass through the cell, causing the impedance to change at frequency [18, 47, 50, 51, 52]. The paths ionic currents follow for different frequencies are shown in figure 2.7.

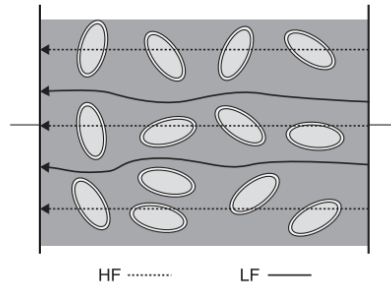


Figure 2.7: Current paths through tissue at low and high frequencies [18]

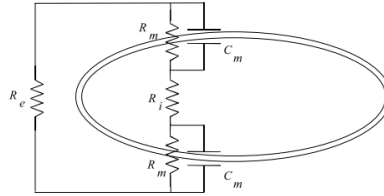


Figure 2.8: Electrical model of cell membrane, where the membrane capacitance is represented by C_m , extra-cellular fluid resistance is R_e , intra-cellular fluid resistance is R_i and the membrane resistance is R_m [52]

Both relative permittivity ϵ_r and conductivity σ of biological tissue are frequency dependent. This frequency dependence is known as dispersion. The dispersions are often separated into three regions: α (alpha), β (beta) and γ (gamma). Thus electrical impedance Z of biological tissues should be frequency-dependent over a wide range of

frequencies. The α dispersion is usually related to collection of cells, β dispersion is related to the capacitive charging of the cell membranes and the γ dispersion relates to the dielectric relaxation of free water. An idealised plot showing the α , β and γ dispersions of the relative permittivity as a function of frequency is shown in figure 2.9.

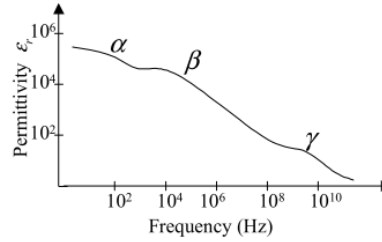


Figure 2.9: Frequency dispersion. Idealised plot showing the α , β and γ dispersions of the relative permittivity as a function of frequency of a biological tissue [52]

Different biological tissue gives different impedance readings. Blood, which is a liquid with blood cells flowing through it has a resistive impedance. This is because AC signals can freely move through the fluid around the cells. Skin comprises of different layers with the top layer mainly consisting dead cells, hence it is more capacitive impedance; this is because there is not much space between the cells to allow low-frequency current to pass freely [18, 47, 53, 54]. The impedance for organs such as heart and lungs changes with time due to their function. The heart pumps blood which has the highest conductivity. When the heart fills with blood its impedance decreases due to the increased amount of blood. When blood is pumped out, the impedance of heart increases. The lung tissue behaves oppositely since air is an insulator, during inspiration, the impedance of lungs increases, and during expiration, the impedance decreases [18, 23, 47]. There are also tissues which only allow current to flow in a certain direction such as the muscles, i.e. conductivity in different directions is not the same. Since the impedance varies for different types of tissue, this can be used to identify them and find any abnormalities such as cancers [18, 47, 55, 56, 57].

2.3.2 Methods

Electrical Impedance Spectroscopy (EIS)

Electrical impedance spectroscopy, also known as impedance spectroscopy (IS) or bio-impedance spectroscopy (BIS) is a method used to characterise the electrical properties of materials and their interfaces with electrodes. It is used to investigate how charge transfer occurs in material such as dielectrics (ions, semiconducting or insulators). The most common and standard approach to taking EIS measurements involves applying a single-frequency signal - voltage or current - to the interface and measuring the resulting current or potential respectively across the interface. Those measurements are then used to calculate the impedance which can be represented as magnitude and phase, or resistance and reactance at that frequency [58]; this process is then repeated for a range of frequencies. The results obtained from these measurements help characterise the frequency response of materials. There have been studies carried out where BIS is used to characterise the frequency response of different types of tissues [52]. When the typical frequency response of tissue is known, any variations in the measured impedance can be used to identify tissue abnormalities such as cancer cells [56]. Parameters such as: conductivity, dielectric constant, mobility of charges, equilibrium concentrations of the charged species, and bulk generation/recombination rates which relate to the material under test can be evaluated through IS. It also helps evaluate parameters related to the electrode/material interface, such as adsorption/reaction rate constants, capacitance of the interface region, and diffusion coefficient of neutral species in the electrode itself. IS has been used with chemical sensors and has been extensively used to study the membrane behaviour in living cells [58].

Electrical Impedance Tomography (EIT)

Image generation of impedance spectroscopy measurements is known as electrical impedance tomography. The process of measuring impedance in EIT is the same as for EIS, where a voltage or current is applied externally using surface electrodes and the resulting current or voltage is measured to get the impedance. EIT uses multiple electrodes,

at present, the number of electrodes that can be used varies from 8 – 128 electrodes depending on the measurement device. The electrodes are usually placed at equal distance around the circumference of the body, as seen in figure 2.10. There are different methods for impedance measurement, depending on the area of interest. The different methods include the neighbouring method, the cross method, the opposite method and the adaptive method [18, 47, 59, 60].

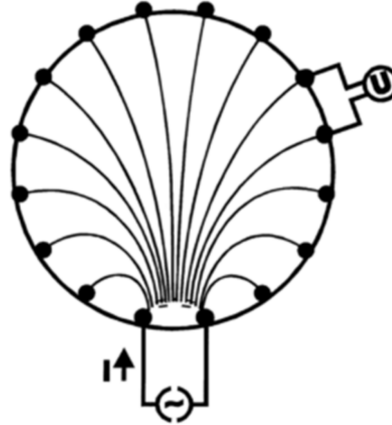


Figure 2.10: EIT electrode placement and imaging. Position of electrodes along the outer circumference of the body. [47]

The method used depends on the application and the hardware used. In the neighbouring method, for example, the stimulus is applied across one pair of neighbouring electrodes and measurements are taken across the remaining electrodes in pairs, as seen in figure 2.11a. Once measurements are taken from all the remaining electrodes, the injecting pair of electrodes is switched to the next pair of electrodes by one, the measurement process is then repeated, as seen in figure 2.11b. This process repeats itself until all possible pairs have been used for injection. It is either carried out once around the body or continuously in order to monitor change in impedance over time. For this method, one source of current injection and voltage measurement are multiplexed across all the electrodes. Similarly, some other methods require independent current sources for each electrode.

There have been many methods proposed over the years in order to generate images

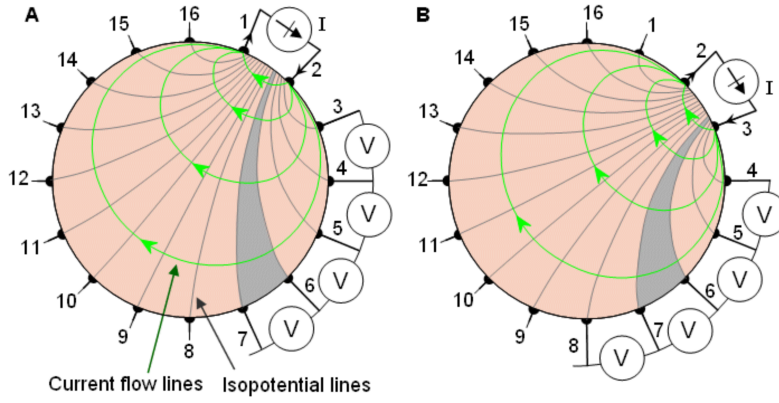


Figure 2.11: Current injection and voltage measurement in EIT [44]

from impedances reading. One such method involves using a computer with predicted impedance results, the measured impedance results are then used to find any differences as shown in figure 2.12a. The dark areas in figure 2.12a indicate low impedance readings and the light areas show high impedance readings, these are the predicted impedance readings. As can be seen in figure 2.12b, the areas where the measured readings match the expected readings are shown in dark colour, whereas the areas of mismatch are shown with a lighter colour. All the different images are then overlapped on top of each other, thus highlighting the area where the impedance is different from expected impedance, this process is shown in figure 2.12c [61].

The method described above is used for a phantom study with a tank filled with a liquid of known conductivity and a submerged sphere with a different conductivity. Similarly, imaging can be produced for impedance that changes with time such as the imaging of the lungs, heart and brain. This process can be used with a single frequency or multiple frequencies, such as for breast cancer detection. The number of electrodes used plays an important role in the imaging process, and so does the positioning of the electrodes. The reason for this is because theoretically, the more electrodes are used, the quality of the image generated should improve. This is because more values are obtained for the area, however in actuality it is not true. Since the surface area of any object is limited, the area to apply electrodes also decreases, reducing the distance between

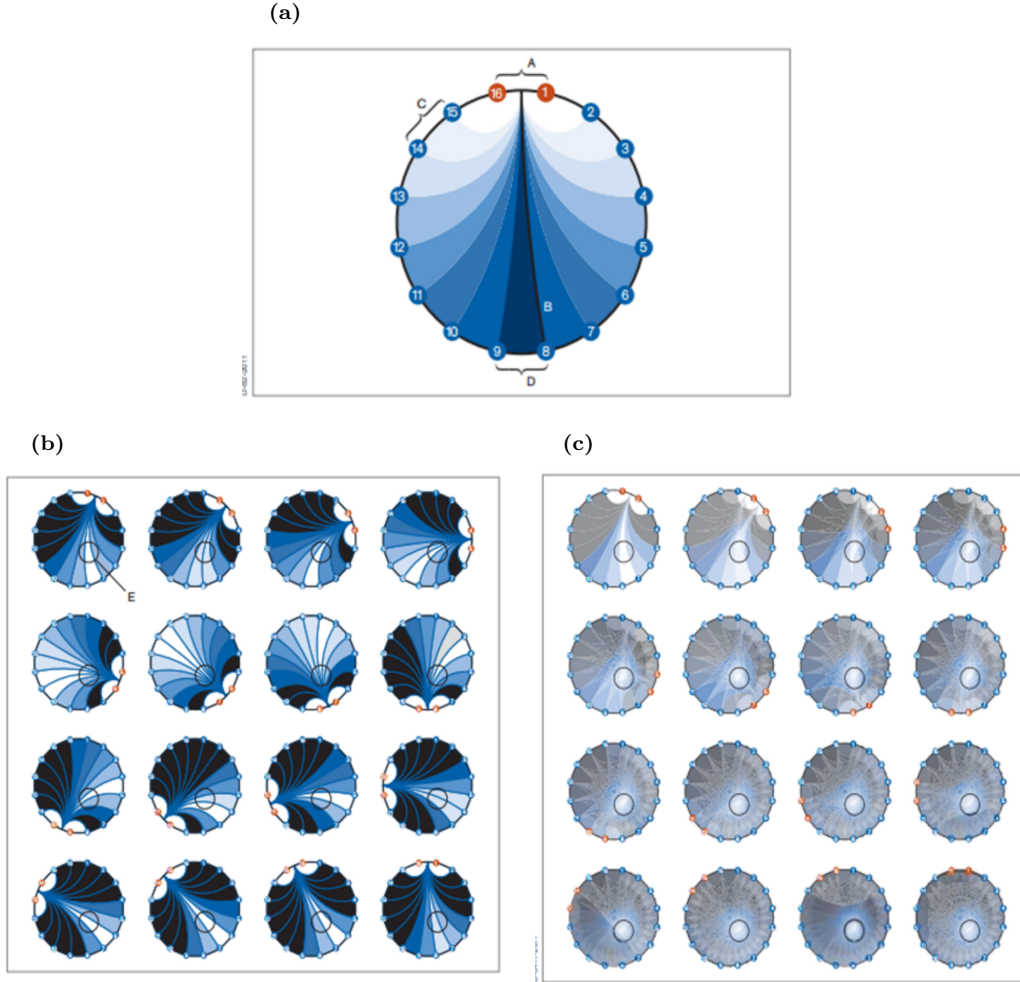


Figure 2.12: EIT measurement and simple imaging procedure. a) Voltage profile for a homogeneous structure, (A) is the point of current application, (B) is the isopotential lines, (C) represents the highest voltage measured as it is closest to the current application site and (D) represents the lowest voltage measured as it is furthest from the current application site. b) Voltage deviations in the presence of a regional increase of impedance, here deviations are represented with white and blue colours and black represents no deviations. c) Superposition of 16 voltage profiles to location the area of higher conductivity [61]

electrodes. The penetration of the electric field lines decreases as the distance between electrodes reduces this prevents the image from improving when more electrodes are applied.

Huang et al [62] attempted to improve the image quality by using movable electrodes in a phantom tank and managed to achieve a higher signal to noise ratio (SNR) and fewer artefacts in the image they generated. However, they found that this process takes longer to implement. Since this method required physically moving electrodes in order to take measurements, this makes it difficult to apply in taking in-vivo measurements. Another similar attempt was made by placing electrodes on an impeller for mixing process to improve imaging by Murphy and York [63]. Even though the image quality improved, this method cannot be used in medical applications. This shows that by having movable electrodes, it is possible to improve the image quality. However, currently it is not feasible to have movable electrodes for clinical applications.

2.3.3 Clinical Applications

Different characteristics of tissue can be identified using Electrical impedance spectroscopy. The total body water is one of the applications of EIS that is used clinically and is used to verify the water content of the subject [18, 64]. Another application of EIS is to monitor samples and to identify certain analytes (chemical compounds to be detected). Micro-electrodes are used to examine cells in tissue samples taken from patients [65, 66]. This is done to verify the effect of medication on the tissue sample and how long it takes for the medication to take effect.

Breast cancer detection is another application of EIS, this is because cancerous tissue of the breast has different impedance response than normal breast tissue [55, 56]. There is also research being carried out on identifying lithium in blood samples to make sure the patients do not have an overdose. Research is also being carried out in detecting ischemia for patients as it is hard to detect. Wound monitoring for patients who have diabetes without removing the bandages is important, so as to prevent further infection, contamination of the wound and to prevent disturbing the healing process. Research is

currently being carried out in order to monitor the healing process using EIS [25]. EIS is also being used to inspect thin film bio-material manufacture process, such as skin in order to monitor the growth progress [65]. These are some of the many medical applications of electrical impedance spectroscopy, each requiring different size and positioning of electrodes.

Electrical impedance tomography provides a safe, inexpensive and portable imaging system for monitoring time-varying changes and also for identifying abnormalities in the body. Currently, EIT is used for monitoring the lung for artificial respiration, this is done to ensure that the artificial respirator does not damage the patients lungs by pumping more air than the lung capacity [18, 47, 61]. EIT is also used to monitor brain activity in patients who have epilepsy to identify the affected part of the brain [47, 48, 67, 68, 69]. Breast cancer detection also uses EIT to show the location of the cancerous tissue uses multiple frequencies. Research is also being carried out for use of EIT to monitor the heart and the digestive system [18, 47, 59, 68].

2.3.4 Commercially Available Systems

As research has progressed in the field of impedance tomography, fully functional EIT devices have been made available commercially. The first commercially available device is the Sheffield MK1 in 1987 [47, 68, 70]. This device used 16 electrodes with an input frequency of 50kHz and was completely analogue. A portable version of the MK1 was then released in 1989 with the same specifications [47, 68, 70]. Soon after the Sheffield MK2 was released, this device used 16 electrodes as well but was a digital system which operated at 20 kHz [47, 68, 70]. In 1993, another device was introduced, the Sheffield MK3. That device, like its predecessors, used 16 electrodes but also had the ability to measure data at 8 frequencies between 9.6 kHz and 1.2 MHz [47, 68, 70]. It used analogue demodulation and as analogue technology was used, it was difficult to change the data acquisition protocols and it could only inject a single frequency signal at a time. An improvement to the MK3 was released in the year 2000 called the MK3.5, although this device used 8 electrodes and it allowed the use of 30 frequencies between

2 kHz to 1.6 MHz. This was a great improvement in the number of frequencies used, it could inject these frequencies simultaneously. The system itself was a digital system using programmable devices [47, 68, 70].

Other than the Sheffield group, there have been other companies and universities which have produced devices that are being used in the medical field; Drager is one such company. The Drager PulmoVista 500 is one of the devices produced by Drager. This device also uses 16 electrodes placed on a belt to make application easy and can use frequencies from 80 to 130 kHz. It is used in the ICU to monitor regional air distribution in the lungs for patients with mechanical ventilation to ensure patient safety [22, 61].

Another impedance device that is used for impedance mammography was developed at Dartmouth and has FDA approval for clinical use. This device was developed by Siemens Medical Systems, known as the TS2000 system. This system is used to scan for breast cancer. It uses one electrode attached to the wrist and 256 electrodes placed on an elastic net which are then pressed against the breast during examination. Current is injected between the wrist electrode and one of the electrodes on the net. Measurements are taken from the remaining electrodes. This process is repeated for all the electrodes in order to generate a 3-dimensional image. The net with electrodes is placed on a probe that can be moved to different positions by the physician [47, 55, 56]. This device has been used in many studies related to impedance mammography. There have been other systems developed by the Dartmouth group which are multiple source systems [47], but the above is a clinically available and more widely known system.

There are also systems developed by the Oxford Brookes group. These systems (OXPACT-II and OXBACT-III) are multi-source systems that use 64 electrodes, 32 of which are used as injecting electrodes and the remaining 32 electrodes are used for sensing the voltage. This system overcomes some problems that are inherent in the single-source systems such as the above systems. However, at the same time has its own drawbacks. This system increases the complexity of the measurement process and also changing the excitation frequency for single electrodes is complicated [47].

The adaptive current tomography (ACT) systems developed by the Rensselaer Polytechnic Institute group are multisource systems that mainly focus on the imaging of the

thorax. The ACT3 uses 32 injecting electrodes, and 32 voltage sensing electrodes with one ground electrode placed away from the rest of the electrodes. This system has high precision but is expensive to build and not easily portable[47]. These are some of the many different models and setups that can be found today with research being carried out to further improve on the many aspects of these systems (table 2.2).

Table 2.2: Commercially available systems

| Device Name | Manufacturer | Year | No. of Frequencies | Frequency Range | No. of Electrodes |
|-----------------------------|--|------|--------------------|-------------------------|-------------------|
| Sheffield MK1 | Sheffield Group | 1987 | 1 | 50 kHz | 16 |
| Sheffield MK2 | Sheffield Group | 1989 | 1 | 20 kHz | 16 |
| Sheffield MK3 | Sheffield Group | 1993 | 8 | 9.6 kHz-1.2 MHz | 16 |
| Sheffield MK3.5 | Sheffield Group | 2000 | 30 | 2 kHz-1.6 MHz | 8 |
| PulmoVista 500 | Drager | 2006 | multy | 80 kHz-130 kHz | 16 |
| TS2000 | Siemens Medical Systems | 2000 | adjustable | 100 Hz-100 kHz | 256 |
| OXPACK-II | Oxford Brookes Group | 1991 | 4 | 10, 40, 160 and 640 kHz | 64 |
| OXBACT-III | Oxford Brookes Group | 1994 | 4 | 10, 40, 160 and 640 kHz | 64 |
| Adaptive Current Tomography | Rensselaer Polytechnic Institute Group | 1994 | 1 | 30kHz | 32 |

2.4 Bio-potential Electrodes and Topologies

2.4.1 Bio-potential Electrodes

Electrode/Electrolyte Interface

The point where the metal electrode comes in contact with the electrolyte is where the conversion of electronic to ionic conduction occurs. In metals, the main charge carriers are the electrons. Electron current does not require transport of substance since the valence electrons can separate from one atom and move to the next atom allowing DC current to flow continuously. In electrolytes or ionic solution the main charge carriers are the ions, ionic current, unlike electron current, requires the transport of substance; hence DC current flow is limited and can cause damage [18, 58, 67]. At the point where

the metal electrode comes in contact with the electrolyte, two main reactions occur:

- **Non-Faradaic reaction:** When electrode comes in contact with the electrolyte, at that location the surface charge of the electrode attracts either negatively charged ions (anions) or positively charged ions (cations). The attracted ions in the electrolyte cover the entire surface of the contact area; in the electrode, the electrons also form a layer this phenomenon is known as a double-layer. The double layer acts as a molecular capacitor, where one plate of the capacitor comprises of the charge in the metal, and the other plate the ions in the electrolyte as shown in figure 2.13. if the net charge of one electrode is forced to be positive, it attracts anions and repels cations. The other electrode which is forced negative, will do the opposite, creating a neutral region in the space in between the two charged areas. When the charge of the electrodes is reversed, causing a redistribution of the ions without any change in the electrolyte till a state of equilibrium is reached once again [18, 58, 67].

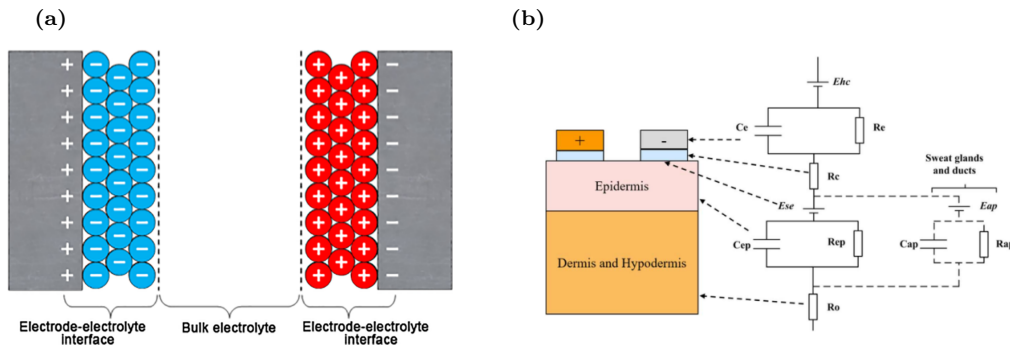


Figure 2.13: Electrode/electrolyte interface. a) distribution of ions between two metal electrodes immersed in liquid electrolyte solution (image taken from [71]), b) electrical representation of electrode/skin interface (image taken from [72])

- **Faradaic reactions:** When the net charge in the electrode is forced to exceed the equilibrium charge, charge is injected from the electrode to the electrolyte by Faradaic processes of oxidation and reduction. At the negative electrode, reduction takes place which requires the addition of an electron, while at the positive electrode oxidation takes place which involves removal of an electron. Unlike

non-Faradaic reactions, Faradaic reactions cause the creation of products; these products are reversible as long as the products are close to the electrode when the charge at the electrode is reversed. However, if the product moves further away from the electrode, the reaction becomes irreversible; this reduces the number of reactants in the solution to allow charge transfer. Applying DC signals to an electrode results in a permanent change in the electrolyte as well as corroding and damaging the electrodes through electrolysis [18, 58, 67].

Types of Electrode Materials Used

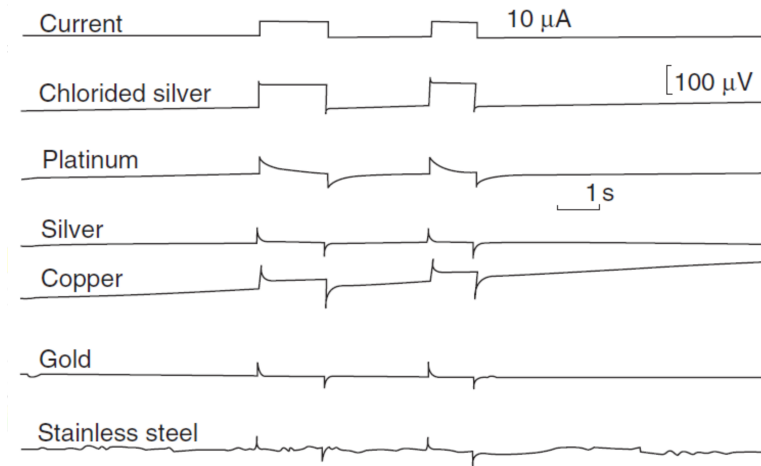
Almost all metals are conductive; some are good conductors and others not. Gold, silver, platinum, stainless steel and copper are some metals that conduct electricity, but not all of them can be used. There are certain aspects of the metal that need to be looked at before they can be used as electrodes. The application for which the electrode will be used also determines which metals can be used. For instance, electrodes which are implanted into biological tissue need to be non-toxic to the tissue. Silver is one of the metals that cannot be used as an implantable electrode as it is toxic to tissue, whereas gold or platinum can be used as implantable electrodes as they are non-toxic [18]

The electrical property of the metals is also important as some metals get polarised. This means that as a signal is applied to the electrode, an electrical charge develops across the electrode/electrolyte interface. This can cause errors in measurements and therefore must be taken into consideration when selecting electrodes; however most bio-compatible metals are polarizable. The list of metals, their properties and their uses can be seen in table 2.3 and the voltage measurement to a step-change in current using six different metals can be seen in figure 2.14.

The voltage measurement to a step-change in the current, as shown in figure 2.14 displays the polarisation of the electrodes. Only the chlorided silver electrode (Ag/AgCl) measures the actual voltage response. For most other materials shown, when the applied current goes from low to high, it causes a buildup of reduction products in the region near the electrode resulting in a positive current to flow and as depletion sets in the

Table 2.3: Electronic Conductor Materials [18]

| Metal | Properties | Uses |
|------------------------------|---|--|
| Ag/AgCl | Stable DC reference, low DC polarization, not bio-compatible | Skin surface electrocardiogram, electromyogram |
| Platinum metals | Non-corrosive, bio-compatible, polarizable | Needles, implants |
| Gold | Non-corrosive, less bio-compatible than Platinum | Needles |
| Titanium | Highly bio-compatible | Implants |
| Stainless steel | Mechanically strong, non-corrosive, highly DC polarizable and noisy, very alloy dependent | Needles |
| Tin, lead | Low noise, soft and mould-able | Electroencephalogram |
| Nickel | Thin flexible plates, skin allergic reactions | Skin surface |
| Silver, zinc, iron, aluminum | Pharmaceutical or bactericidal properties | DC therapy and skin Iontophoresis |
| Carbon | X-ray translucent, soft and flexible multiuse rubber plates and wires | Skin surface electrocardiogram, electromyogram |
| Polymers | Also found as ionic or mixed versions, special consideration must be taken for the ionic contact medium. May be a part of the contact electrolyte | Skin surface |
| Mercury | In research laboratories. Unique as a mercury dripping electrode with the metal surface continuously renewed | |

**Figure 2.14:** Measured voltage ΔV with six different electrode metals

magnitude of the positive current declines. However, when the current then goes from high to low, causing oxidation to occur, resulting in a negative current to flow and as depletion sets in the magnitude of the negative current declines [73]. Even though Ag/AgCl electrodes are not bio-compatible, they have a stable DC reference and low DC polarisation making them ideal for taking transcutaneous measurements.

Different Forms of Electrodes

Depending on the applications, the form of the electrode also changes. Over the years, many different electrodes have been developed, such as needle electrodes and disk electrodes. A lot of research has been carried out in order to optimise electrodes for certain uses. The needle electrodes are used to get impedance measurements between two points within the skin. Micro-electrodes are used to take measurements of cells. These electrodes are mostly used in laboratories for monitoring cells and tissue samples. Electrodes with suction or spring-loaded electrodes were also researched to improve contact with skin and to reduce errors in measurement due to electrode movement [18].

There is also research being carried out in order to use compound electrodes, where there are two electrodes in one, as seen in figure 2.15. The outer electrode, which is larger is used to inject current, and the inner electrode, which is smaller is used to measure voltage. Hua et al [74] found that using compound electrodes minimises effects of contact impedance in voltage measurements and helps generate a better image for EIT.

Disk-shaped electrodes are used for surface placement of electrodes. These types of electrodes are used for most non-invasive measurement applications and not only for EIT and EIT but also for EEG and ECG. In order to make the placement of electrodes easier on patients and to ensure that the electrodes are equidistant, the electrodes are placed on elastic belts, making it easier for the application on patients [18].

Implanted electrodes are also used where the electrodes are placed inside the human body in order to stimulate the tissue such as cardiac pacemakers, or for epilepsy treatment, auditory systems where the implant helps the patients hearing. There are also

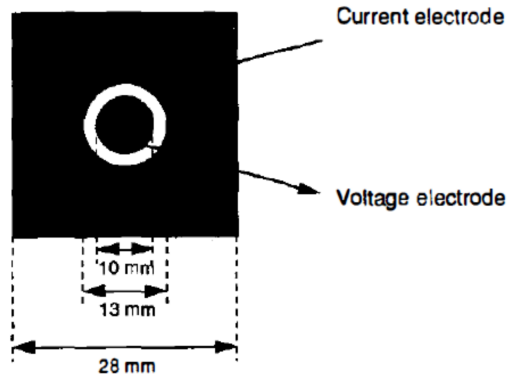


Figure 2.15: Compound electrodes with outer area used for current injection and the inner area used for voltage measurement [74]

systems built for monitoring the brain using implantable electrodes like for mapping brain functions and causes for epilepsy [18, 75].

Needle electrodes are also similar to the implantable electrodes as they are pierced into the skin. A small section of the needle is made of conductive material used as the electrode. Needle electrodes can have different orientations from having one to four electrodes in it. These are used to get the impedance of a specific point within the body. The needles are positioned on either side of the area of interest and then impedance measurements are taken through the section of the needle that acts as the electrodes [18, 47, 56, 57]. Recently there have also been advances in sportswear where multiple sensors have been incorporated in a bracelet to monitor the condition of the athlete including impedance sensors to monitor level of sweat, muscle impedance and heart rate [76].

Electrode Size and Positioning

The size and position of the electrodes also affects the measurements, as they affect the contact impedance and the depth of penetration of the current. The size of the electrode changes the contact impedance; the larger the electrode, the smaller the contact impedance as the area making contact with the electrolyte or skin is larger. Hence there is more area where the exchange of electrons can occur between the electrode and the

electrolyte. However the size of the electrodes does not affect depth of penetration of the electric field lines [18, 47, 48, 74] as can be seen in figure 2.16.

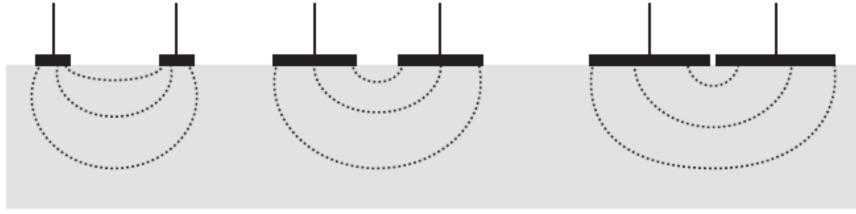


Figure 2.16: Electrodes with varying size and constant centre to centre spacing. It can be seen that even though the size of the electrodes is changed the depth of penetration of the electric field-lines does not change. [18]

In figure 2.16, the distance between the centres of the electrodes is kept constant, and the size of the electrodes is varied. As can be seen, the depth of penetration is not affected by the size of the electrodes. The depth of penetration of the electric field lines depends on the distance between the electrodes, as seen in figure 2.17. The closer the electrodes are placed together, the closer the electric field lines are to the surface, as the distance between the electrodes is increased the depth of penetration increases. This is because there is no fixed path for the current to flow through like in electronic circuits, as current flows in 3 dimensions in a volume conductor. As the distance, the current has to travel increases, the current starts to flow through more of the volume and hence the depth increases [18, 65].

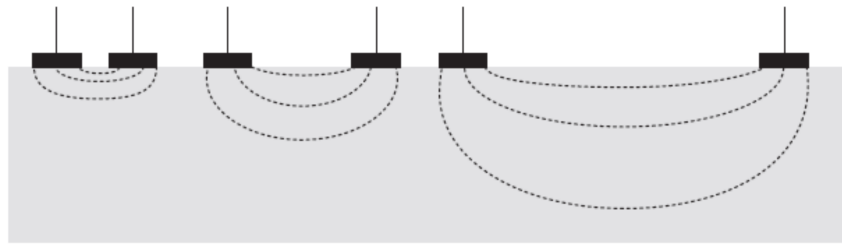


Figure 2.17: Electrodes with varying spacing and fixed electrode size. here it can be seen that as the spacing between the electrodes is increased the depth of penetration of the electric field-lines increases. [18]

2.4.2 Electrode Topologies

Topologies refer to the different methods of injecting current and measuring voltage that are used in EIT and EIS. There are three main methods, i.e., the bi-polar, tri-polar and tetra-polar topologies. These topologies are briefly described below.

- **Bi-polar Topology:** In the bi-polar topology, only two electrodes are used to inject current, and the same electrodes are used to take voltage measurements, hence it is known as bi-polar as shown in figure 2.18. This was the first topology used for measuring impedance. However, the measurements include not only the impedance of the test sample but also the contact impedance of the electrodes [18]. The contact impedance might not be of great importance in other industries, but when it comes to medicine, it is essential for the measurement to only be from the tissue of interest [18].

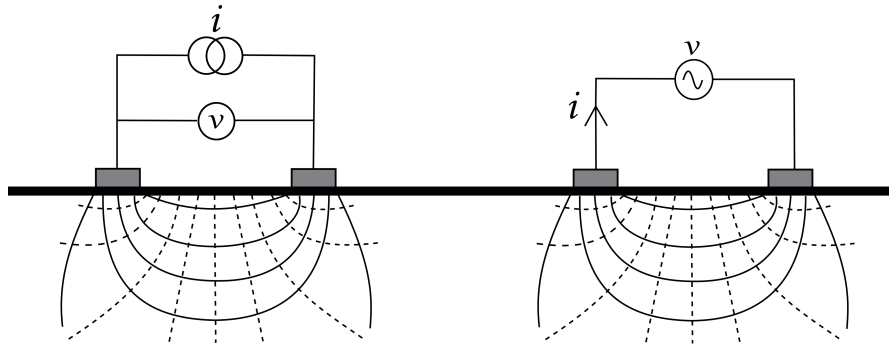


Figure 2.18: Bi-polar topology. On the left, current injection and voltage measurement method is shown. On the right, voltage injection and current measurement is shown.

- **Tri-polar Topology:** In this topology, three electrodes are used. For this method, the injecting pair and the measuring pair of electrodes share one electrode in common. As can be seen in figure 2.19, the electrodes labelled C and M are used to inject current, and electrodes labelled R and M are used for measurement of voltage, having the electrode labelled M as a common electrode. The advantage of using this method is that the contact impedance of only one electrode is part of the measurement. The measurement only includes the area between the measuring electrodes M and R and as the distance between these electrodes is increased, the

sensitivity gradually reduces. A positive sensitivity region is observed in the volume between the M and R electrodes, and a negative sensitivity region is present in the volume between R and C electrodes. This method is mostly used when the area under the M electrode is of importance [18].

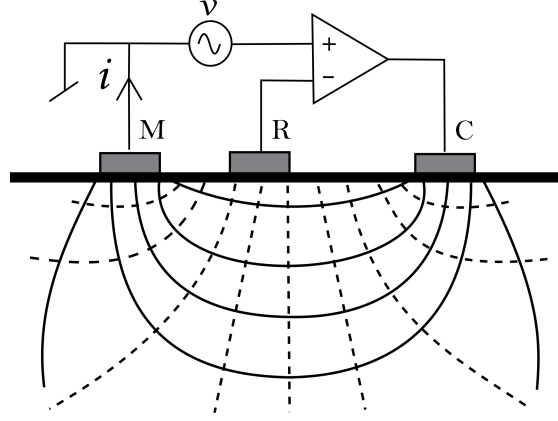


Figure 2.19: Tri-polar topology

- **Tetra-polar Topology:** This is the most frequently used method as the measurement does not incorporate the electrode impedance. This method uses four electrodes; two of these electrodes are used to inject current, and the other two electrodes are used to measure the voltage, as shown in figure 2.20. Electrode impedance usually occurs at the electrodes used for injecting current as potential is built up. However, at the electrodes where the measurements are taken, little to no current passes through them (as they are connected to the large input impedance of the instrumentation amplifiers). Hence, the electrode impedance is not part of the measurement. This allows for the measurement to be strictly of the volume being studied and hence the true impedance of the volume can be found [18, 52].

Sensitivity Distribution

Sensitivity S determines how much the different areas of a volume conductor contribute to the measured impedance. In a volume conductor, the current is not restricted to a single path and can flow in many different paths, hence in a volume the density of

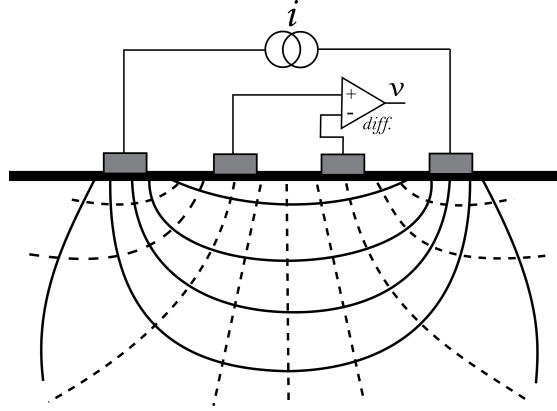


Figure 2.20: Tetra-polar topology

current flow is measured. Sensitivity for a system is calculated by the dot product of the current density fields of the CC and PU electrodes, as shown in equation 2.2. In the equation J'_{reci} and J'_{cc} are the current density fields of the PU and CC electrodes respectively when a current is applied to them separately [18, 77]

$$S = J'_{reci} \cdot J'_{cc} \quad (2.2)$$

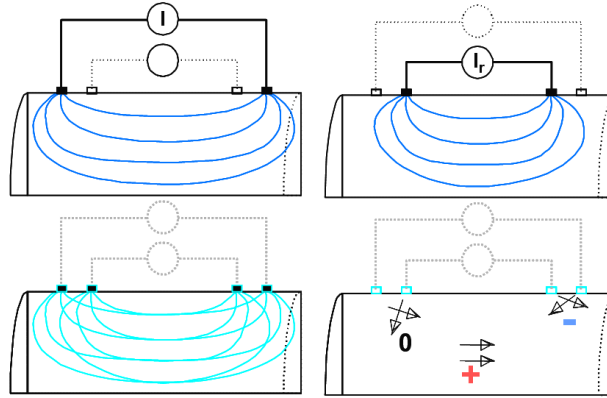


Figure 2.21: Simplified sensitivity distribution of a four electrode system for a uniform conductor. a) Current distribution field for CC electrodes. b) Current distribution fields for PU electrodes when current is applied to them. c) Overlapping of the two field lines. d) Resulting positive and negative regions [77]

A graphical representation of the density fields for the electrodes is shown in figure

2.21. In part a) of the figure, the current density fields for the CC electrodes are shown. Part b) of the figure shows the current density fields of the PU electrode when current is applied to them. Part c) overlaps the two field lines to show how the two intersect. The parallel components of the fields represent positive sensitivity, the perpendicular components cancel each other out resulting in zero sensitivity, and the components with an obtuse angle result in negative sensitivity as shown in part d) [77]. From part d) it can be seen that negative sensitivity forms closer to the electrodes where the density fields intersect at an obtuse angle. Any change that occurs in volume within the fields will be detected by a change in the impedance measurement. The degree of change will depend on where in the sensitivity region, the change occurs.

2.5 Multi-electrode Arrays

As the name suggests, MEAs are systems where multiple electrodes are used. They are placed in a different configuration and switched on or off depending on the application they are being used for. EIT is also a system that uses such arrays, where electrodes are placed around the area of interest. The electrodes are multiplexed in order to inject current and take measurements from different points, as mentioned earlier. MEAs are also used for 3D EIT systems where a 3d image is generated [51, 66]. They are also used in industrial processes such as mixing processes to ensure uniform mixing. Some examples of MEAs used in different medical fields are shown in fig 2.22.

MEAs are also used in a recently developed remote wound monitoring system. In this application, the MEA is made on a flexible material which is placed in contact with the wound inside the wound dressing. In the system, one electrode from the MEA is assigned as common, and the other measuring electrode is multiplexed with the remaining electrodes in order to change the depth of penetration. This system allows monitoring the wound without removing the wound dressing, preventing any disturbance to the healing process [25].

Implantable Micro-MEAs are also developed in order to monitor brain activity. Here the bio-electrical signals generated from the brain are picked up by the MEA to identify

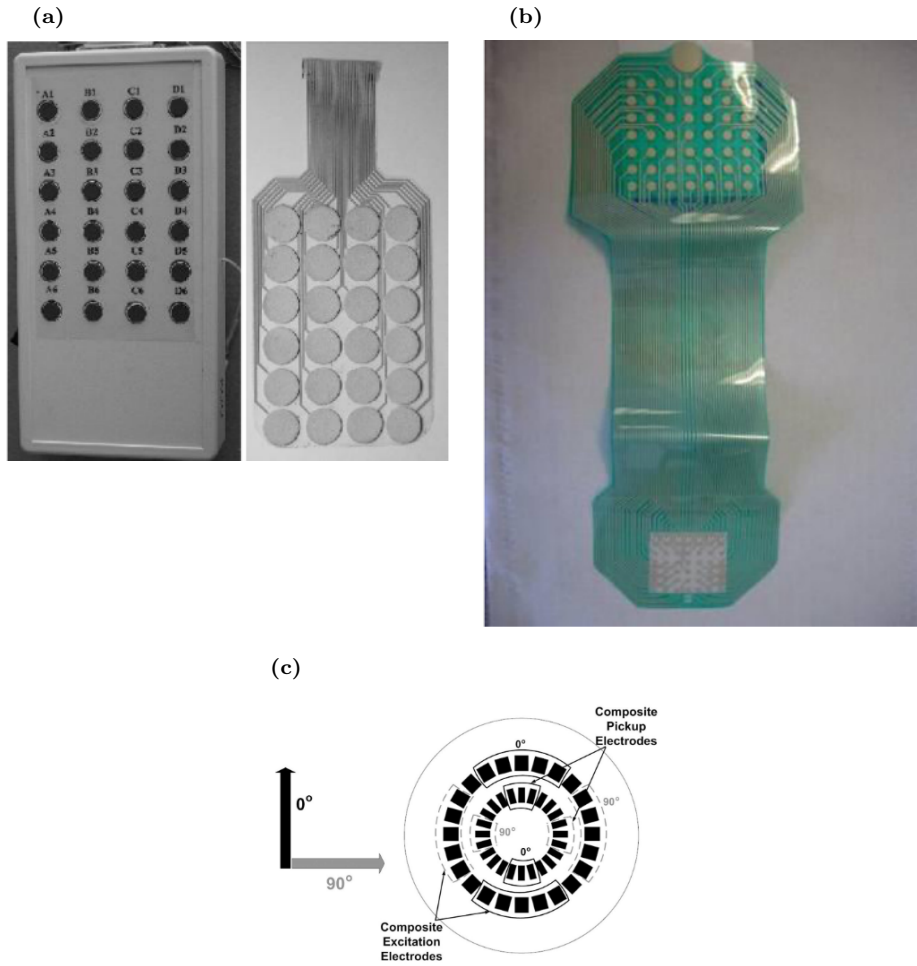


Figure 2.22: Multi-electrode arrays used for: a) electrical muscle stimulation [78], b) remote wound monitoring [25] and c) electrical impedance myography [79]

Table 2.4: Some MEA applications and uses

| Method | Measurement Electrode Selection | Technologies | Uses | References |
|--|---|----------------------|----------------------------------|------------|
| EIT | Single Electrode Multiplexing | Analogue/ Digital | Impedance Imaging | [47, 48] |
| Remote Wound Monitoring | Single Electrode Multiplexing | Digital | Skin Mapping | [25] |
| Transcutaneous Electrical Stimulation | Electrode Grouping | Analogue | Muscle Stimulation | [78] |
| Electrical Impedance Myography | Reconfigurable Electrode Grouping | Digital | Muscle Health Assessment | [79] |
| Neural Prostheses | Single Electrode Multiplexing | Analogue | Spinal Cord Stimulation | [80] |
| Brain Neural Response | Parallel Measurement | Analogue | Auditory Cortex Measurement | [81] |
| Brain Stimulation Recording | Parallel Measurement | | Acute Brain Slice Measurement | [66] |
| Neural Stimulation | Electrode Grouping | Analogue | Nerve Muscle Stimulation | [82] |

the active regions of the brain. These micro-MEAs are also used to stimulate certain regions of the brain as a treatment for patients who have epilepsy. These electrodes have also been used for studying test samples in laboratories [75, 83, 84].

In most or all of the above-mentioned methods, the MEAs are multiplexed having individual electrodes activated, moved or used as independent measurement points running in parallel. However, there haven't been many attempts at a different method for switching of these electrodes. Such as allowing the grouping of electrodes to form larger electrodes of different shapes and sizes and for allowing static or dynamic switching of electrodes.

2.6 (Experimental and Simulatory) Biological Models

2.6.1 Finite Element Modelling (FEM)

FEM is a method that uses mathematical equations and geometric models to predict the behaviour of different processes. It can be used in many disciplines, for example, the mechanical strain, flow rate or rate of reaction and can be useful in identifying any problems that might not have been considered. Such as, heat generated due to friction

or the amount of strain on a structure. These aspects can be calculated using a computer as long as the mathematical equations for the physics are known and there is a geometric model of the process [18, 85]. Special software is required in order to carry out these calculations. MATLAB is one such software that can be used as it is used to carry out mathematical calculations. There is also software which was originally linked with MATLAB and is now a very well know software known as COMSOL multi-physics.

COMSOL can be used in multiple disciplines in physics. It has multiple equations related to fields in physics, for example electrical, mechanical, and optical. It has basic equations for these fields already programmed into the software. This software also allows the user to combine different physics together and can be used in many fields. It can also be used to simulate the flow of current through an electrolyte using surface electrodes. In order to do that, a 3d model of the process is made, the parameters of elements used are then entered and the problem that needs to be addressed is identified. The computer program then processes this information and then provides a solution unless the problem is ill-posed [86, 87].

A tutorial article by Petterson and Hogetveit provides guidance on how to generate 3d geometry from MRI scans using Simpleware ScanFE+IP and then using COMSOL to run impedance-based simulations. In the tutorial, they provided the frequency-based parameters for different tissue which were obtained from other journals. They also demonstrated the setup of the boundary conditions and how to find the sensitivity for the four-electrode system using COMSOL. They also showed the contribution from different layers of tissue in their impedance readings. After they compared the simulated results with actual measurements, they found the results to be similar with minute differences [85].

2.6.2 Phantoms

The technological development process of devices that have electromagnetic interaction with the human body need quantitative and explicit validation of performance and safety. Simulations of numerical models can be used to simulate the system environment for

ideal cases; they cannot reflect the realistic environment which is vulnerable to various electrical, mechanical and environmental interferences. It would be preferred to use the human body as the measurement environment. However, it is essential that any test or measurement be carried out under controlled environment. Such an environment is important to validate the performance of the system under all possible operating scenarios to ensure the safety of those systems. For example, in order to evaluate the ability of a breast imaging system to detect tumours at multiple locations, it would be unthinkable to implement it on a patient, Therefore having a phantom mimicking the breast would help optimise the device before clinical trials on human patients can take place. The inherent uncertainties, such as respiratory movement, cardiovascular vibration and variable skin humidity in addition as well as the safety concern of the new devices, make it difficult to employing live human participants for testing devices. It is also difficult to reasonably estimate and investigate the level of risks from various scientific, physical and psychological aspects beforehand, making it difficult to receive an ethical clearance from proper authorities. Another approach would be to use a slab of meat obtained from the slaughterhouse and use that to take measurements. This approach has been used in many studies as its biological structure resembles that of human tissue. This approach, however, has some limitations; the sample needs to be fresh as the electrical properties of tissue change postmortem. It's inner layer structure is also unknown making it difficult to match to the simulation, it is difficult to replicate as the sample is difficult to preserve and it is costly to obtain the multiple samples. The use of artificial tissue emulating (ATE) phantoms are much more beneficial for the testing purpose of systems and devices, as they are more controllable, reproducible and relatively cheap [88].

Mobasbsber and Abbosh [88] have explored the different state-of-the-art ATE materials and phantom types for various operating frequencies and fabrication procedures. This includes liquid, gel, semi-solid (or jelly) and solid phantoms identifying the type of advantages and limitations of each. Liquid phantoms, as the name suggests, comprises of water with certain solutes mixed together to change the electrical properties. In these liquid phantoms, conductive and insulating materials can be suspended to create differ-

ences in the homogeneity, these phantoms are easy to prepare. However, It is difficult to maintain consistency of the material properties, as the materials tend to dehydrate, which drastically alters the relative permittivity and conductivity. Gel phantoms are more solid than liquid phantoms, and it can sustain homogeneity over a long period. However, it takes some time to form as gels most undesirable feature is its variable setting time. This may extend to 1 day, causing delays in the testing of the systems or devices. Semi-solid or jelly phantoms are capable of conforming to any shape independently. This property allows for multiple layers to be formed, making it possible to have multiple layer phantoms. However, unlike the liquid and gel phantoms, semi-solid phantoms are usually neither reusable nor dielectrically adjustable, the materials also tend to dehydrate and it is hard to preserve the materials over a long period of time. Solid phantoms are not water-based; they overcome the hydration drawbacks of the liquid, gel and semi-solid phantoms. Solid phantoms require special production equipment, as high temperature is needed for material blending, and high pressure is required for injection moulding purpose. This makes it more expensive than the rest of the phantoms.

For this study, it is essential to choose a method that is: not expensive, relatively easy to manufacture, allows multiple layers of different conductivity to be formed, and does not require additional support to hold its form. Therefore, it was decided to use jelly phantoms to test the system. The conductivity for the different layers used was taken from the properties used in the simulation at the frequency of interest. Using these conductivity values and equation 2.3 [89], the *NaCl* concentrations for the different layers were obtained and then used for manufacturing the phantoms used to test the systems. The NaCl concentrations for the different layers are shown in later chapters

$$\sigma = 215 \times \frac{\text{grams of NaCl}}{\text{solution volume (ml)}} + 0.0529 \text{ (S/m)} \quad (2.3)$$

In the above equation, σ represents the conductivity of the tissue, the 'grams of NaCl' represents the concentration of sodium chloride needed and the 'solution volume' is the total volume of the solution given in millilitres. The 215 and 0.0529 are constants given in [89].

2.7 Conclusion

In this chapter the physiology of the circulatory system is described, along with the composition of the vascular structures. Some of the diseases associated with arteriosclerosis are also discussed, highlighting the need for early detection. The basic working principles of some of the most commonly used diagnostic methods for circulatory conditions are also briefly discussed. The advantages and drawbacks of these modalities are also covered, which highlights the need for a safe, fast and easy to use early detection method. Bio-impedance diagnosis systems are proposed and elaborated, describing the basic principles involved in taking bio-impedance measurements and how the electrical properties of tissue influences bio-impedance measurements. Different types of bio-potential electrodes and their properties, along with their topologies are also described to show the importance of electrodes in bio-impedance systems. MEAs are also briefly described as a potential type of electrodes being used in some bio-impedance applications. Biological models such as FEM and ATE phantoms are also described.

The next chapter describes the simulation and experimental procedure followed in order to explore the possible application of using multiple electrode segments to emulate an electrode with a larger effective area. The ability of such a system to detect and take localised measurements will also be explored. Comparisons will also be made between localised and non-localised measurements using impedance plethysmography as an example.

Chapter 3

Dynamically Re-sizeable Electrodes (DRE)

In the previous chapter, a brief description of the physiology of the circulatory system was given along with the medical conditions associated with them and their diagnostic modalities were discussed. The theory behind bio-impedance measurements, their systems and applications were also discussed. The importance of the electrodes and their impact on the measurements were also elaborated. In this chapter¹, the concept of using multiple segmented electrodes to emulate larger electrodes will be looked at, with the aid of simulations and experiments and using impedance plethysmography as an example method.

3.1 Method

A novel approach to targeted impedance plethysmography measurements with dynamically re-sizeable electrodes (DRE) was explored. A system involving electrodes of adjustable effective size has been developed. Four elongated rectangular electrodes [42] (named hereafter stripe electrodes as in Fig. 3.1(b)) have been partitioned into smaller

¹This chapter has been published in IEEE TBioCAS [90] with two co-authors, who had significant input in the design and setup of custom impedance measurement circuitry as well as the operation of the impedance analysers. All the work presented in this chapter is work carried out by the author of this thesis.

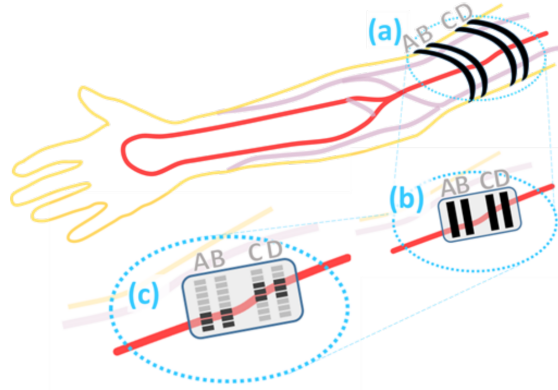


Figure 3.1: Simplified diagram showing the positioning of electrodes using: a) Band electrodes taking measurements from the whole section of the arm, b) Stripe electrodes taking measurements over the vessel and the surrounding tissue and c) Segmented electrodes grouped into localised effective electrodes to take measurements only over the targeted vessel.

electrode segments (Fig. 3.1(c)) which are interconnected through custom circuitry. The interconnection allows any of the segments in any of the four partitioned electrodes to be individually addressed to form single-segment variable tetrapoles (SSVT, Fig. 3.4c). It also allows the segments to be grouped so as to cover the targeted vasculature only, thus, forming effective localised electrodes to provide more targeted measurements. When all segments of each of the four partitioned electrodes are shorted, they each form an effective stripe or a pseudo-stripe electrode. The developed prototype DRE system was simulated using finite element modelling (FEM) analysis (COMSOL v.5.3a) and experimentally verified in-vitro by performing impedance measurements, through custom-made instrumentation, using gelatine phantoms to mimic tissue characteristics.

An approximate biological model of a subcutaneous blood vessel was constructed and simulated. It was idealised so as to assess the DRE method, and thus only a single frequency was considered, bone and muscle were not included. The model dimensions were limited, allowing the surface of the skin to be approximated as flat rather than curved. Moreover, the model considered only one vessel in the examined volume. The features considered, although geometrically idealised, were kept consistent with anatomy. The vessel was modelled in various orientations (θ) relative to the electrode tetrapole. Two research questions were assessed: 1) whether through SSVT the blood vessel location could be determined; and 2) whether the resulting localised electrodes are more sensitive

to variations in the blood vessel properties relative to the larger stripe electrodes.

3.2 Geometric Model Parameters

This section describes the geometric parameters used for constructing the model and phantoms used for simulations and experiments.

3.2.1 Initial Model

Initially, the model used was a parallelepiped geometric model with length $\ell_{m0} = 100 \text{ mm}$, width $w_{m0} = 50 \text{ mm}$ and height $h_{m0} = 10 \text{ mm}$ (fig 3.2). The model was divided into two main layers, a skin layer and a fat layer with heights of 2 mm and 8 mm respectively. A 5 mm diameter cylindrical blood vessel was embedded in the fat layer at a depth of 7 mm from the outer surface of the skin layer. The blood vessel was centred along L_{m0} at an angular orientation of -37° with respect to the longitudinal axis of symmetry of the electrode, as shown in figure 3.2. The different electrode lengths $\ell_e = (50 \text{ mm}, 45 \text{ mm}, 40 \text{ mm}, 35 \text{ mm}, 30 \text{ mm}, 25 \text{ mm}, 20 \text{ mm}, 15 \text{ mm}, 10 \text{ mm}, 8 \text{ mm}, 3 \text{ mm})$ had a fixed CC electrode width $w_{e1} = 2 \text{ mm}$ and a fixed PU electrode width $w_{e2} = 1.5 \text{ mm}$. The spacing between the CC electrodes was set to 15 mm , and the spacing between the PU electrodes was set to 10 mm . This model was used primarily in simulation to identify the influence of ℓ_e on the sensitivity of the measurements. Therefore the conductivity of the blood vessel was varied from the original conductivity of blood to twice the conductivity of blood with a step-change in conductivity of 10%. Measurements were taken using electrodes of different ℓ_e , with the smallest electrodes localised directly over the vascular structure. The results obtained from these simulations led to the selection of a model with smaller dimensions (described in the next section). This simplified the model further helping to speed up the scanning sequence and also helped design the lumped impedance model.

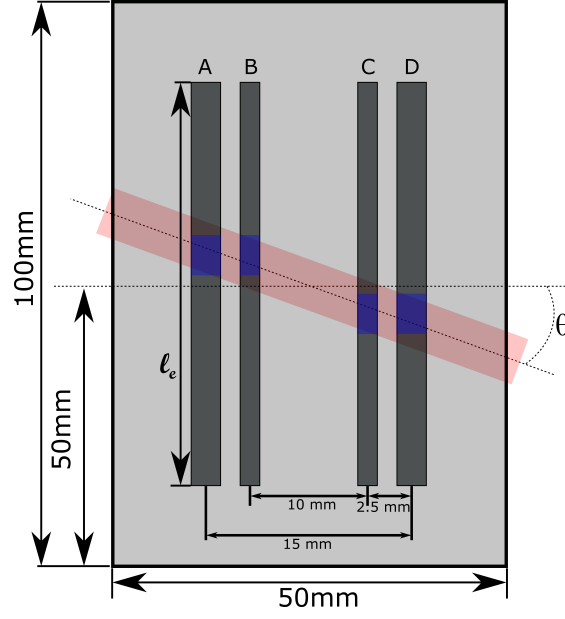


Figure 3.2: Initial model top view. Shows the model dimensions top view showing electrode length ℓ_e and vessel location.

3.2.2 Final Model

A parallelepiped geometric model with length ℓ_m , width w_m and height h_m of 45 mm, 20 mm and 10 mm respectively was designed to examine the aforementioned two research questions (Fig 3.3). The model was used as a template for both the gelatine phantom used in experiments and for the FEM simulations. It featured three main structures of homogeneously conductive geometries: a 2 mm thick skin layer, a 8 mm thick fat layer and a 5 mm diameter cylindrical blood vessel embedded in the latter. The blood vessel's longitudinal axis was on a plane parallel to- and 7 mm deep from the skin surface plane on which the electrodes were attached. Assuming that, realistically, perfectly in-line placement of the electrode tetrapole relative to the blood vessel would be very difficult to achieve, tests - mainly in simulations as described later - were designed to mimic imperfect placement by involving a number of orientations (θ) of the vessel relative to the tetrapole's middle axis of symmetry (i.e. the axis connecting the electrodes across their centres).

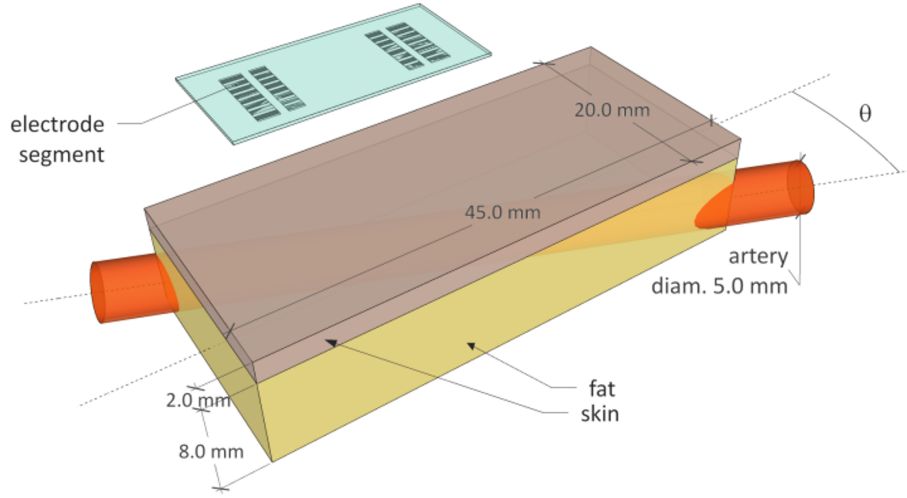


Figure 3.3: Overall dimensions for 3D simulation model

3.2.3 Tissue Parameters

The electrical properties of biological tissue are frequency-dependent and have conductive and reactive elements [91] and impedance plethysmography measurements have been mostly reported at frequencies between 10KHz 100KHz [92, 93]. In simulation, it was fairly easy to assign conductivity and relative permittivity of different types of tissue to sections of the 3D model used for simulations [85]. However, when modelling biological tissues experimentally using gelatine phantoms, it was not straightforward to replicate the reactive element [88, 89, 94], and thus the conductivity of tissue that corresponds to the impedance magnitude at a particular frequency of choice was used. For the simulation model used here the conductivity values for skin, fat and blood were set to 2.937 mS/m , 42.954 mS/m and 700.04 mS/m and the relative permittivity values were set to 29010, 911.54 and 5248.2 respectively corresponding to impedance measurements at a frequency of 10KHz as reported in [54, 95]. For the experimental phantom, the conductivity values were altered by varying the concentration of NaCl (sodium chloride) in the solution used to create the phantom [89]. That frequency value was at the lowest end of the aforementioned spectrum, and it was selected to represent a worst-case scenario in terms of skin and fat layers impeding the injected current.

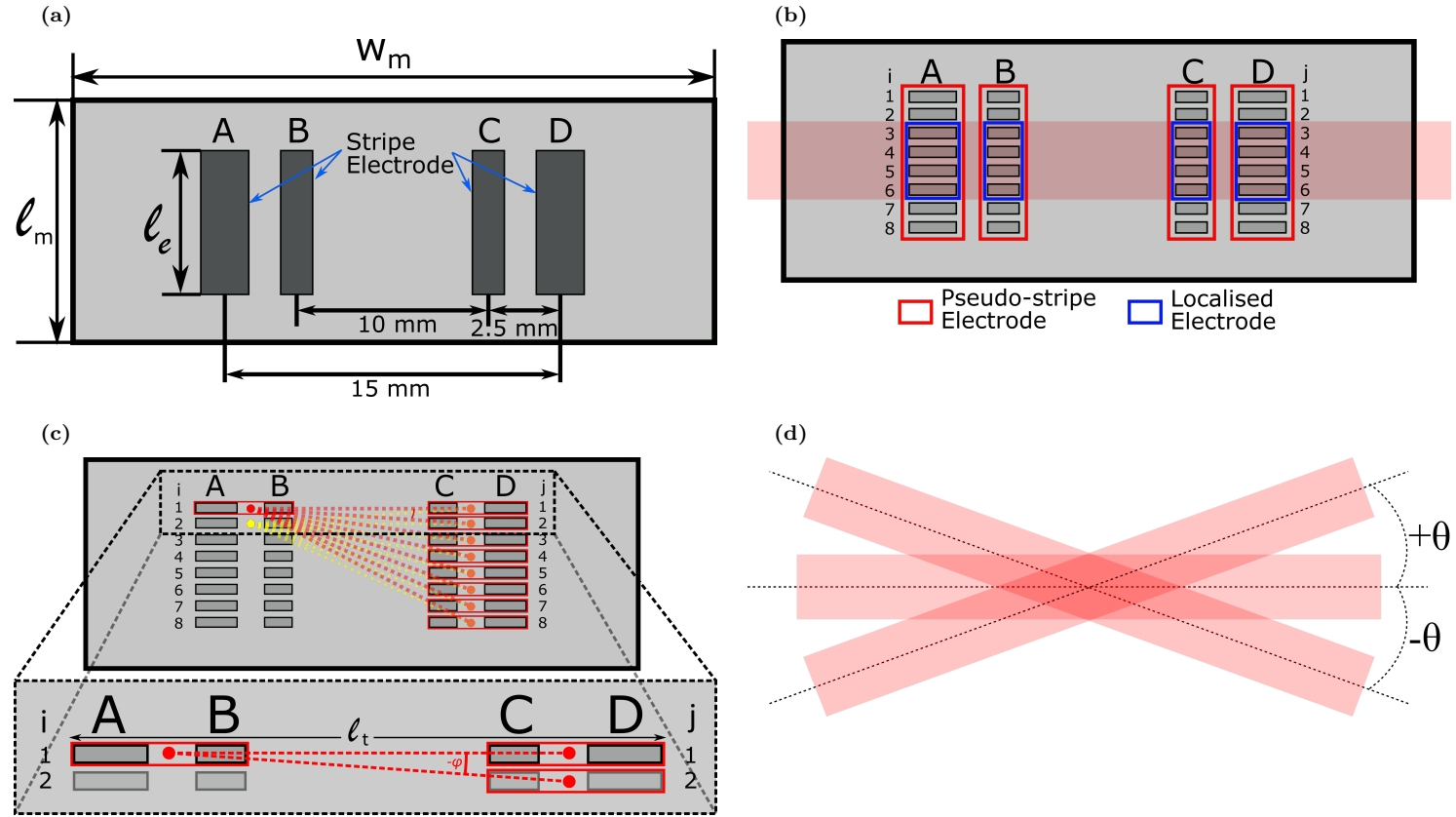


Figure 3.4: Model parameter overview. a) Stripe electrode setup, where W_m and ℓ_m are used to refer to the length and width of the model and ℓ_e is used to refer to the length of the electrode. b) Electrode groupings, here red is used to show segments used to create pseudo-stripe electrodes and blue is used to show the localized electrode over the blood vessel. c) Segmented electrode setup and tetrapole length, Here ℓ_t refers to the length of a single SSVT position and ϕ shows a single SSVT angle. d) Vessel angle θ is show demonstrating the vessel position with positive and negative θ values.

3.3 Electrode Design

Impedance values were to be extracted through electrodes attached to the skin layer surface in both the experiments and the simulations. For current injection electrodes, it was important to have a relatively large area to reduce the electrode-electrolyte interface impedance to avoid overloading the current injection circuitry. The voltage measurement electrodes could be made smaller – as their interface impedance could be ignored – increasing the measurement precision and the signal-to-noise ratio of measured data [74]. Therefore here four stripe electrode sites A, B, C and D were considered (fig 3.4a), with the current injection electrodes A and D having a $2\text{ mm} \times 8\text{ mm}$ geometry, and the voltage measuring electrodes B and C being $1.5\text{ mm} \times 8\text{ mm}$. The length of the electrodes (ℓ_e) was chosen so as to adhere to the dimension limitations of the model - so as to approximate the arm skin as being flat - and it closely resembled electrodes used in [96]. Each stripe was subdivided into eight 0.6 mm long segments separated by a 0.4 mm gap (fig 3.4c). The centre to centre distances were 15 mm for electrodes A and D and 10 mm for B and C, resulting to a 2.5 mm distance between each of electrodes A-B and C-D. The electrode spacing was designed to cover adequate length of the blood vessel to increase the volume of the blood contributing to the measurements.

3.4 Lumped-impedance Simplified Representation

To ascertain the theoretical basis of research question 2, prior to the experimental and the simulation assessments, an approximate analysis could be offered through a lumped impedance representation of the cases involving localised versus longer electrodes. It has generally been shown that the impedance of different tissue layers can be approximately represented by simplified lumped impedance models [72, 97, 98] with impedance magnitudes at the applied frequency considered. Following the geometric model presented previously, and assuming $\theta = 0$, Fig. 3.5 illustrates a simplified lumped impedance model for a cross-section of juxtaposed skin, fat and blood layers schematically, with respective impedances Z_S , Z_F and Z_B , respectively. A side view is shown in Fig. 3.5a, while Fig.

3.5b is the top view (from the skin down to the fat layer) of current paths along the tetrapole, assuming the blood vessel is on the axis connecting the electrodes across their centres.

The nature of electric/ionic current is to travel between two electrodes by taking the path of least resistance, and with the skin being the most insulating layer, currents will mostly traverse it flowing through it to the more conductive layers below [99]. Currents originating directly above the vessel will cross the skin and fat layers almost vertically and will enter the blood, flowing across it for a length (ℓ_t) approximately equal to the distance A-D. Currents flowing between electrodes A-D outside of the boundaries - but in the vicinity of the blood vessel will deviate from their straight geometric path and pass through it. As the length (ℓ_e) of the injecting electrodes extends away from the centrally located vessel currents adequately far from it will experience a minimum resistance path by traversing the skin and traversing fat tissue of equal length to the distance travelled inside the vessel by the centrally located field lines. The corresponding fat impedance, in that case, is shown as Z_{FF} . For a specific value of Z_B , the baseline impedance value $Z_{LOCbase}$ if localised electrodes are used, and the minimum corresponding baseline impedance value $Z_{STRbase}$ when longer stripe electrodes are used, are calculated below. The stripe electrodes used in this calculation are long enough so as to allow n current paths to pass through fat surrounding the blood vessel. Localised electrodes baseline impedance:

$$Z_{LOCbase} = 2Z_S + 2Z_F + Z_B \quad (3.1)$$

Larger stripe electrodes baseline impedance (n paths not passing through the vessel):

$$Z_{STRbase} = \frac{1}{\left(\frac{1}{Z_{LOCbase}} + \frac{n}{2Z_S + Z_{FF}}\right)} \quad (3.2)$$

because $Z_{STRbase}$ is the parallel combination of $Z_{LOCbase}$ and n parallel branches of $2Z_S + Z_{FF}$.

In order to examine which electrode type is more sensitive to blood variations, the

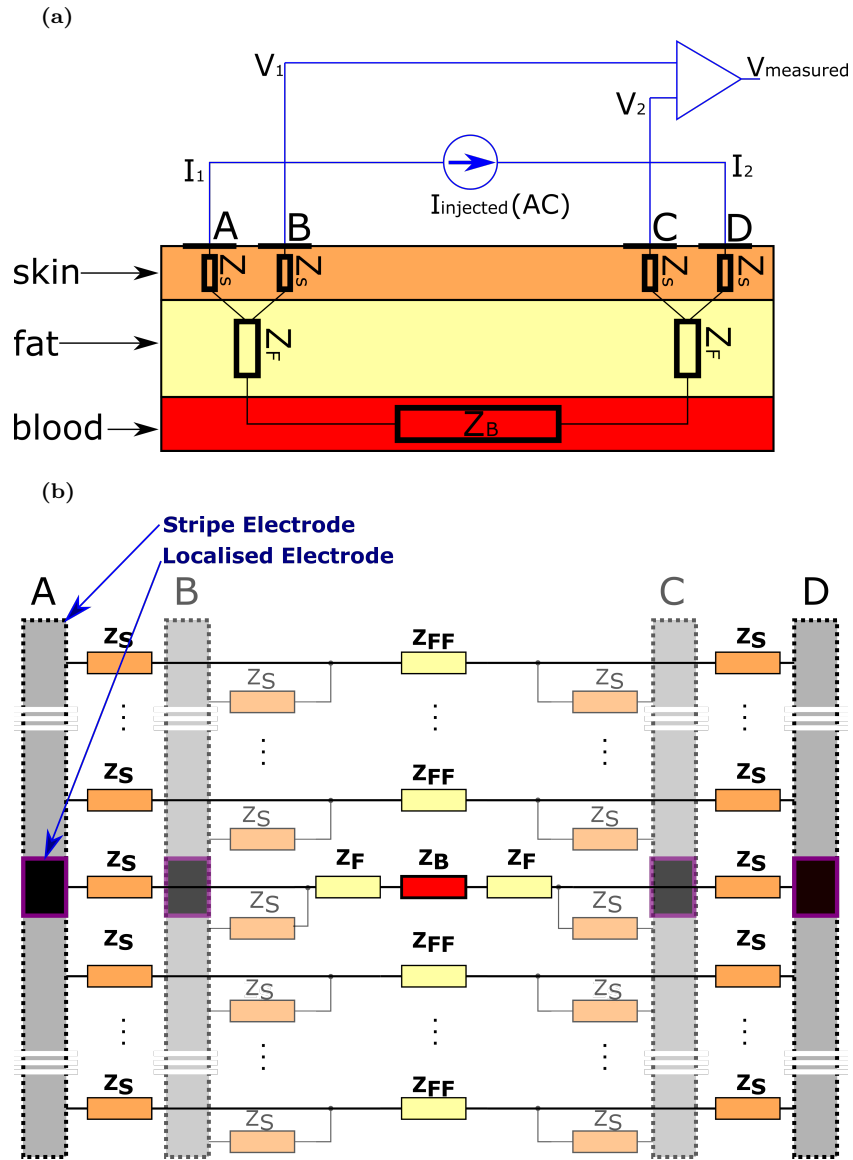


Figure 3.5: Simplified lumped impedance model. a) shows the simplified lumped impedance from the side, b) shows the simplified lumped impedance looking through the electrodes (top view)

value of Z_B can be assumed to change by $\pm 20\%$ from the baseline impedance corresponding to pulse related blood impedance variations [93, 100]. Therefore, Z_B is replaced by Z_b to represent the blood impedance with pulse related variations. The resulting variations to the overall impedance between A-D using localised vs larger stripe electrodes are calculated below. Localised electrodes impedance, using $2Z_S + 2Z_F = \alpha$, for clarity:

$$Z_{LOC} = \alpha + Z_b \quad (3.3)$$

Stripe electrodes impedance, using $2Z_S + Z_{FF} = \beta$ for clarity:

$$Z_{STR} = \frac{1}{(\frac{1}{Z_{LOC}} + \frac{n}{\beta})} = \frac{\beta(\alpha + Z_b)}{\beta + n(\alpha + Z_b)} \quad (3.4)$$

To calculate the sensitivity of a model the following equation [101] is used:

$$S = \frac{\frac{\partial x}{x}}{\frac{\partial p}{p}} \quad (3.5)$$

Here S is the sensitivity, x is the state variable, p is the parameter and ∂x and ∂p are the partial derivatives of the state variables and parameters. Applying the sensitivity equation to 3.3 with Z_B as the parameter result to:

$$S_{LOC} = \frac{\frac{\partial Z_{LOC}}{Z_{LOC}}}{\frac{\partial Z_b}{Z_b}} = \frac{\partial Z_{LOC}}{\partial Z_b} \frac{Z_b}{Z_{LOC}} \quad (3.6)$$

As $Z_{LOC} = \alpha + Z_b$ and $\partial Z_{LOC}/\partial Z_b = 1$, the sensitivity S_{LOC} can be written as follows

$$S_{LOC} = \frac{Z_b}{\alpha + Z_b} \quad (3.7)$$

Repeating the above for 3.4 gives:

$$S_{STR} = \frac{\frac{\partial Z_{STR}}{Z_{STR}}}{\frac{\partial Z_b}{Z_b}} = \frac{\partial Z_{STR}}{\partial Z_b} \frac{Z_b}{Z_{STR}} \quad (3.8)$$

Replacing Z_{STR} with 3.4 the sensitivity S_{STR} can be written as follows:

$$S_{STR} = \frac{\beta^2}{(\beta + n(\alpha + Z_b))^2} \frac{Z_b}{Z_{STR}} = \frac{\beta}{\beta + n(\alpha + Z_b)} \frac{Z_b}{(\alpha + Z_b)} \quad (3.9)$$

The ratio RLS of localised to stripe sensitivities yields:

$$RLS = \frac{S_{LOC}}{S_{STR}} = \frac{\beta + n(\alpha + Z_b)}{\beta} = 1 + \frac{n}{\beta}(\alpha + Z_b) > 1 \quad \forall Z_b \quad (3.10)$$

The fact that RLS is > 1 for all Z_b values indicates that localised electrodes will always exhibit higher sensitivity to blood impedance variations relative to their larger counterparts and thus research question 2 is theoretically justified by the above derivation.

3.5 SSVT scanning Sequence and Localised Measurements

The SSVT scanning sequence was first carried out in order to find out which electrode segments were closest to the blood vessel. In each measuring sequence the injecting electrode segment from group A was always combined with the neighbouring measurement electrode segment from B, while the same combination was always observed between segments in C and D (Fig. 3.4c). The eight segments at each electrode site were designated by the electrode site followed by segment number (eg: A_1). Thus for each SSVT measurement a pair $A_i B_i$ and a pair $C_j D_j$ were used, with i, j independently having values between 1 and 8. An example of this is shown in figure 3.4c where segment pair $A_1 B_1$ and its combination with all the $C_j D_j$ segment pairs is shown with dashed-red lines. A sinusoidal 10 kHz , 100 μA current was injected between A_i and D_j with B_i and C_j measuring the resulting voltage. The magnitude of the voltage between B_i and C_j was divided by the injected current magnitude to give the value of $|Z_{ij}|$ between the electrodes B_i and C_j . Each of the 8 $A_i B_i$ pairs was combined in turn with each of the 8 $C_j D_j$ pairs (dotted lines in Fig. 3.4c). The outcome of the sequence was thus an 8×8

matrix of 64 $|Z_{ij}|$ values as shown below in 3.11.

$$|Z_{ij}| = \begin{bmatrix} Z_{11} & Z_{12} & \cdots & Z_{18} \\ Z_{21} & Z_{22} & \cdots & Z_{28} \\ \vdots & \vdots & \ddots & \vdots \\ Z_{81} & Z_{82} & \cdots & Z_{88} \end{bmatrix} \quad (3.11)$$

When a scan is performed using SSVT, the length of the active tetrapole (ℓ_t) (i.e. the outer edge-to-edge distance between the current injecting electrodes as shown in fig 3.4c) varies. Even in a homogeneous volume, the tetrapole length (ℓ_t) variation is the main factor that introduces non-uniformity between the impedance values measured by each tetrapole [18]. Other factors include boundary conditions and the fact that in this case, the recording electrodes are not always in line with the current injection ones. To remove that scaling effect, each impedance value obtained from a SSVT tetrapole was divided by the length (ℓ_t) of that tetrapole. This approximate process significantly reduced the non-uniformity from the results. Subsequently, the values in the $|Z_{ij}|$ matrix were normalised between 0 and 100% and values lower than 10% of the resulting impedance range of the matrix were used to identify the electrodes closer to the vessel.

Localised measurements were performed by activating only the electrode segments from each group corresponding to lowest $|Z_{ij}|$ values, grouped to form the largest possible localised electrode covering only the area of interest. Each measurement was repeated with pseudo-stripe electrodes. Both the SSVT sequence and localisation were used in simulations and experiments.

3.6 FEM Simulations

Manufacturing phantoms controlling the electrical properties and accurately changing the orientation of the blood vessel was an elaborate time-consuming process. Implementing the different orientations in simulations would be quicker and would allow more precise control over different parameters. Using the electric currents (ec) module in COMSOL 5.3, FEM simulation was first implemented of a SSVT scan on a saline par-

allelepipiped model (conductivity of 1.55 S/m as measured previously), with identical dimensions to the geometric model and the phantom. In the ec module, quasi-static solutions of Maxwells equations were used to solve for the electrical potential. No electrode-electrolyte interface was included in the model. Electrode site A was assigned as a current terminal with a 1 A current being assigned as a boundary condition. Electrode site D was assigned as a ground terminal of zero potential. It was assumed that no current flows through the exterior boundaries of the phantom, as the exterior boundary was air which is a poor conductor of electric current. Electrodes B and C were assigned as boundary probes used to obtain the resulting potential, which was then used to obtain the transfer impedance. These simulations were performed to observe the impedance sensitivity distribution in a homogeneous volume and to verify that division by the tetrapole lengths (ℓ_t) allowed each data point to be scaled to the same level. Moreover, these simulations allowed for a performance comparison between the simulated stripe electrodes and the simulated as well as the experimental pseudo-stripe electrodes.

Further assessing research question (1), simulations were then carried out for eight models, with blood vessel cylinder orientations of $\theta = -20^\circ, -10^\circ, 0^\circ, 10^\circ, 20^\circ, 30^\circ, 60^\circ$ and 90° with respect to the longitudinal axis of symmetry of the electrode array. The values of $\pm 20^\circ$ were chosen so as to verify that the model produced similar results to the experiments. For each θ , simulations of SSVT sequence were carried out leading to the estimates of the values of the $|Z_{ij}|$ matrix for each model. Thus, allowing for the selection of the electrode segments close to the blood vessel in each case. The $|Z_{ij}|$ matrix was then divided by the lengths of the related tetrapoles (ℓ_t) to remove the electrode spacing influence from the measurement. By applying a 10% threshold from the overall change in the impedance value, the desired segments satisfying research question (2) could be identified. The 10% threshold was selected empirically, and it worked for all cases.

To assess research question (2) simulations were carried out for $\theta = -20^\circ$ with the blood conductivity being varied from its original value (700.04 mS/m) that corresponded to the experiments up to twice that value (1400.08 mS/m), in increments of 10%. Moreover, uniquely in the simulations, an additional calculation was carried out for each conductivity variation step of the blood vessel using stripe and pseudo-stripe electrodes,

to establish whether they perform similarly.

3.7 Experimental Setup

Once the multiple simulations were performed, the results obtained need to be verified experimentally. For this purpose, first, a circuit needed to be designed that could allow for the scanning sequence and localised measurements easily. To replicate the simulations in a controlled environment, it was decided to use anatomical phantoms that mimic the $\theta = \pm 20^\circ$ 3D models used in simulations. The design of the circuit, along with the related programs used for measurements, as well as the phantom design, are described below.

3.7.1 Circuit Design

The DRE system was designed to function according to the block diagram shown in figure 3.6a. A printed circuit board (PCB) was designed featuring the four segmented electrode sites, as illustrated in Fig. 3.3. The board was fitted with a 3D printed rectangular wall attached around the electrodes using epoxy glue, allowing the use of liquids on the electrodes without shorting any circuitry. The electrode addressing electronics were positioned on the bottom layer of the same PCB, to reduce the distance between the electrodes and the addressing circuitry. This served to minimise the influence of parasitics and noise in the impedance measurements and to further protect the latter from any accidental spillage of liquids. The addressing circuitry was developed for interconnecting and individually addressing the 32 segments of the DRE system and for interfacing the ones selected from each group A, B, C or D with the respective four channels of a tetra-polar impedance analyser (Keysight E4980A/AL Precision LCR Meter [102]). The requirements on the circuit, for real diagnostic use rather than for the static gelatine phantom scenario examined here, included minimal impedance contribution when active, fast switching and stable frequency response at the chosen carrier frequency. Fig. 3.6a shows the block diagram of the system, which was implemented through the circuit diagram shown in Fig. 3.6b and A.1. Switching between segments was carried out using

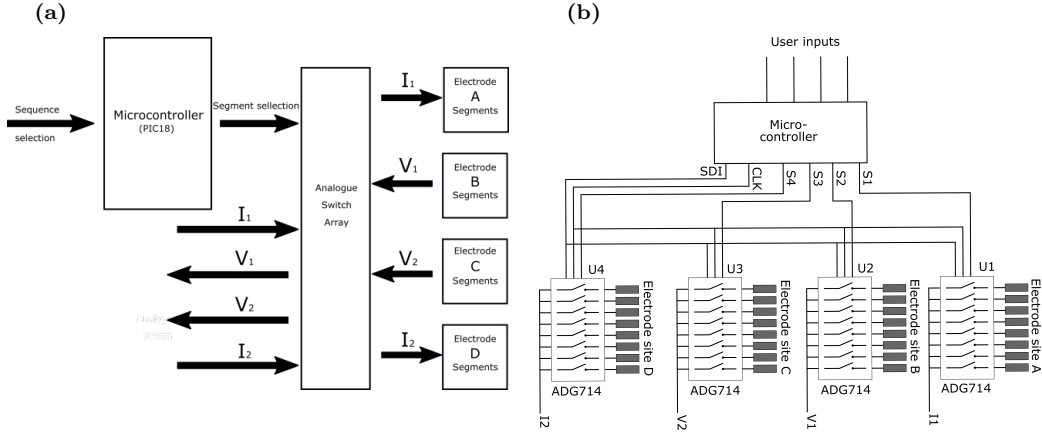


Figure 3.6: Circuit diagram, a) shows the block diagram for the complete system. b) shows the connections to and from the micro-controller and the switch connection for the electrode segments sites to their corresponding impedance measurement channel

four ADG714 eight switch IC analogue switches, featuring low on-resistance ($R_{on} = 2.5 \Omega$), and requiring about 28ns each to go from OFF state to ON and then OFF again. The ADG714 ICs were labelled 'U1' to 'U4'. To change the segment allocation an 8-bit binary word needs to be sent serially to the ADG714 IC, each bit of the byte corresponding to one switch in the IC. In order to send the byte of switching data, the address pin of the desired IC needs to be held low and then high again to implement the switching data. The ADG714 ICs were controlled by a PIC18F26K22 micro-controller, with the switching data transmitted through the serial peripheral interface (SPI) pins, allowing them to connect each of the electrode segments individually or in combinations to the respective LCR meter channels (I_1, V_1, V_2, I_2). The user could select the segment combinations through switches activating pre-programmed sequences in the micro-controller. The pre-programmed sequence was then triggered using push-buttons. Three main sequences were pre-programmed into the micro-controller; the first sequence shorted all the segments to form the pseudo-stripe electrodes, the second sequence was the SSVT scanning sequence, and the third sequence was the localised electrode sequence.

A user interface board was designed such that all external connections such as the power supply and the LCR meter connect to it. The ADG714 IC, requires $\pm 2.5 V$ and a reference to ground, whereas the PIC18F26K22 can handle a supply voltage from 2.3 V

to 5 V as the positive supply and ground. Therefore, three power supply connections were included, one for +2.5 V, another for -2.5 V and for 0 V as ground. The four channels from the LCR meter also connected to this board using BNC connectors. The BNC connections then connect to one side of DIP switches which was used to change the topology. The other connection of the switches were connected through a ribbon cable to the electrode PCB. A second DIP switch used to switch between the different functions in the micro-controller, along with two push buttons to trigger different parts of the functions. Lastly, a set of pads were also included in this PCB which were used to program the microcontroller shown in fig A.2. The two PCBs were connected using a ribbon cable which fits into the connector located at the edge of both PCBs.

3.7.2 Micro-controller Program

The Micro-controller used can be programmed using C language or assembly language. C language is a high-level programming language which is easy for the user to understand, which is then converted to machine language for microcontroller to understand them. Assembly language is closer to machine language and can sometimes be difficult to decipher. However, it allows the program to be designed in a more time-critical manner, as the language is written for each clock-cycle of the internal clock of the micro-controller. The advantage of using assembly language over C language is that: assembly language allows the user to dictate what happens at each clock-cycle, whereas C language translates the commands into assembly and then into machine language, which might not always be time critical. The programs for the micro-controllers used in this research were written in assembly language. The assembly programs are attached in the attached CD. The overall flow of the programs will be described using flowcharts.

At the start of the program, the inputs and outputs of the micro-controller and additional variables were set. This was followed by initialisation of serial communication protocols to enable serial communication between the micro-controller and the switches. The micro-controller then starts to check the inputs from the DIP switches. The DIP switches were used to switch between the different functions, which were programmed

into the micro-controller. The first two switches were used to enable and disable the micro-controller from accepting user inputs, as long as the first switch (SW1) was kept at logic 1 it disabled the other inputs. Only when the SW1 was set to logic 0 and switch two (SW2) was set to logic 1, would the other inputs be enabled. Once the other inputs are enabled, the micro-controller activates the function associated to that switch. The third switch (SW3) and fourth switch (SW4) were intentionally kept empty. The fifth switch (SW5) was used to enable the localised electrode segment activation function, which switched between localised segments and pseudo stripe segments when push-button one (PB1) or push-button two (PB2) were pressed. The sixth switch (SW6) was used to initiate the scanning sequence; every time PB1 was pressed the next state of the scanning sequence was implemented, while PB2 was used to reset the scan to its initial state. The full program is provided in the CD attached with the thesis.

3.7.3 Impedance Analyser Setup

The impedance analyser used to take impedance measurements was the Keysight E4980A precision LCR meter. The analyser was setup by going to the measurement set-up option, the measurement type was changed to give the real and imaginary "R + I" values, the frequency was set to 10 kHz , and the trigger was set to bus driven, allowing the analyser to be triggered through MATLAB. The impedance analyser contains four terminals which are labelled L_{cur} , H_{cur} , L_{pot} and H_{pot} . The L_{cur} and H_{cur} were used as the current injection (CC) channels and L_{pot} and H_{pot} were used as the voltage measurement (PU) channels. The channels were connected to the electrodes in the same order as those used in the simulations. The E4980A precision LCR meter was connected through USB to the laptop, and a MATLAB program was used to take impedance measurements and store them in an 8×8 matrix for further processing. The sampling time of the LCR meter was approximately 35 ms per impedance measurement.

3.7.4 Data Acquisition Program

Before any command could be sent to the E4980A precision LCR meter through the USB connecting using MATLAB, the address of the LCR meter must first be set up using the following command `E4980A = visa('agilent','USB0 :: 0x0957 :: 0x0909 :: MY46309532 :: 0 :: INSTR')`; and the buffer size and byte order was set using `E4980A.InputBufferSize = 388608`; and `E4980A.ByteOrder = 'littleEndian'`; commands. Using the `fopen(E4980A)`; command MATLAB tries to establish the connection to the LCR meter, if no response is received from the LCR meter MATLAB gives an error message. Once the connection is made different parameters of the impedance measurements such as the trigger type (internal, external, bus and manual), measurement type (magnitude-phase, real-imaginary, etc), frequency and number of samples can be set using the `fprintf = (E4980A, sprintf());` command. To trigger the impedance measurement the command `fprintf(E4980A,': TRIGger : IMMEDIATE')`; is used, and `C = textscan(query(E4980A,': FETCh : IMPedance : CORRected?'),'%f%f', 'Delimiter',' ');` imports the impedance values from the LCR meter and stored in the variable `C` and stored in separate variables `ReZ = C1`; and `ImZ = C2`; . The connection to the LCR meter can be disconnected by using the command `fclose(E4980A)`; . The above sequence of establishing the connection, setting the LCR meter parameters, taking impedance measurements and closing the connection were made into a function making it possible to trigger the LCR meter in other programs, shown in section B.1.1.

A function was made to store the impedance data in a matrix associated with the position of the electrodes. In it two for-loops were used to address the locations in the matrix, the first loop triggered the LCR meter and the impedance data obtained were stored at the address obtained from the second for-loop. The function was designed such that it waits for the user to press any key for each iteration of the loop. This was done as the electrode PCB requires user input to carry out the scanning sequence. The function for taking the impedance measurements and storing it is shown in section B.1.2.



Figure 3.7: DRE gelatin phantom comprising skin (yellow), fat (white) and blood vessel (red)

3.7.5 Gelatin Phantom Design and Manufacturing

The experimental setup featured gelatine phantoms constructed in accordance to the previously described biological model. The aforementioned dimensions, featuring skin and fat layers, with a cylinder representing a blood vessel embedded in the fat layer were used (fig 3.7). The phantoms were created using 3D printed moulds, where gelatine solutions with conductivities corresponding to each respective layer were poured into successively. The skin side of the phantoms was attached to the electrode PCB. To address research question (1), two phantoms P1 and P2 were constructed with their respective blood vessel cylinders placed at orientations of 20° and -20° relative to the axis passing across A-D through the array's centre (fig. 3.4a). These values represented the maximum angles that allowed the vessel to still be fully within the boundaries of the electrode area. To assess research question (2), five phantoms P2a-e, (variants of P2) were made with blood conductivity values between $700.04mS/m$ ($P2a \equiv P2$) and $1400.08mS/m$, in steps of 25%.

In order to prepare the phantom, first the saline was prepared in bulk of half a litre (0.5 l or 500 ml) for each layer that needed to be formed. Three solutions were made one each for the skin layer, fat layer and the blood layer. This was done to ensure that all phantoms had the same conductivity values. The NaCl concentrations in table 3.1 were adjusted to match the volume of the bulk solution. 30 ml of solution was taken from the bulk for each layer, and each of the layers were prepared one at a time. The solution was first heated till it reached $80^\circ C$ on a hot-plate, once the solution reached this temperature it was taken off the hot-plate and placed on a stirrer. 2.8 g of gelatin powder was then added to the heated solution, and stirred till all the gelatin powder dissolved in the solution. In this manner, the liquid gelatin solutions were prepared, and

Table 3.1: Different layers and their conductivity and concentration

| Layer | conductivity at 10 $KHz(\frac{S}{m})$ | Concentration per 100 $ml (g)$ |
|-------|---------------------------------------|--------------------------------|
| Skin | 0.00293 | 0.0014 |
| Fat | 0.042 | 0.02 |
| Blood | 0.70004 | 0.325 |

food colouring was used to make each layer easily distinguishable. Red food colouring was added to the blood solution, and for the skin layer, yellow food colouring was added. Once all the gelatin solutions were prepared, they were poured into the mould one layer at a time and left in the freezer at $-20^{\circ}C$ for 10 minutes for each layer. The phantom was completely ready when all the different layers were set. The moulds used to create the phantoms were 3D printed to match the required dimensions.

3.7.6 Experimental Procedure

For research question (1) and for each of the phantoms $P1$ and $P2$ described above, an impedance measuring sequence using DRE in SSVT mode was first carried out in order to find out which electrode segments were closest to the blood vessel.

For research question (2) impedance measurements were then performed on the five phantoms P2a-e, first activating only the electrode segments from each group corresponding to lowest $|Z_{ij}|$ values, grouped to form the largest possible localised electrode covering only the area of interest. Each measurement was repeated with pseudo-stripe electrodes. Between each measurement sequence, the electrodes were cleaned using ethanol to maintain good contact across the experiments and to remove any residue left over from the previous experiments.

Pseudo-stripe electrode (i.e. using all A_iB_i and C_jD_j electrode segments) measurements were also carried out on saline solution, poured inside the 3D printed wall over the electrodes so as to occupy the same overall volume with the gelatine phantoms. The conductivity of the saline used was $1.55 S/m$ as measured using Model 3540 pH/-conductivity meter. These measurements were carried out for comparison with FEM simulations also featuring a saline.

3.8 RESULTS AND DISCUSSION

Both experimental and simulation results are presented and discussed for each research question.

3.8.1 Initial Model Results

The results from the simulation on the initial model are shown in figure 3.8. The impedance measurements taken using each electrode length (ℓ_e) were normalised to the impedance measured at the original blood conductivity of their respective ℓ_e . Plotting the magnitude change in impedance for all the ℓ_e , showed that as the electrode lengths (ℓ_e) were reduced the magnitude variation of impedance increased. This shows that the sensitivity of impedance measurements increases as the electrodes were more localised to the vascular structure. These results led to the design of the Lumped-impedance simplified representation. The largest magnitude was obtained from the localised 3 mm electrodes. Therefore, it was decided to simplify the final model to have segmented electrodes with an overall ℓ_e of 8 mm, which would allow the scanning sequence to be quick as well as the electronics needed for experimental validation to be less complex. As it was decided to use a smaller length (ℓ_e) of electrodes the overall geometry of the model was reduced to those described in section 3.2.2 for the assessment of DRE system.

3.8.2 Research Question (1): Segment Identification

Factoring in the weighting factor for different size tetrapole formations

Applying SSVT to the FEM saline-only volume resulted in a $|Z_{ij}|$ matrix Z_{SSAL} which was then divided by the length ℓ_t of each corresponding tetrapole, i.e. the outer edge-to-edge distance between the current injecting electrodes, to remove the electrode spacing influence from the measurement (Fig. 3.9). dividing the two resulted to the normalised values that were within 3% of the average scaled value of the scaled Z_{SSAL} data-set. In figure 3.9, the AB in the legend refers to electrode segments at site A and B, and the number that follows is the segment number i . The x-axis represents the j position of

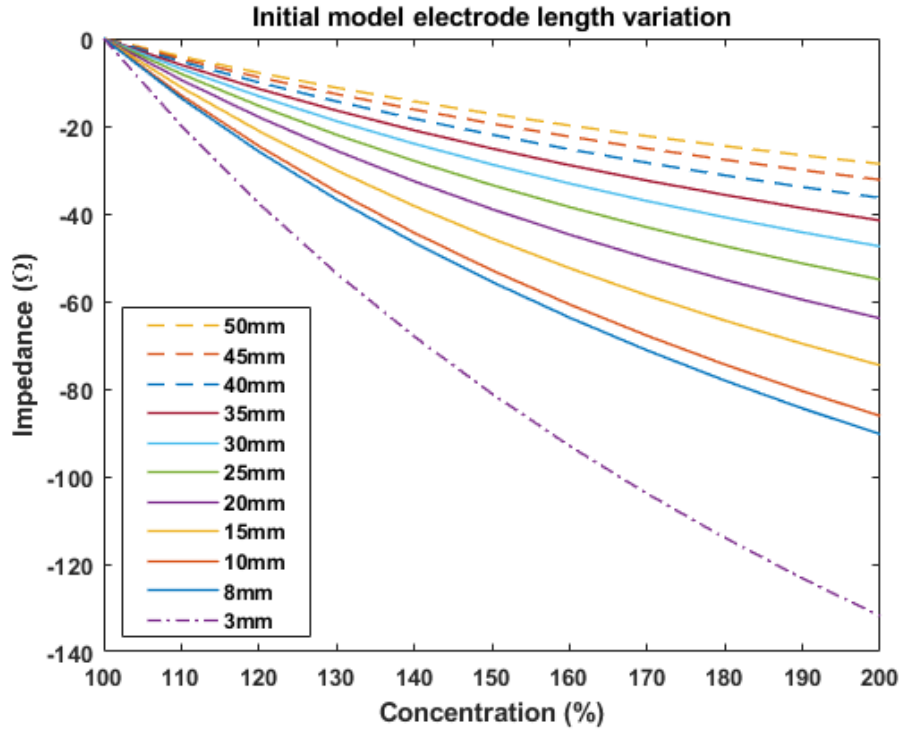


Figure 3.8: Conductivity variation with varying electrode lengths (ℓ_e). The impedance variation with respect to the variation of blood conductivity is measured using electrodes of different ℓ_e . As ℓ_e changes from 50 mm to 3 mm (localized) the magnitude variation in impedance increases, showing an increase in sensitivity.

electrode segments at site C and D; hence the x-axis is label as 'CD'. This labelling style will be used for all SSVT scan results shown in this chapter.

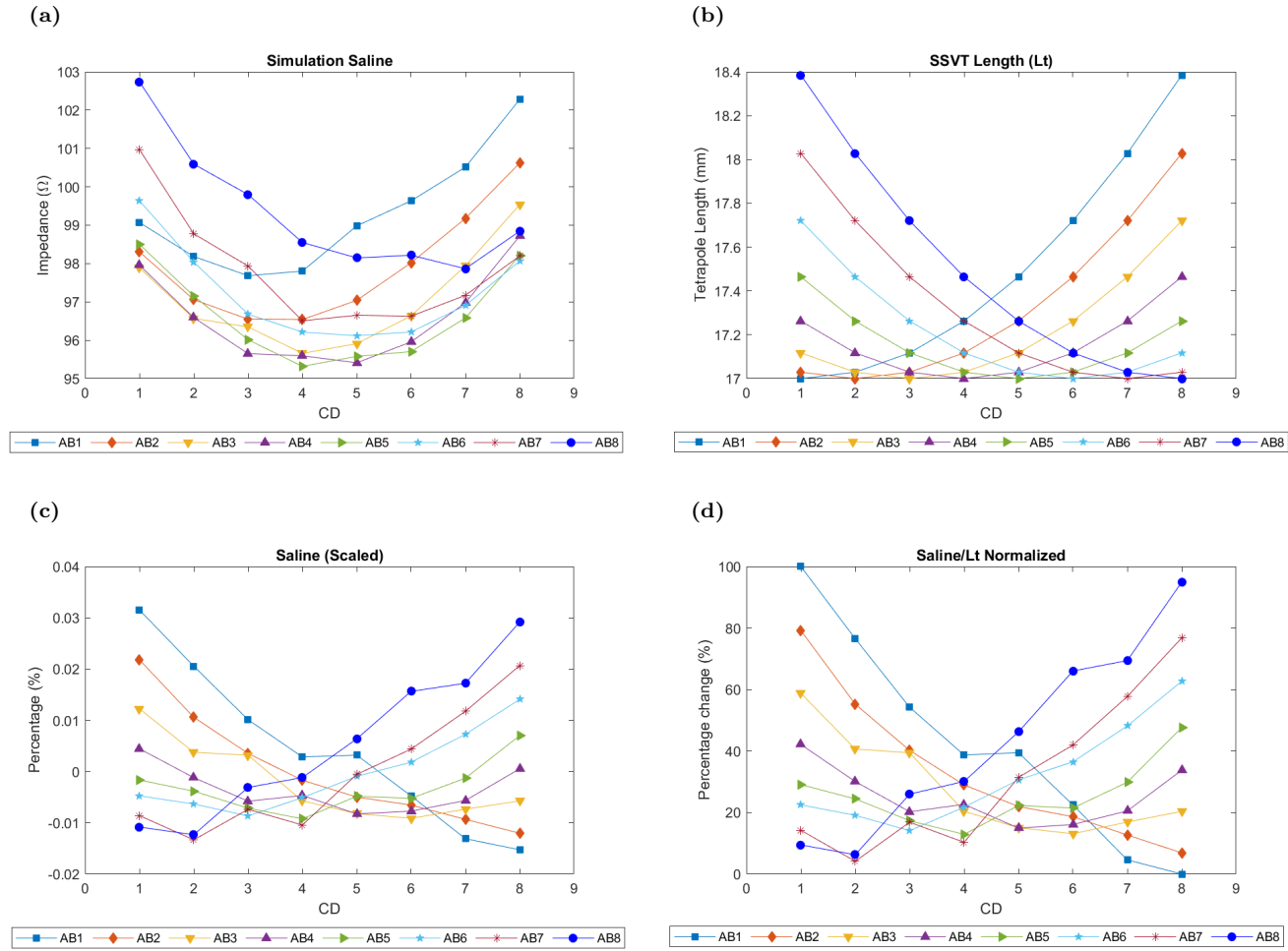


Figure 3.9: Scaling and Normalising data. a) saline SSVT data from simulation, b) Electrode tetra pole length ℓ_t , c) scaled data and d) normalised and scaled data.

Scanning and localisation

The scaling procedure (described previously) was applied to all SSVT scans for both the experimental and the simulation results. The scaled results were then normalised to a 0% – 100% range and by applying a 10% threshold the desired segments were identified as shown by the examples in fig. 3.10(a-d), fig. 3.11(a-d) and fig 3.12.

As the normalised figures indicate, the threshold could be used to identify the electrode pairs that correspond to the lowest impedance values. i.e. to the area over the blood vessel (top view). The ij combinations that were below the threshold shown in Fig. 3.13 for $\theta = -20^\circ$, together with the ij pairs geometrically located over the vessel labelled as overlapping segments. The outcome indicates a very close match of 85% with 12/14 segments matching. For all cases of θ considered, Table 3.2 summarises the comparison between all of the AB_i-CD_j pairs found to exhibit the lowest $|Z_{ij}|$ values after scaling and normalising the results versus those located over the corresponding blood vessel. In most cases the results are very closely matched with the geometrically overlapped values.

In non-controlled measurements, plotting the angle θ of each SSVT orientation ϕ vs the scaled normalised data provides an approximate value for the angle θ . This is shown in Fig. 3.14 for the $\theta = -20^\circ, 0^\circ, 20^\circ$ cases where the lowest $|Z_{ij}|$ values exhibit minima at respective $\phi = -16.5^\circ, -3.4^\circ, 0^\circ, 3.4^\circ, 16.5^\circ$. These values are within 83% and thus approximately near the θ cases considered.

The scanning and localisation function of the system have been successfully demonstrated using the idealised model used here. It is worth mentioning that it does not take into consideration the an-isotropic properties of muscle layer and the insulating properties of bone, or the influence of neighbouring vascular structures.

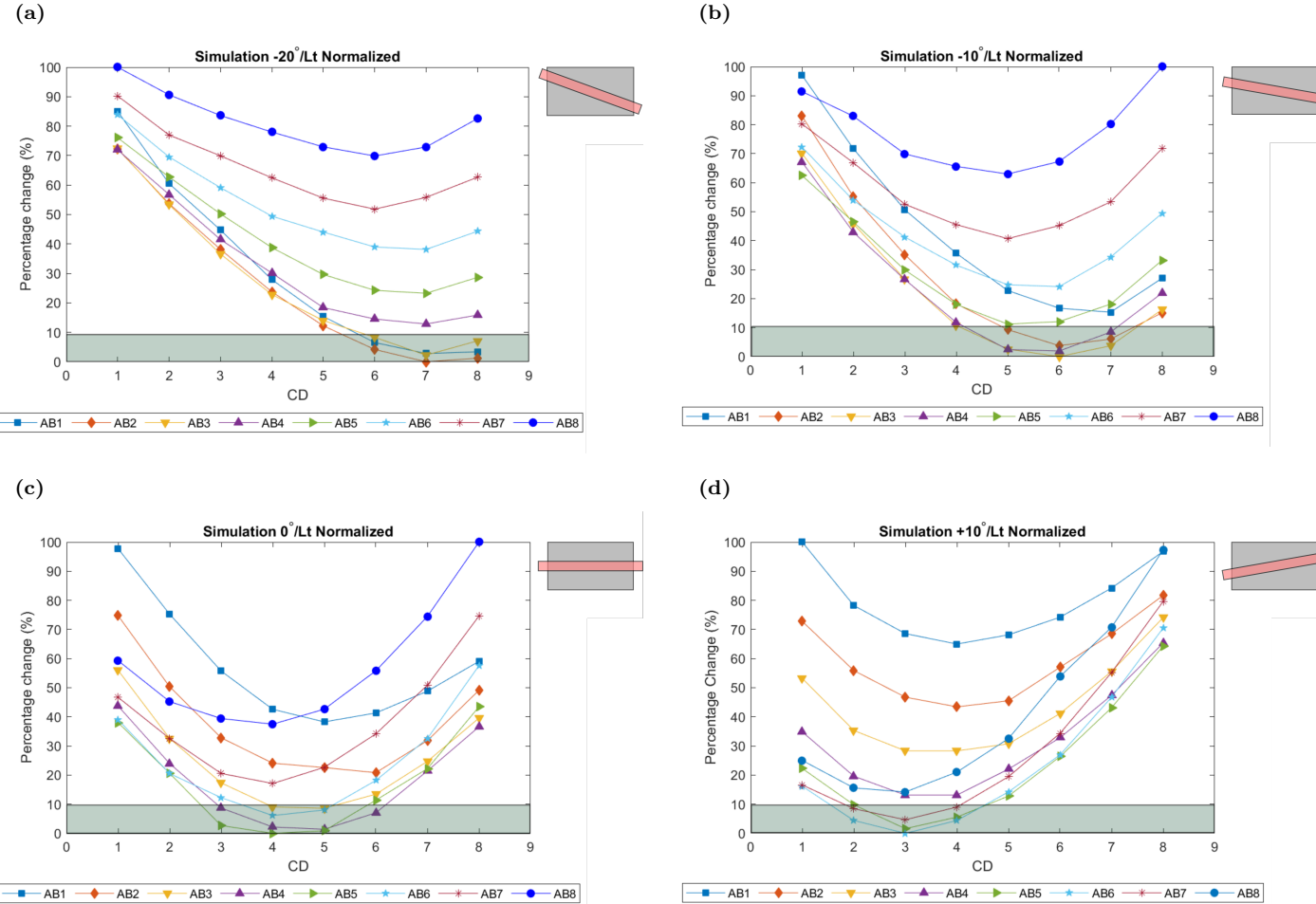


Figure 3.10: Blood vessel detection process (simulation data). a-d) show the scaled and normalised simulation scan data for (-20° , -10° , 0° and 10°) orientation data, with a threshold of 10% of the maximum impedance. following the steps shown in fig 3.9

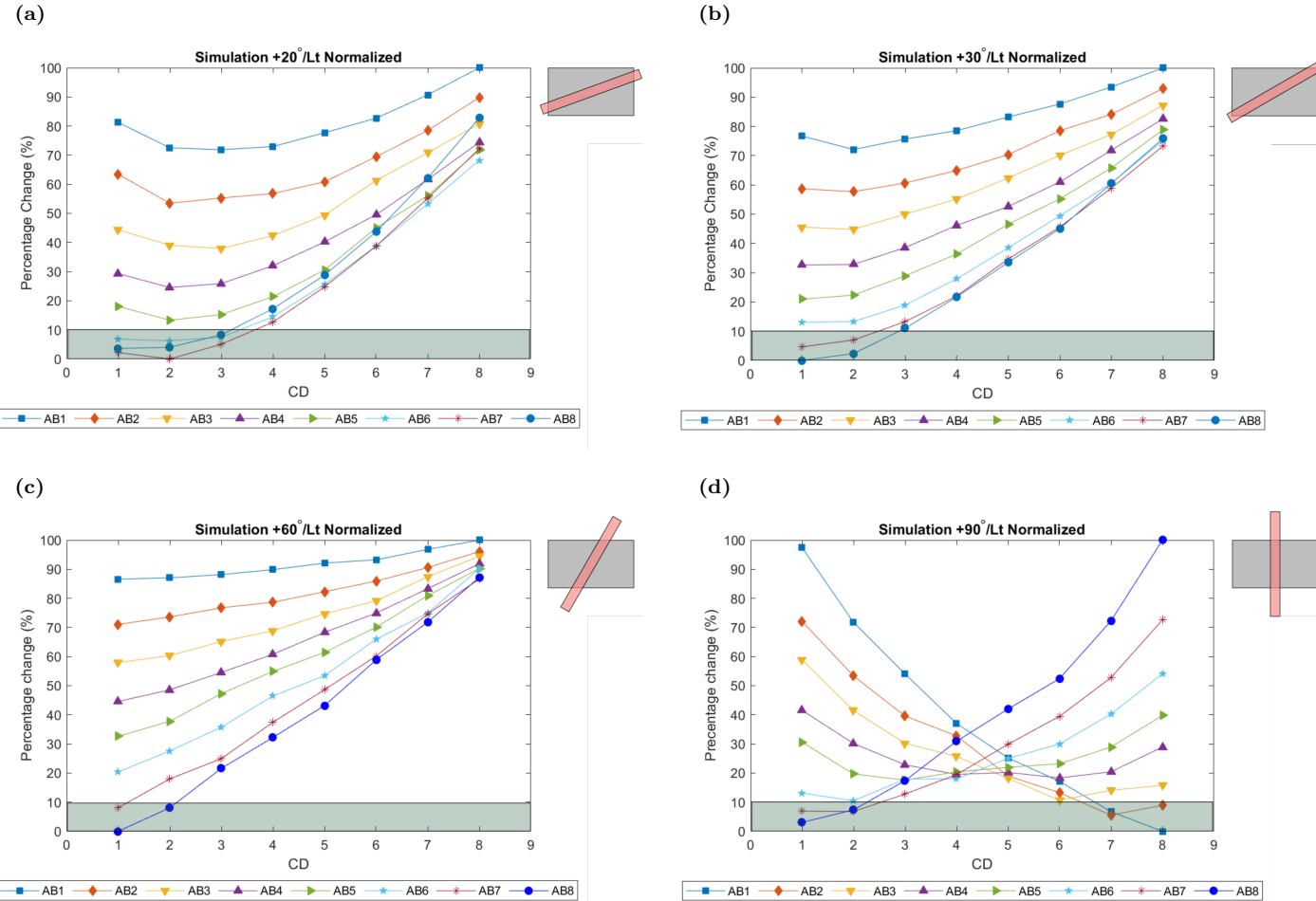


Figure 3.11: Blood vessel detection process (simulation data). a-d) show the scaled and normalised simulation scan data for (20°, 30°, 60° and 90°) orientation data, with a threshold of 10% of the maximum impedance. following the steps shown in fig 3.9

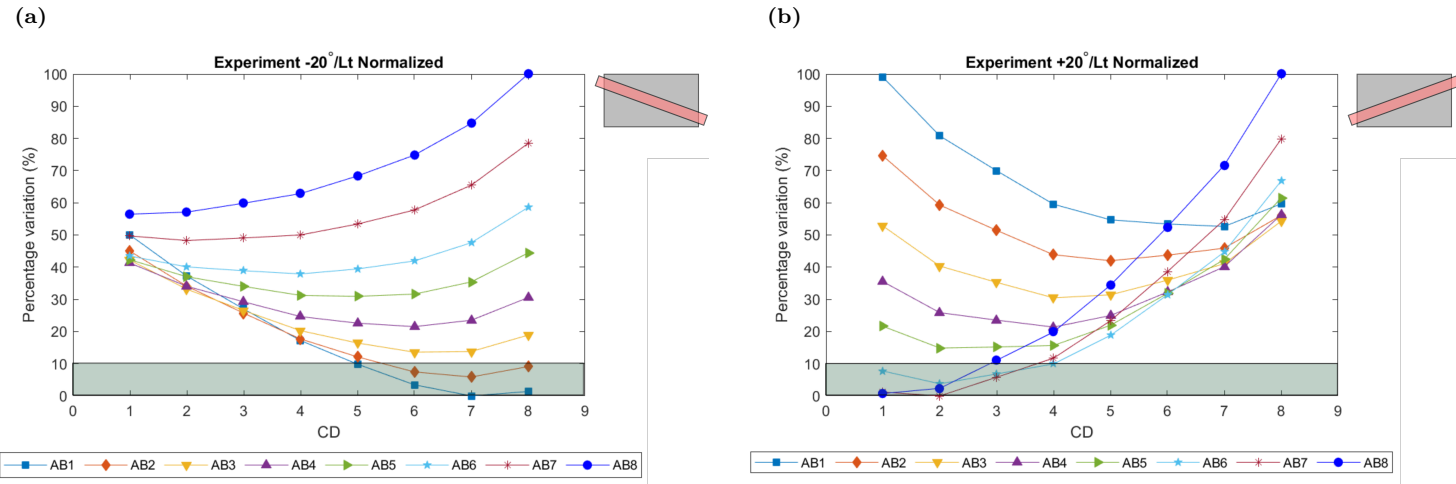


Figure 3.12: Blood vessel detection process (experimental data). a-b) show the scaled and normalised simulation scan data for (-20° , and 20°) orientation data, with a threshold of 10% of the maximum impedance. following the steps shown in fig 3.9

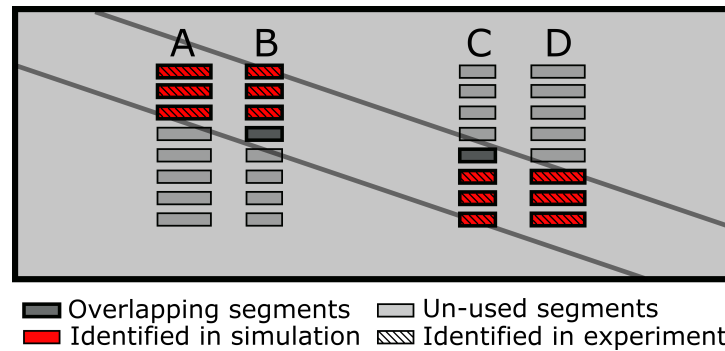


Figure 3.13: Scan result plotted against electrode segments used to obtain results for detecting electrode segments overlapping the blood vessel

Table 3.2: Expected segments vs identified segments

| θ | Simulation | | Experiment |
|-------------|--|--|----------------------------------|
| | Overlapped | Identified | Identified |
| -20° | $AB = 1\ 2\ 3\ 4$ $CD = 5\ 6\ 7\ 8$ | $AB = 1\ 2\ 3$ $CD = 6\ 7\ 8$ | $AB = 1\ 2$ $CD = 6\ 7\ 8$ |
| -10° | $AB = 2\ 3\ 4$ $CD = 5\ 6\ 7$ | $AB = 2\ 3\ 4$ $CD = 5\ 6\ 7$ | No Data |
| 0° | $AB = 3\ 4\ 5\ 6$ $CD = 3\ 4\ 5\ 6$ | $AB = 3\ 4\ 5\ 6$ $CD = 3\ 4\ 5\ 6$ | No Data |
| 10° | $AB = 5\ 6\ 7$ $CD = 2\ 3\ 4$ | $AB = 5\ 6\ 7$ $CD = 2\ 3\ 4$ | No Data |
| 20° | $AB = 5\ 6\ 7\ 8$ $CD = 1\ 2\ 3\ 4$ | $AB = 6\ 7\ 8$ $CD = 1\ 2\ 3$ | $AB = 6\ 7\ 8$ $CD = 1\ 2\ 3$ |
| 30° | $AB = 1\ 2\ 3$ $CD = 6\ 7\ 8$ | $AB = 1\ 2$ $CD = 7\ 8$ | No Data |
| 60° | $AB = 1\ 2$ $CD = 7\ 8$ | $AB = 1\ 2$ $CD = 7\ 8$ | No Data |
| 90° | $AB = \text{None}$ $CD = \text{None}$ | $AB = 1\ 2\ 7\ 8$ $CD = 1\ 2\ 7\ 8$ | No Data |

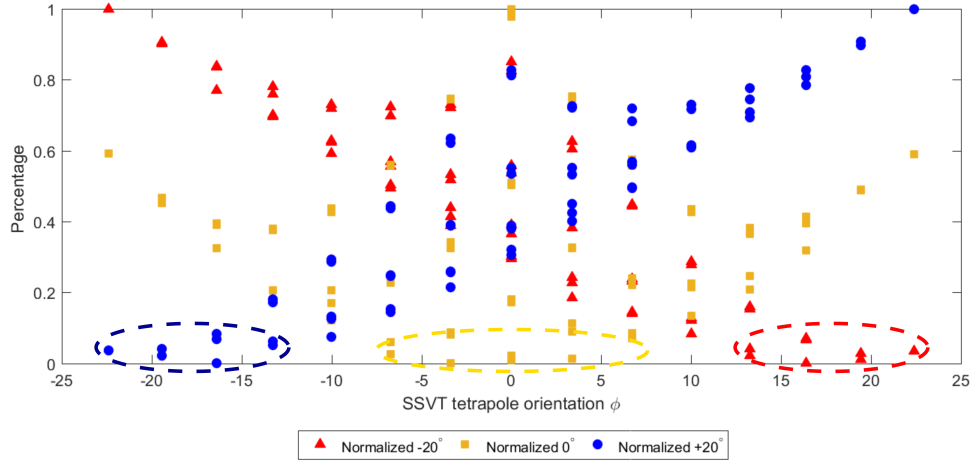


Figure 3.14: SSVT orientation ϕ vs the scaled normalized data

3.8.3 Research Question (2): Measurement Sensitivity

Pseudo- stripe vs full size stripe

The simulation results on saline solution with stripe and pseudo-stripe electrodes demonstrated that the impedance for both types of electrodes was very similar: the simulated impedance for the stripe and for the pseudo-stripe electrodes for saline was $114.88\ \Omega$ and $115.41\ \Omega$, respectively. The small difference of less than 1% between the two values leads to the conclusion that the pseudo-stripe electrodes emulate satisfactorily their equivalent stripe electrodes. Experimentally, the saline solution impedance was measured with an LCR meter and it was found to be $122\ \Omega$. The difference of about $7\ \Omega$ with respect to the simulated value was attributed to the resistance introduced by the switching circuit.

It is expected that an increase in blood conductivity will result in a decrease of the total skin-fat-blood vessel impedance, and vice versa. Fig. 3.15 illustrates simulation results of the aforementioned blood conductivity variations worked out for stripe versus pseudo-stripe electrodes. The results are similar within 0.01% for all concentration steps, highlighting further the similarity in performance between full solid stripe electrodes and the grouping of segments covering a similar outline area.

Monitoring blood variations with localised vs. pseudo-stripe electrodes

Fig 3.16 illustrates the performance of localised electrodes comprising the selected ij pairs for $\theta = -20^\circ$ in the previous section, compared to pseudo-stripe electrodes in detecting such impedance changes, both with simulations and experimentally. The impedance measurement using the DRE localised electrodes overlapping the blood vessel is not the same as that monitored by the pseudo-stripe electrodes. The localised impedance measurements exhibit a larger decrease as a function of blood conductivity than when pseudo-stripe electrodes are used. A similar behaviour, albeit with a smaller relative difference, is observed in the simulation results. The overall conclusion from these measurements is that localised electrodes exhibit significantly higher sensitivity to blood variation. In fact, absolute impedance change for each concentration step change is 25% higher for localised versus pseudo-stripe electrodes in simulations, while the correspond-

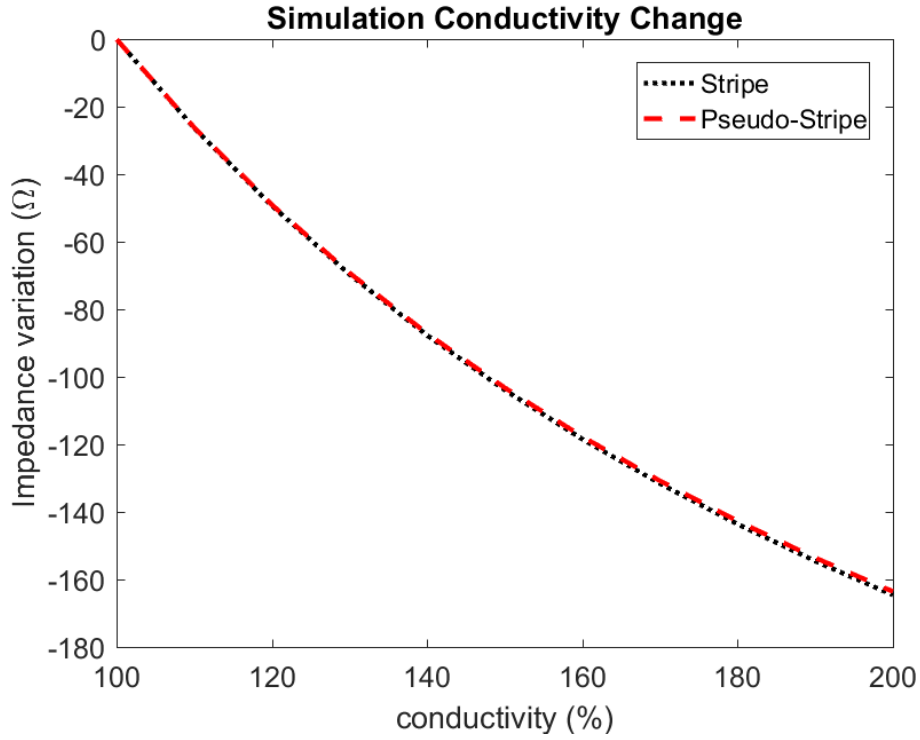


Figure 3.15: Conductivity vs impedance plot for Stripe vs pseudo-stripe electrodes to measure impedance while changing conductivity of blood from 100% conductivity to 200% conductivity

ing experiment results exhibit a 22% – 28% improvement. While this is a smaller variation than the one demonstrated in the theoretical lumped impedance model, the electrode length ℓ_e assumed in that model would have been significantly larger for the field lines to pass straight between the injecting electrodes. Therefore it is commendable that, based on the achieved outcome, the localised electrodes exhibit higher sensitivity even when compared to relatively smaller stripe electrodes such as the ones examined here. This indicates that the performance improvement over significantly larger electrodes (eg: band electrodes) will be even more pronounced.

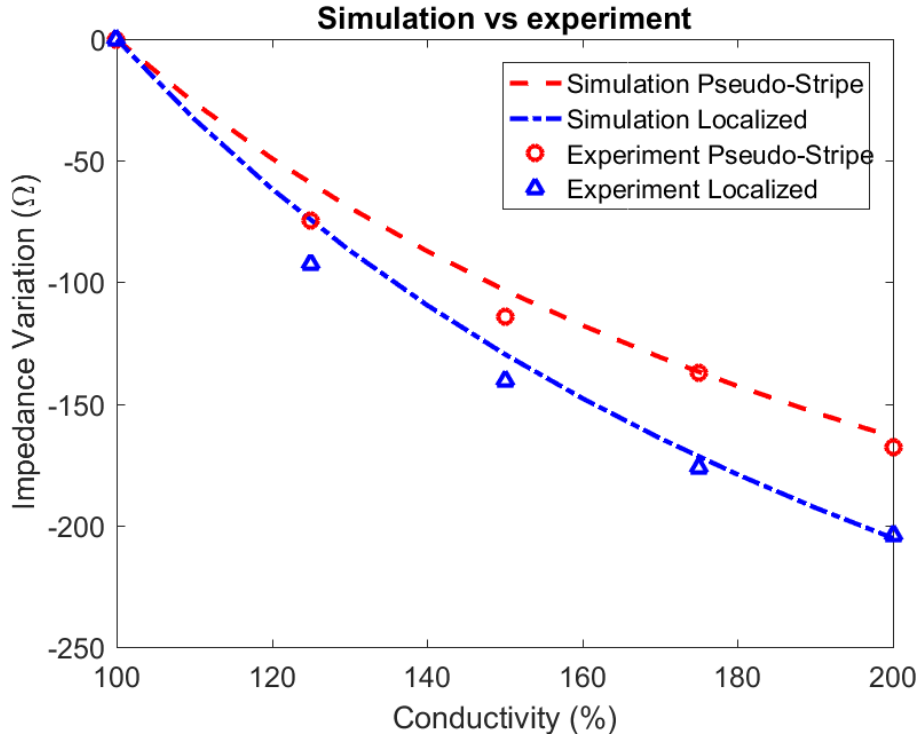


Figure 3.16: Conductivity vs impedance plot for simulation and experimental results, using different types of electrodes to measure impedance while changing conductivity of blood from 100% conductivity to 200% conductivity

3.9 Conclusion

In this chapter, it was verified that multiple small electrode segments could be combined to emulate large electrodes. It was also demonstrated that simple structures such as a straight blood vessel could be detected with the help of a simple scan using individual segments. From these scans, the electrode segments overlapping with the blood vessel were identified, which were then used for taking localised measurements. Through simulations and experiments, it was observed that localised electrodes had a higher sensitivity than pseudo-stripe electrodes. Even though simple structures could be identified using the scanning sequence described in this chapter, complex structures such as curved vessels would be difficult to detect accurately. Positioning and placement of the segmented electrodes also play an important role; they still need to be positioned over the struc-

ture of interest. To overcome the limitations of segmented electrodes identified in this chapter, it was decided to replace the segmented electrodes with a two-dimensional array of electrodes. In the next chapter, the use of an electrode array to scan and detect structures will be explored using experiments and simulations.

Chapter 4

Intelligent Re-configurable Electrode Method (IREM) Simulation

In the previous chapter it was shown - through experiments and simulations - that it is possible to create electrodes of varying effective areas by combining smaller electrode segments together. It was also shown that electrodes localised to the structure identified through a simplified scan were more sensitive to conductivity changes than pseudo-stripe (larger) electrodes, making it useful for taking impedance plethysmographic measurements. However, the segmented electrodes used in the previous chapter suffer from the following limitations: the tetrapole dimensions are fixed (on sites A-D); the vessels that are "detectable" have to exhibit orientations of up to $\pm 20^\circ$ while passing from the tetrapole's centre, therefore limiting the scanning and detection area; and they do not facilitate identification of vessel features and possible occlusions. In order to be able to move towards detection of occlusions, it is necessary to be able to scan the whole area covered by the electrodes and use some imaging techniques to identify the features of a vascular structure and its morphology. It is also desirable to avoid the need for any alignment of the vessel or the features to be detected with the electrode area centre. Therefore, the use of an array of electrodes was explored, in an attempt to increase the

scanning area, allowing greater flexibility in electrode grouping and increasing scanning options.

In this chapter, the possibility of using electrode arrays to enhance the detection of vessel features will be explored in detail. The effect of different electrode array geometries, different vessel parameters and scanning methods will be explored through FEM simulations. The optimum electrode array dimensions, their limitations as well as the ideal scanning sequence to detect structures transcutaneously will also be looked into. An imaging technique will be used to extract features of the vascular structures.

4.1 Method

As mentioned earlier, imaging using impedance measurements are mainly called EIT. These images usually comprise of a cross-sectional area of the sample under test. However, EIT lacks spatial resolution, and this is mainly due to the electrode size and positioning. In EIT, electrodes are positioned around the circumference of the body, mainly used to generate images of organs such as the heart and lungs [18, 47, 59, 60]. Impedance measurements for scanning and detection of blood vessels have yet to be documented, resulting in a lack of specifications on the optimum electrode geometry. This lack of specifications makes it necessary to explore these parameters to identify the optimum electrode geometries.

The simulations implemented in this chapter were divided into four stages. These stages were carried out incrementally, assessing different model parameters and electrode configurations. For stage 1, a 3D model hereafter referred to as model A was used. Model A was a simplified structure consisting of a rectangular homogeneous volume (fat) with a small cylindrical tube of higher conductivity (blood vessel) embedded at a shallow depth. This model was designed to have its length and width matching that of the final model used in the previous chapter. In stage 1, the segmented electrodes were replaced with an array of electrodes covering the same approximate area. The rationale behind using the array of electrodes was to verify the validity of the novel scanning method to detect the embedded tube and to re-assess the pseudo-stripe electrodes grouping and custom

localised electrode groupings in the electrode array. In stage 2, model A was altered by adding a layer of low conductivity (skin) in between electrode array and the fat layer. The overall model dimensions and the number of electrodes in the array were increased. This altered model was called model B. Here, different parameters such as the diameter and depth of the blood vessel, and the size and inter-electrode spacing of the electrodes were varied. The rationale behind stage 2 was to identify the minimum detectable blood vessel parameters, as well as the optimal electrode dimensions and spacing for detecting blood vessels at greater depths.

Stage 3 was a 2D simulation, the design of which was based on the cross-section of the model B. Therefore, it comprised of two main layers (skin and fat), with eight electrodes on the outer layer of the skin layer. Taking the two extremes, the blood vessel was introduced into the model with a parallel and perpendicular orientation. The rationale behind the 2D simulations was to identify the influence of increasing inter-electrode spacing between the measurement electrodes on the depth of detection. For these simulations, the thickness and depth parameters of the blood vessel were varied, while the spacing between the measurement electrodes was increased, keeping the spacing between the injection and measurement electrodes constant. Through these simulations, the minimum electrode dimensions and inter-electrode spacing were confirmed for detecting the blood vessel of interest. These electrode dimensions and inter-electrode spacing were then used to design the main 3D model to be used for detecting the carotid artery in stage 4.

The main 3D layout (main model) was designed to be anatomically idealised, with the electrode array comprising of the identified electrode dimensions. On this new design, a more complex scanning sequence was implemented to identify the vessel parameters that could be extracted from them. The results from the scanning sequence were then used to identify the different properties of the blood vessel such as its diameter, orientation and features such as bifurcations in it. Additional simulations with more complex models including: variation of vessel depth, vessel diameter, vessel orientation, and adding a bifurcation to the blood vessel to test the detection algorithm were also implemented. To better detect the bifurcation, the dimensions of the model and array size were ex-

Table 4.1: Summary of different simulation stages

| Stage | Model Name | Varying Parameters | Rationale |
|-------|------------|--|--|
| 1 | A | <ul style="list-style-type: none"> - Simplified can - Pseudo-stripe grouping - Localised electrode grouping | <ul style="list-style-type: none"> - Possibility to detect vessel with electrode array - reassess the results from Ch3 with the electrode array |
| 2 | B | <ul style="list-style-type: none"> - Vessel diameter - Vessel depth - Electrode size - Electrode spacing - Electrode grouping and positioning | <p>For the electrode array used here to identify:</p> <ul style="list-style-type: none"> - minimum detectable vessel diameter - maximum detection depth - influence of electrode size on impedance - influence of electrode spacing on impedance - influence of electrode grouping and its positioning on impedance |
| 3 | 2D | <ul style="list-style-type: none"> - Parallel and perpendicular electrode/vessel orientation - Inter electrode spacing between measurement electrodes - Vessel depth & diameter | <ul style="list-style-type: none"> - Assess the influence of orientation on impedance - Assess the detection capabilities of different inter electrode spacing |
| 4 | Main | <ul style="list-style-type: none"> - Different scanning sequences - Vessel orientation - Vessel depth and diameter - Vessel feature (Bifurcation) | <ul style="list-style-type: none"> - To create a more accurate scanning and detection sequence - to assess the capabilities of the scanning sequence for detecting the : <ul style="list-style-type: none"> * Vessel orientation * Vessel detection at different depths * Vessel feature identification |

panded, while keeping the electrode dimensions and inter-electrode spacing constant. The complex scanning sequence was then applied using the expanded array to get a more detailed scan of the bifurcation. The summary of all the four stages is given in table 4.1.

Later in this chapter, the different stages will be described in detail. For each stage, the model parameters, the simulation procedure and their results will be described before moving to the next stage for clarity and continuity.

4.2 Electrical Impedance Calculation in Simulation

To simulate the impedance measurements in COMSOL 5.3, the electric currents section of the AC/DC module was used, which uses quasi-static solution of Maxwells Equations to solve for the electrical potential. Since the electrodes were used as only entry and exit points, the electrode-electrolyte interface impedance was not implemented. For these simulations, the tetra-polar electrode configuration was used. In this configuration, four electrodes were used, two electrodes for injecting current (CC) and the other two for measuring the resulting potential (PU). To assign the CC electrodes, one electrode is assigned as terminal with a current of 1 A, and the other was set to ground, as the return point for the current. The PU electrodes were set by assigning the remaining electrodes as voltage probes 1 and 2. The voltage probe measures the voltage at the specified boundary. Subtracting the values obtained from the two probes and dividing it with the applied current of 1A gives the transfer impedance.

4.3 Stage 1: Simplified Design

4.3.1 Intelligent Re-configurable Electrode Method (IREM) Pixelated MEA Setup for Model A

For the IREM setup A 3D model was designed in COMSOL 5.3 software, with a parallelepiped layer of fat with 4 mm depth, 20 mm height and 45 mm width. A cylinder positioned diagonally at a depth of 1 mm away from the top was positioned inside the fat layer, representing a blood vessel on model A, the stripe electrodes were replaced by an array of 8x16 round electrodes with a diameter of 0.6 mm (Fig 4.1). The array was designed such that two columns of 8 electrode pixels would equal the size of the stripe PU electrodes. The spacing between the elements of the array was setup to be 1 mm centre to centre from the adjacent electrodes. This was done so that the array would cover the same area as the previously used stripe electrodes.

The next set of simulations was carried out in order to assess the ability of the IREM array to identify the location of the blood vessel. For this purpose, impedance measure-

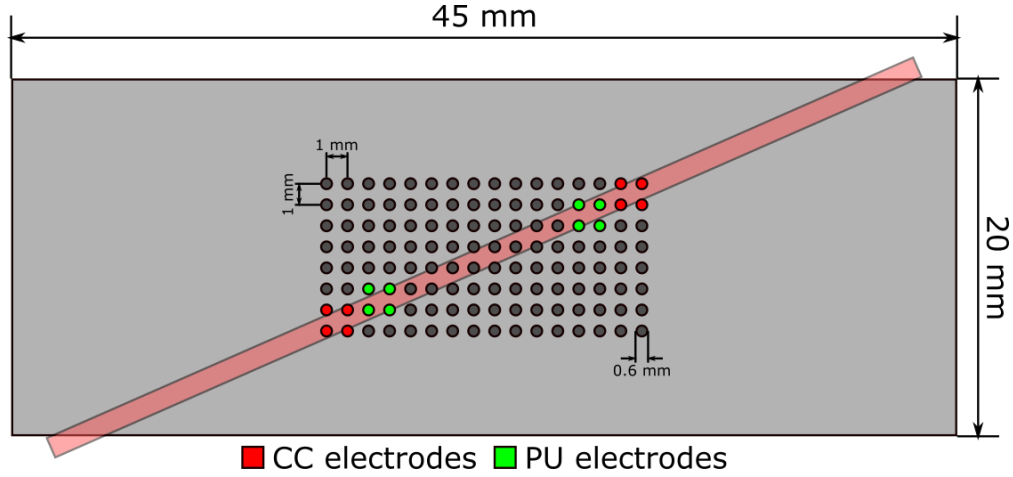


Figure 4.1: Model A with IREM array and localised electrode configuration. Shows the fat and blood vessel layers, with the IREM array of 8x16 electrodes with their dimensions. It also shows the CC electrodes (Red), PU electrodes (green), with their position and shape localised on the blood vessel.

ments need to be taken from the entire area covered by the array. This simulation was carried out by keeping the conductivity of blood constant and selecting four electrodes horizontally adjacent to one another to take the measurement. The electrode selection was then changed to the next four electrodes vertically below the previously selected electrodes before taking the next measurement. Similarly, measurements were taken from all possible horizontal electrode pairs throughout the electrode array, as shown with black arrow in figure 4.24. In this manner, the simulation virtually scanned the entire area covered by the array.

4.3.2 Localised Impedance Simulation.

The results from the scan carried out with the IREM setup (shown in the next section - Fig. 4.2), identified the location and the optimum number of pixels positioned above the blood vessel, thus allowing the formation of the tetra-polar localised electrode configuration shown in Fig. 4.1. Each localised electrode consisted of four pixels. Two columns of electrode pixels were also grouped together to form pseudo-stripe electrodes. A parametric sweep was set up, which increased the conductivity of blood from its original value by 0.005S/m until the conductivity of blood was increased to 0.05S/m over

the original conductivity. The sweep represents variations of blood analytes (e.g. ions) that would be measured by a trans-cutaneous EIS system. Its purpose was to allow for the localised electrode sensitivity to be assessed in comparison to that of conventional electrodes. Localised electrode tetrapole and pseudo-stripe electrode tetra-polar were then used to compare variations in impedance due to the parametric sweep.

4.3.3 Results: Model A

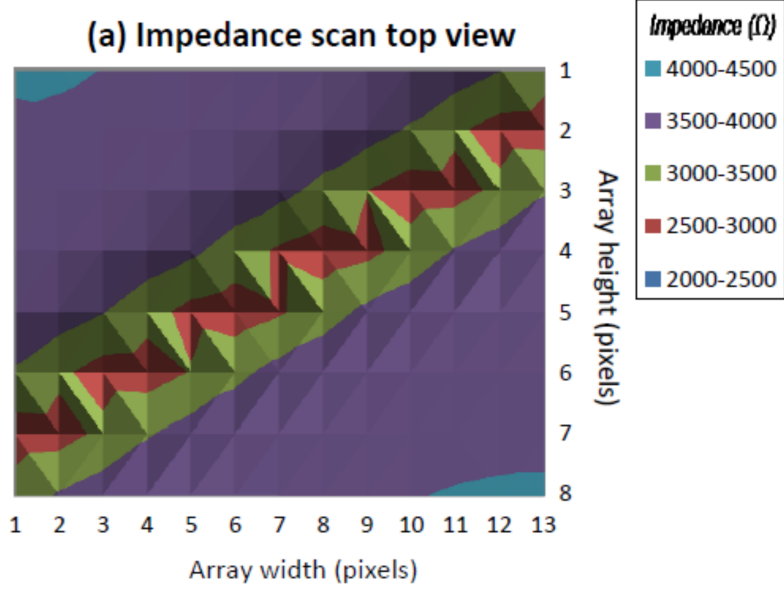
Multi electrode scan

The results from the scan were plotted to visualise the impedance of the area under the array (Fig. 4.2). From the plot it can be seen that the area where the blood vessel was located exhibited lower impedance from its surroundings, due to the high conductivity of blood which allows the majority of the injected current to flow through it, hence reducing the impedance measured locally by the SPVT scan. In that manner, the approximate location of the blood vessel could be identified, allowing for the selection of electrode pixels positioned above it to be grouped to form localised electrodes towards a more localised impedance measurement.

Localised electrode results

The parametric impedance variation was applied to both the pseudo-stripe electrode tetra-polar configuration and to the localised electrode tetra-polar configuration that was formed following the sweep described above. Measurements plotted in fig. 4.3 are normalised to start from the respective baseline impedance measurement for each of the two configurations. The results for the pseudo-stripe electrodes show that for each increment in conductivity of blood by 0.005S/m there was a decrease in measured impedance of approximately $2.86\Omega \pm 0.03\Omega$. For the same conductivity step, the localised electrodes exhibited a decrease in measured impedance of approximately $5.32\Omega \pm 0.06\Omega$. This is almost double the change in impedance measured using the pseudo-stripe electrodes. Thus, the comparison clearly indicates that the localised electrodes can greatly improve the sensitivity of EIS for trans-cutaneous blood analysis, re-confirming the results ob-

(a)



(b)

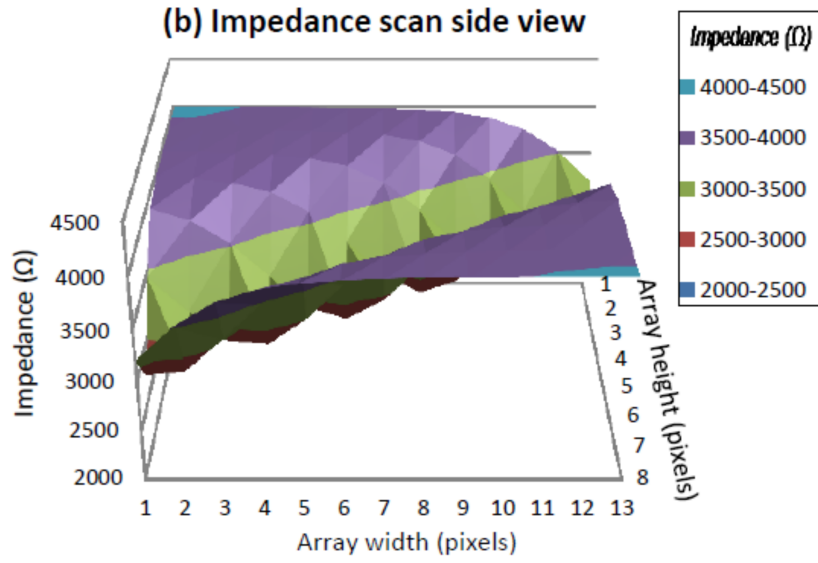


Figure 4.2: Model A: impedance scan plot, a) top view, b) side view. The location of the low impedance subcutaneous blood vessel through the high impedance fat layer is clearly detectable, especially in (a).

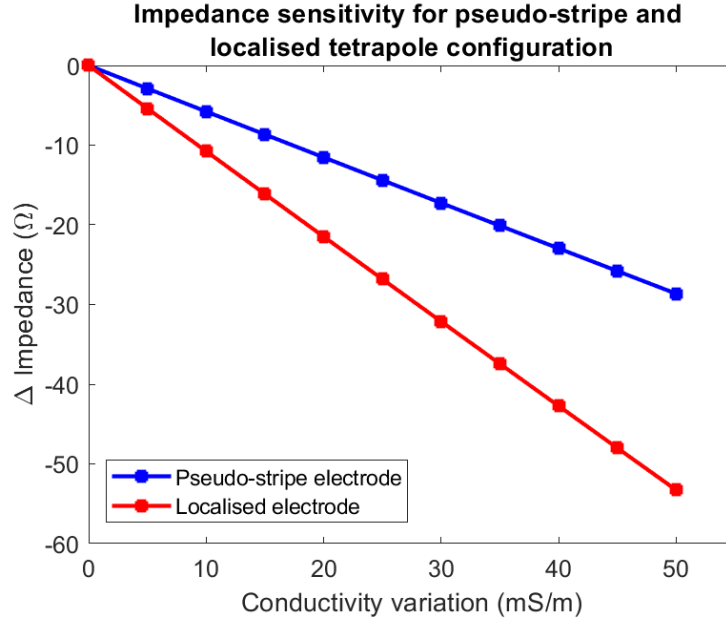


Figure 4.3: Model A: comparison of both tetra-polar configurations in terms of their respective impedance sensitivity normalised to their respective baseline values. The impedance variation was a result of the same parametric conductivity sweep applied to the model.

tained with DRE.

4.4 Stage 2: Parameter Identification

4.4.1 Simulation Setup

For this simulation, a 3D model comprising a rectangular block with 7 *mm* depth, 30 *mm* width and 50 *mm* length was made. The depth was further divided into two segments representing skin (2 *mm* top) and fat (5 *mm* bottom) shown in figure 4.4a. In the rectangular block representing fat, a diagonal cylindrical tube (diameter 1 *mm*) representing the blood vessel was built at a depth of 3 *mm* from the surface containing the electrodes. In the cylindrical tube, a wall was added with a thickness of 0.2 *mm* acting as the walls of the blood vessel, the inner cylinder created by adding the wall represented the blood in the vessel. On the top surface of the layer representing skin, an array of 16×16 circular electrodes was built with a 0.6 *mm* diameter, the electrodes were spaced with a 1 *mm* distance between the centres of each adjacent electrode as shown in

figure 4.4b. The array was positioned so that it sits in the centre of the $50\text{ mm} \times 30\text{ mm}$ surface of the skin layer.

The conductivity and relative permittivity for each layer were set to make the model behaved similar actual tissue. These values were found in [85] and were set to the values of; wet skin for the skin layer, average fat for the fat layer, muscle for the blood vessel layer and blood for blood layer. The electrode array was labelled by assigning; numbers (1 – 16) to the rows and alphabets ($a - p$) to the columns. In order to simplify the comparison between the different variations of depth and thickness. The impedance obtained from electrodes in columns g , h , i and j , where electrodes in the g and j columns were used as the CC pair and those in columns h and i were used as the PU pairs. Resulting in a total of 16 impedance values for each parameter variation.

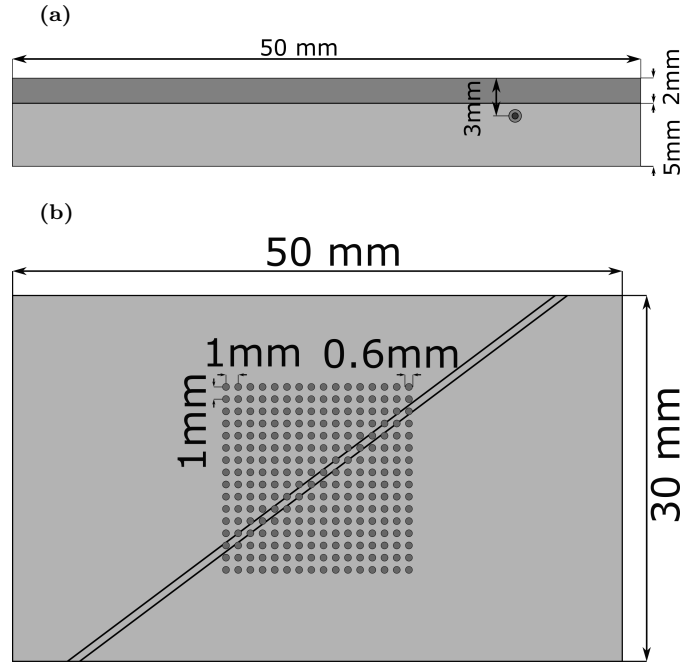


Figure 4.4: Model B setup. a) shows the side view of the model highlighting the location of the vessel along with the dimensions of the model and b) shows the top view of model length and width of the model along with the position of the electrodes

4.4.2 Detection of Vessels at Different Depths

To find the maximum depth at which a blood vessel could be detected, simulations were carried out where impedance values were obtained as previously described. In the simulation, impedance scans were carried out with a 1 *mm* diameter blood vessel at three different depths. Figure 4.5 shows the relative position of the blood vessel with respect to the top layer of the skin where, the depth of the blood vessel from the top layer was denoted by 'a'. The values of 'a' were varied from 3 *mm* to 5 *mm* with a step of 1 *mm*, while all other parameters of the model were left unchanged. The location where the blood vessel was directly below the measuring pair of electrodes, the transfer impedance for that location was expected to be much lower. This was based on results of the previous scanning simulation.

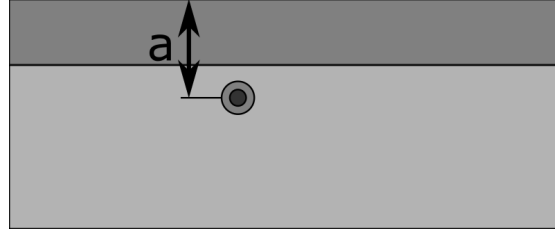


Figure 4.5: Model B: relative position of blood vessel from skin layer, where 'a' denotes the depth of the vessel from the surface of the skin layer

4.4.3 Detection of Vessel with Varying Vessel Thickness

While keeping the skin, fat and the electrode parameters similar to that of the previous simulation, the depth of the blood vessel was fixed at 3 *mm*. Impedance scans were taken while the diameter of the blood vessel were changed. The diameter of the blood vessel comprise of two parameters: the total diameter of the blood vessel 'b' and the wall thickness of the blood vessel 'c' as shown in fig 4.6. The total diameter of the blood vessel was changed from 1 *mm* to 0.4 *mm* with a step decrease of 0.2 *mm*, for every step decrease in the diameter the vessel wall thickness was reduced by 0.05 *mm* going from 0.2 *mm* to 0.05 *mm*.

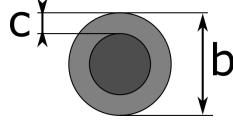


Figure 4.6: Model B: relative thickness of the blood vessel, where 'b' represents the diameter of the vessel and 'c' donates the wall thickness of the vessel.

4.4.4 Changing Electrode Size with Fixed Centre to Centre Spacing

The effect of changing the electrode size was explored in the following simulations. In this simulation, the depth of the blood vessel was fixed to 3 *mm* from the top layer of the skin with a vessel diameter set to 1 *mm* and vessel wall thickness of 0.2 *mm*. Without changing the skin and fat layers, impedance measurement sweeps were carried out. As shown in fig 4.7, the space between the centres of the electrodes was kept constant at 1 *mm*, while the diameter of the electrode 'd' was changed from 0.2 *mm* to 0.8 *mm* with a step of 0.2 *mm*.

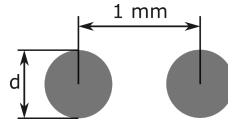


Figure 4.7: Model B: variation of electrode diameter 'd' with a 1 *mm* spacing between electrode centres

4.4.5 Changing Electrode Size with Fixed Edge To Edge Spacing

Keeping the vessel (depth, diameter and wall thickness) and other parameters the same as in the previous setup, the following simulation was performed. As in the previous simulation, the diameter 'd' of the electrodes was varied from 0.2 *mm* to 0.8 *mm* with a step of 0.2 *mm*. However, instead of having the centres of the electrodes fixed at a distance of 1 *mm*, the distance between the edges of the electrodes was fixed at 0.4 *mm*, as shown in fig 4.8. This was done to identify the minimum spacing that could be used in order to scan for a 1 *mm* diameter blood vessel at a depth of 3 *mm* from the top layer of the skin.

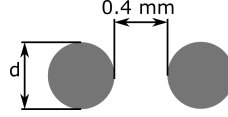


Figure 4.8: Model B: variation of electrode diameter 'd' with a 0.4 mm spacing between the electrode edges

4.4.6 Changing electrode spacing with fixed electrode size

The Spacing between the electrodes affects the depth of penetration of the electric field lines, and this affects the depth at which a structure can be detected. For this reason, the spacing between the electrodes was increased, going from 1 mm to 3 mm while keeping the electrode diameter constant, this was done by selecting every other electrode or by selecting every third electrode. For this simulation, the steps used in section 4.4.2 were used, where the depth of the blood vessel was varied. For each depth, impedance measurements were taken using the different electrode spacing. This set of simulations were carried out to identify which electrode configuration was able to obtain the maximum change.

4.4.7 Localised Measurements with Different Electrode Grouping and positioning

Grouping electrodes to take Localised measurements is also important, as shown in [103]. However, it is important to know how the different grouping and spacing of electrodes affects the measurements. For this set of simulations, All the parameters for the blood vessel and the skin and fat layers were kept the same as in the previous simulation. The electrode diameter was set to 0.6 mm with a spacing between the centres of the electrodes set to 1 mm. Starting from the conductivity of blood found in [85], the conductivity of blood was increased to 5 mS/m from its original by a step increase of 1 mS/m. In this simulation, three different groupings of electrodes were explored, going from using single electrodes, two electrodes diagonally grouped together, and four electrodes grouped together to emulate a single electrode of different sizes. The position of the injecting and measurement pairs of electrodes was also varied to identify the effect

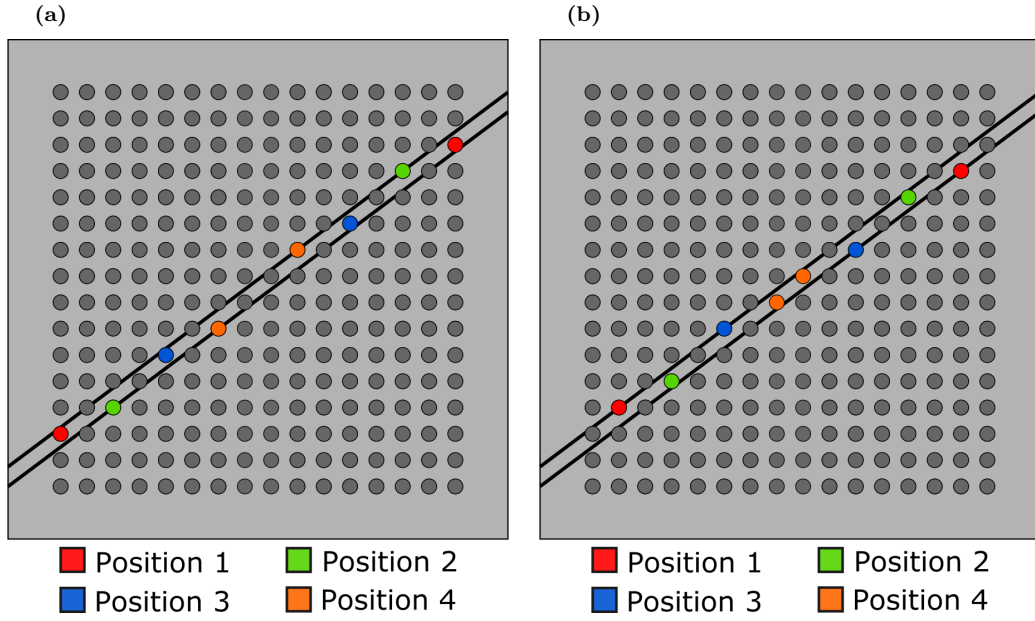


Figure 4.9: Model B: localised measurements taken using single electrodes. a) shows the Current injection(CC) electrodes position. b) shows the Voltage measurement (PU) electrodes positioning

of electrode position on its ability to detect any changes in blood conductivity.

- Figure 4.9 shows the first localised simulation setup, where fig 4.9a shows the Current injection (CC) electrodes and fig 4.9b shows the voltage measurement (PU) electrodes. Single electrodes positioned directly above the blood vessel were used in the simulation. The electrodes coloured in red show where the injection and measurement electrodes were positioned; being the furthest apart the electrode pairs could be assigned in the array. Using these red electrodes, impedance measurements were taken as the conductivity of blood was varied. This process was repeated for the other positions indicated by the green, blue and orange coloured electrodes. In this manner, measurements were taken for different spacing between electrode pairs.
- The second localised simulation, as shown in fig 4.10, uses two diagonally adjacent electrodes grouped as a single electrode to take measurements. Using the same procedure as in the previous simulation impedance measurements were taken from the three positions as indicated in fig 4.10a and fig 4.10b, which show the grouping

and spacing of the CC and PU electrodes.

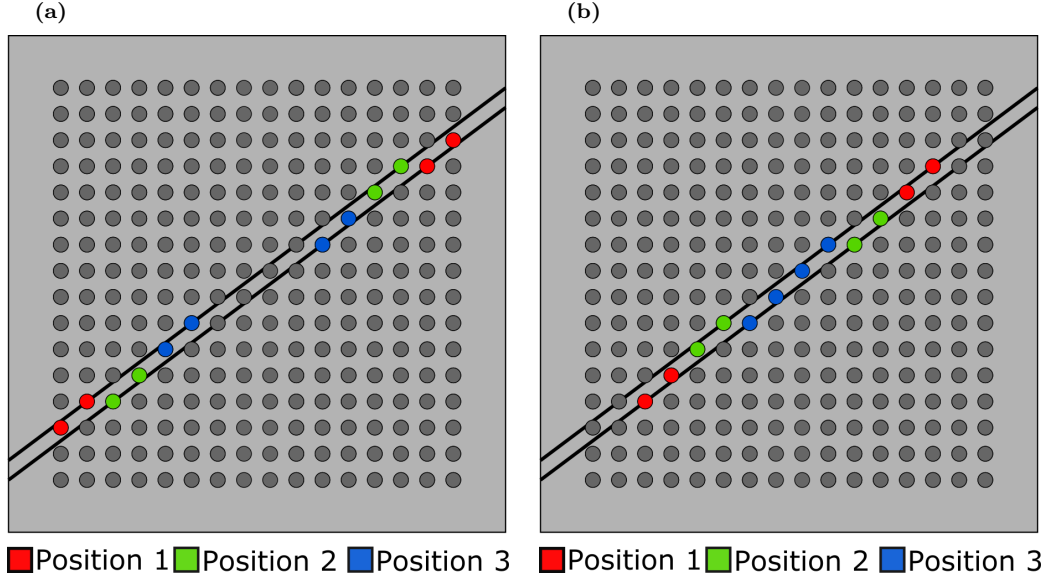


Figure 4.10: Model B: localised measurements taken using two electrodes diagonally grouped together. a) shows the Current injection(CC) electrodes position. b) shows the Voltage measurement (PU) electrodes positioning

- In the third localised simulation setup, four electrodes were then used to form a single electrode, as shown in fig 4.11. The electrode positions were varied, like the previous setups during measurements.

4.4.8 Results: Model B

Detection of Vessel at Different Depths

These simulations were carried out to identify the ability of the IREM to identify a blood vessel 1 *mm* in diameter with a wall thickness of 0.2 *mm* at depths of 3 *mm* to 5 *mm* from the top layer of the skin. Figure 4.12 shows the real part of the complex impedance from the different scans plotted against the 16 different electrode positions in the simulations. It can be seen in the results that as the position of the four electrodes goes from an area with no blood vessel, to an area where the blood vessel is directly below the electrode the impedance value decreases. This decrease in impedance was

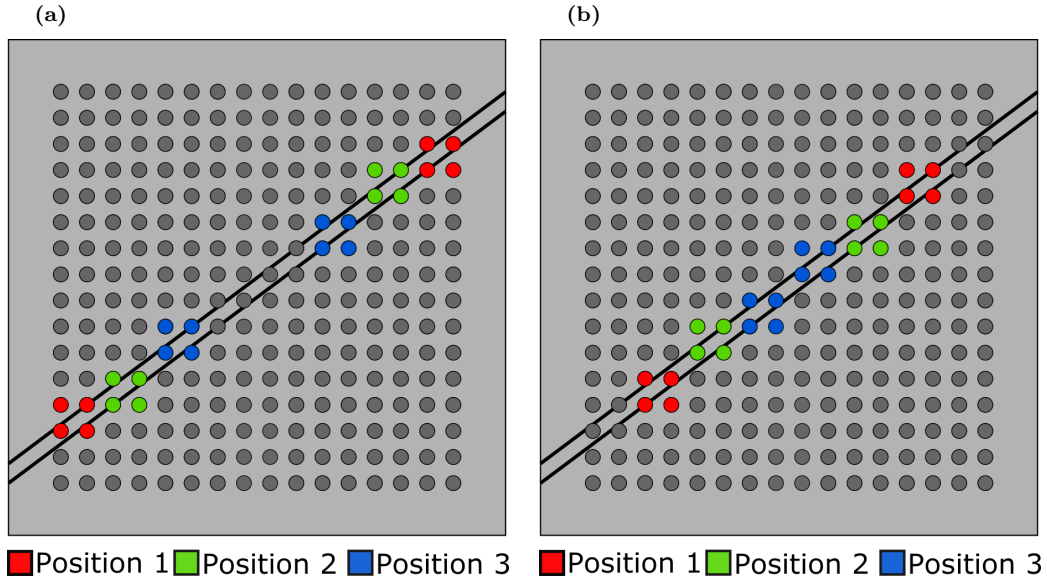


Figure 4.11: Model B: localised measurements taken using four electrodes grouped together. a) shows the Current injection(CC) electrodes position. b) shows the Voltage measurement (PU) electrodes positioning

expected as the conductivity of blood is much higher than the surrounding tissue. At 3 mm vessel depth from the surface (blue), the simulation clearly shows a large change in impedance when the electrode pixels were directly over the blood vessel. At the vessel depth of 4 mm (red), the change in impedance is not as prominent and even less so at a vessel depth of 5 mm (yellow). This indicates that at a spacing of 1 mm between the centres of the electrodes, the scan can detect a blood vessel up to a depth of 4 mm from the surface. To detect vessels at a deeper depth, the electrodes used to scan must be changed such that the spacing between the electrode pairs is greater, thus increasing the depth at which the electric field penetrates into to tissue.

Changing Blood Vessel Dimensions with Fixed Electrode Shape and Spacing

Figure 4.13 shows the results from the scan carried out as the dimensions of the blood vessel were reduced, from a diameter of 1 mm down to a diameter of 0.4 mm and the wall thickness reduced from 0.2 mm to 0.05 mm at a fixed depth of 3 mm . The real part of the complex impedance, measured in ohms, is plotted against the different locations

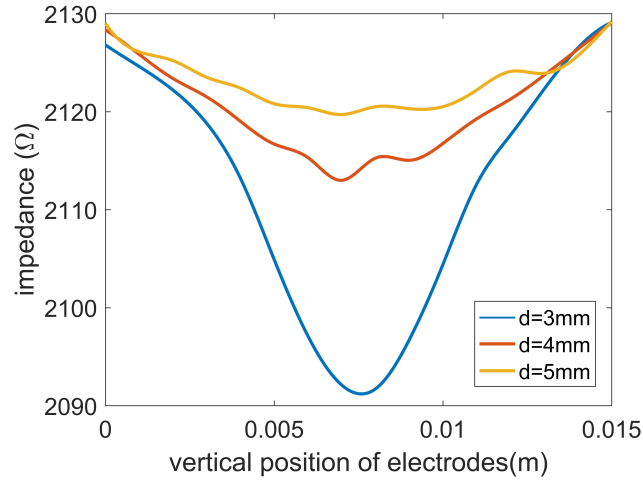


Figure 4.12: Model B: vessel detection at different depths. Detection of blood vessel at three different depths with an electrode spacing of 1 mm

of the electrodes. From the fig 4.13 it can be seen that for a diameter of 1 mm and wall thickness 0.2 mm (blue) the SPVT scan can accurately detect the vessel as it shows the greatest change in impedance when the vessel was below the electrodes. As the vessel diameter and wall thickness are reduced, the ability of the SPVT scan to detect the blood vessel also decreases. Through this simulation, it was observed that with the IREM setup, the smallest detectable vessel would have to have a diameter of 0.6 mm as the change in impedance is still distinguishable.

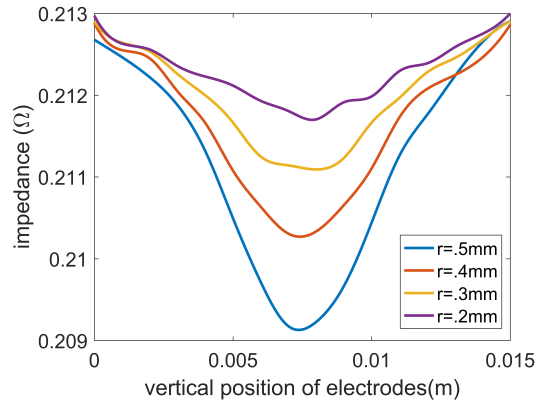


Figure 4.13: Model B: impedance measurements for different vessel diameters at a fixed depth of 3 mm

Changing Electrode Size with Fixed Centre to Centre Spacing

If the size of the electrode is varied while the spacing between the electrodes is kept constant, measured impedance should not be affected. Figure 4.14a is the graphical representation of the results of the different scans described in section 4.4.4. Here the real part of the complex impedance is plotted against the 16 different electrode positions of the sweep. Based on the results, it can be seen that as the size of the electrodes is varied from a diameter of 0.2 mm to 0.8 mm, the baseline value of the measured impedance increases. However, If the results of each scan were normalised, the overall change in measured impedance could be compared (fig 4.14b). It can be seen that the change in impedance for each scan show similar variations. From these results, it was conclude that even though the baseline impedance of the measurements may increase, but the sensitivity of the system remains the same.

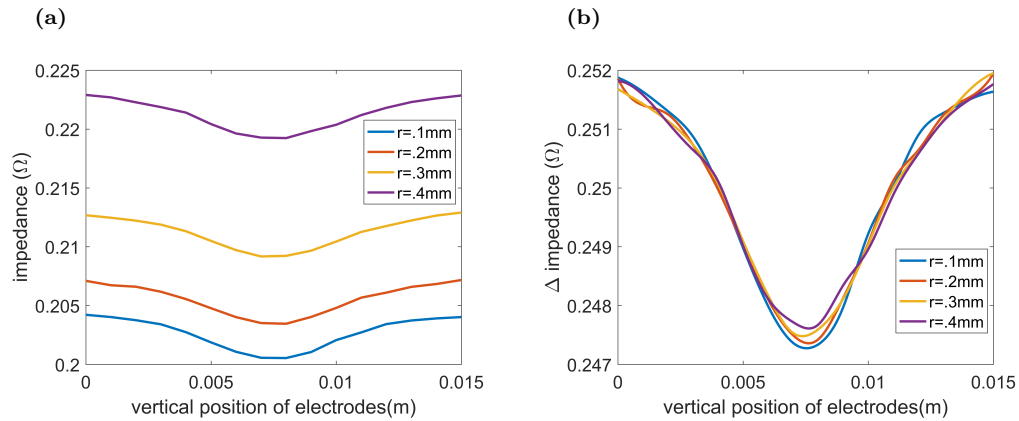


Figure 4.14: Model B: changing electrode size with a fixed centre to centre spacing. a) is the original measurement, b) is the normalised measurement

Changing Electrode Size with Fixed Edge To Edge Spacing

The purpose of this simulation was to achieve the smallest centre to centre spacing possible. For this reason, it was decided to keep the edge to edge spacing of the electrodes fixed at 0.4 mm, this allowed the centre to centre spacing of the electrodes to change as their sizes were varied from 0.1 mm to 0.4 mm as described in section 4.4.5. The results

from the simulation are shown in fig 4.15a; here the measured impedance is plotted against the position of the electrodes in the scan. Unlike the previous simulation results, it can be seen that here as the size of the electrodes was increased, the baseline value of the measured impedance decreases. As the baseline values of the different scans have a large range, the exact change in impedance cannot be visualised. Hence, the results of each scan needed to be normalised in order to compare the results of the different scans shown in fig 4.15b. The normalised results clearly indicate that as the centre to centre spacing of the electrodes increases the effect of the blood vessel on the impedance value also becomes more prominent. With the help of this simulation, the minimum spacing of the electrodes needed to detect a blood vessel of diameter 1 mm at a depth of 3 mm from the surface was identified as 0.8 mm. Therefore any spacing larger than 0.8 mm could be used to detect a blood vessel of the dimensions used in this simulation.

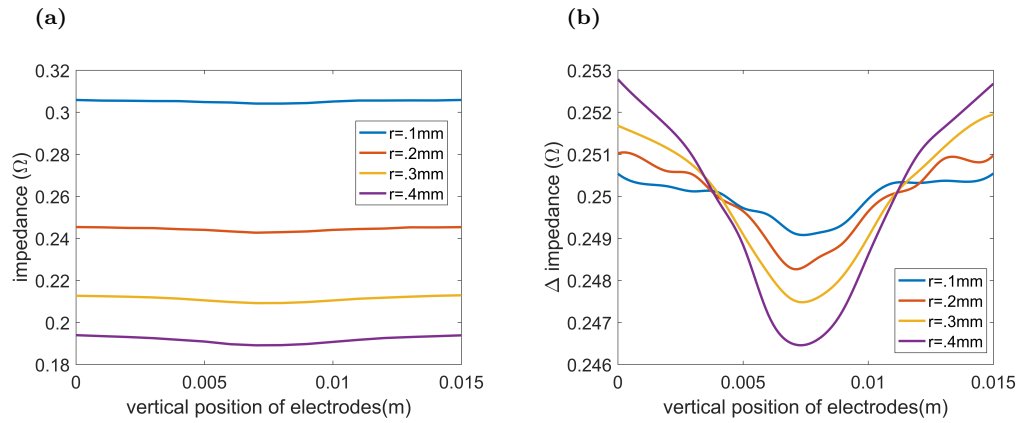


Figure 4.15: Model B: changing electrode size with fixed edge to edge spacing, in order to monitor its effect on measured impedance. a) is the original measurement, b) is the normalised measurement

Changing electrode spacing with fixed electrode size

The spacing between the electrodes is an important factor as it affects how deep the electric field lines penetrate into the tissue. For this purpose, the spacing between the electrodes were altered as described in section 4.4.6. Figure 4.16a shows the impedance scan with the spacing of 2 mm between the electrodes at three different vessel depths and fig 4.16b shows the same scan carried out with a spacing of 3 mm between electrodes. It

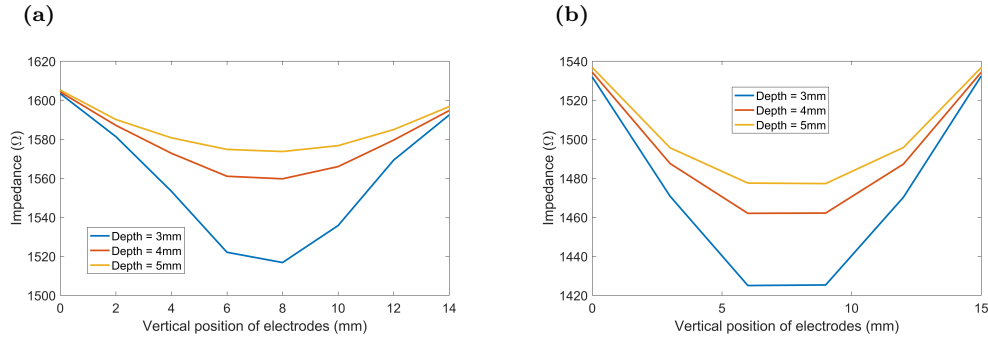


Figure 4.16: Model B: changing electrode spacing with fixed electrode size, to monitor its effect on measured impedance. a) is the 2 mm spacing between electrodes, b) is the 3 mm spacing between the electrodes

was observed from these scans that as the spacing between the electrodes is increased the change in impedance due to the blood vessel at a greater depth becomes more prominent. This confirmed that with a greater spacing, the depth at which the blood vessel could be detected increased as well. From this it was concluded to increase the electrode spacing to 2 mm with an electrode diameter of 1 mm, to increase the detection depth.

Localised Measurements with Different Electrode spacing between electrode pairs

From the previous simulations, it was clear that the distance between the electrode pairs affects the depth of electric field line penetration. Therefore, it was important to identify the effect of different spacing between electrode pares when taking localised impedance measurements. Figure 4.17 shows the results from the simulation using four single electrode pixels for taking localised impedance measurements. An increase in conductivity of blood results in a decrease in impedance measured in the simulation. Changing the spacing between electrode-pairs going from position 1 to position 4 showed, that the magnitude of change in impedance varies depending on the spacing between electrode-pairs. The largest change in impedance was observed at position 1 as the volume of blood under the electrodes was the largest. As the spacing between the electrode-pairs was reduced, the volume of blood also decreases, as does the depth at which the electric field lines penetrate into the tissue.

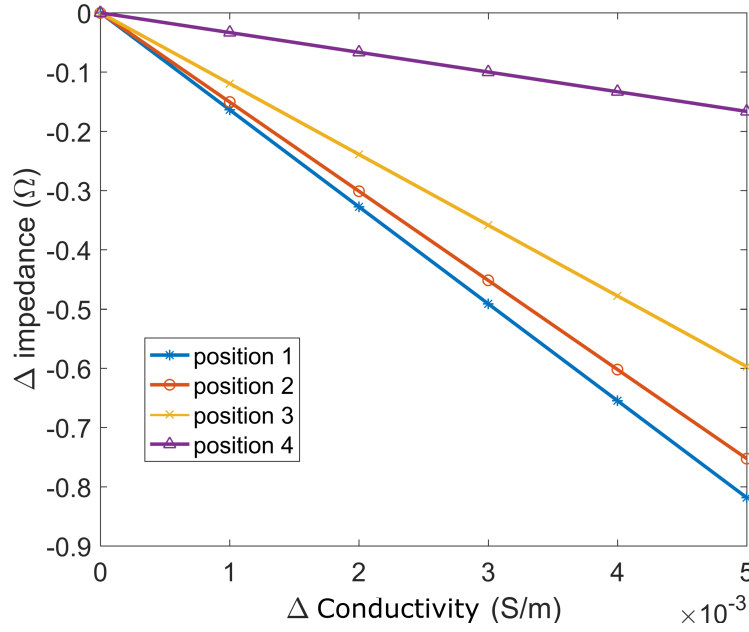


Figure 4.17: Model B: localised impedance measurements with single electrodes at different positions

Figure 4.18 shows results for diagonal grouping of electrodes following the above procedure. The simulation for the diagonally grouped localised electrodes only contains 3 positions: the maximum (position 1), the minimum (position 3) and the position in between (position 2). The results show that the maximum change in impedance is detected at position 1 with the maximum spacing, and as the grouped electrodes are brought closer together the magnitude change in impedance detected also decreases. Figure 4.19 shows the simulation results, for four electrode localised grouping. Similar to the diagonal grouping, this simulation also only has 3 positions. However, the results from this simulation showed that there was only a slight difference in the measured impedance of position 1 and 2 and their magnitude change in impedance. These simulations show that the change in conductivity of blood can be more accurately detected when the electrodes are positioned at the maximum distance possible (position 1) in the array. Therefore, for future electrode groupings the maximum possible electrode spacing will be used.

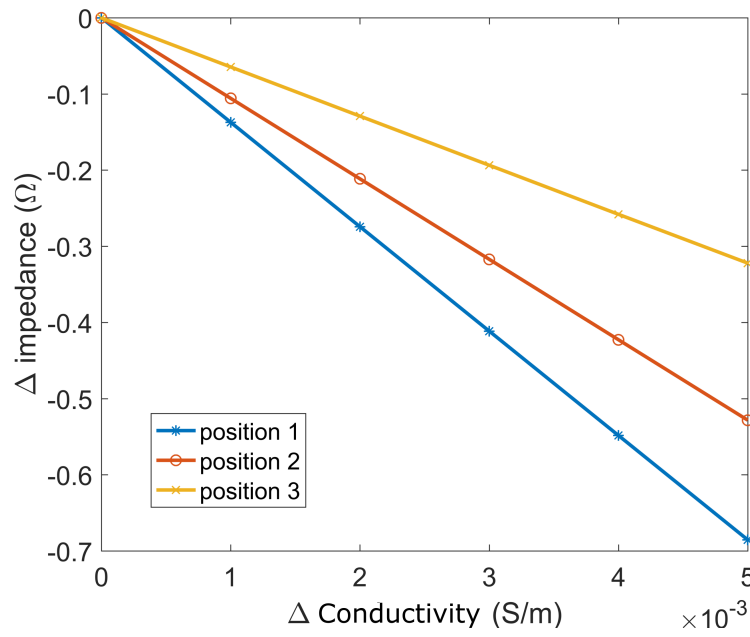


Figure 4.18: Model B: localised impedance measurements with diagonally grouped at different positions

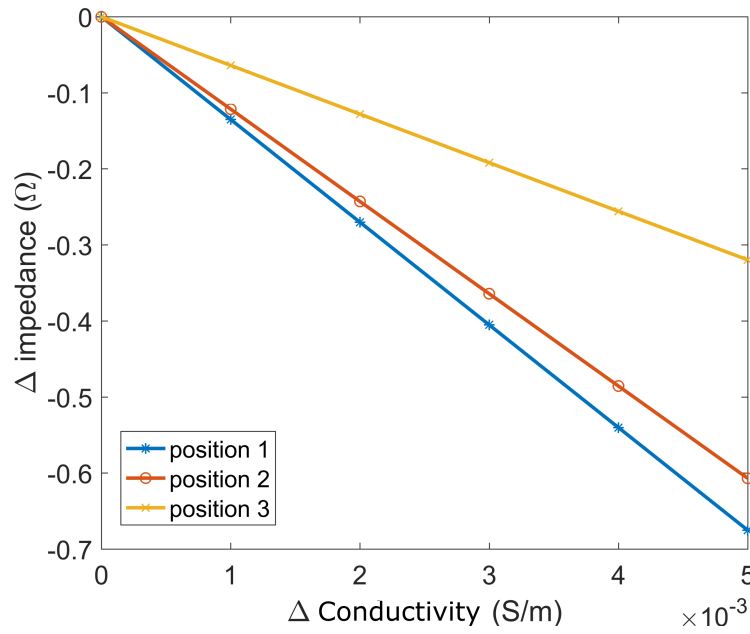


Figure 4.19: Model B: localised impedance measurements with four electrode groups at different positions

4.5 Stage 3: 2D Simulation

4.5.1 2D Model Setup

2D simulations were used to explore the relation of electrode orientation and spacing (between the measurement electrodes), on the ability to detect vessels of different depths and diameter. The Electrodes used in the 2D simulations were set to be 1 mm wide, with a centre to centre spacing of 2 mm between each adjacent electrode. This was done to increase the depth of detection and also to increase the electrode surface area. A total of eight electrodes were included in the design, labelled a to h as shown in figure 4.20. The simulation was split into two; in the first simulation the electrodes were perpendicular to the blood vessel (fig 4.20b), in the second simulation the electrodes were parallel to the blood vessel (fig 4.20a). In both simulations the centre four electrodes $c - d - e - f$ were selected as the tetrapole for taking measurement. The diameter of the vessel was varied starting from 1 mm then to 3 mm – 6 mm while the depth was kept constant at 5 mm. The electrode tetrapole were then switched to $b - c - f - g$ and then to $a - b - g - h$ while the diameter was varied. These tetrapoles were then used again while the diameter of the vessel was set to 5 mm, the depth was varied from 5 mm – 7 mm and then from 10 mm – 40 mm with a step change of 5 mm.

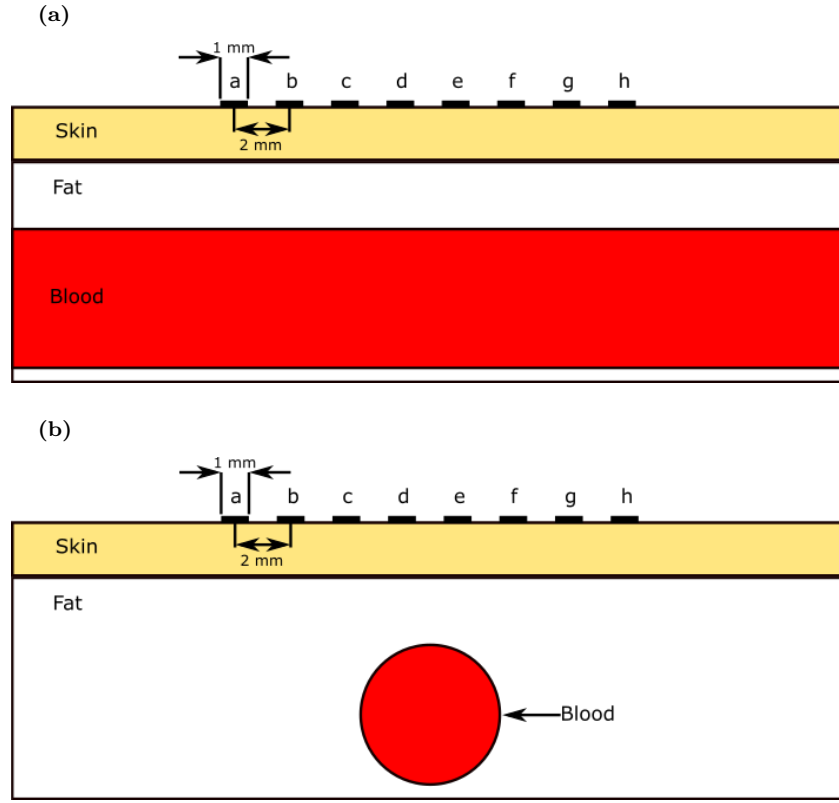


Figure 4.20: 2D simulation model. a) shows the model used for the parallel configuration of the 2D model. b) shows the model used for the perpendicular configuration of the 2D model.

4.5.2 2D simulation results

The results from the 2D simulation where the blood vessel was positioned parallel to the electrodes, while the depth and diameter of the blood vessel were varied is shown in fig 4.21. It shows that as the diameter of the blood vessel increases the impedance value obtained decreased due to the increase in the volume of blood. However, as the blood vessel moves to a deeper depth, its influence on measured impedance decreases. For an electrode spacing of 2 mm (i.e. electrodes $c - d - e - f$), after the depth of 10 mm, the influence of the blood vessel becomes negligible for all the different vessel diameters used here. As the spacing between the measurement electrodes was increased to 6 mm (i.e. electrodes $b - c - f - g$), the changes in the blood vessel diameter were detected up to the depth of 15 mm. With a spacing of 10 mm (i.e. electrodes $a - b - g - h$), the

detection depth was increased to approximately 20 *mm*, even-though the rate of change detected is much smaller at this depth.

For the 2D simulation where the blood vessel was positioned perpendicular to the electrodes (fig4.22), it was observed that in this orientation, a blood vessel of diameter of 1 *mm* had a minimum influence on the overall impedance. Blood vessels with a diameter greater than 3 *mm* produced a more prominent change in impedance at different depths. It was also observed that the depth of detection for this orientation was shallower than the parallel orientation. At a spacing of 2 *mm*, the maximum depth of detection observed was 7 *mm*, at 6 *mm* spacing it was 10 *mm*, and at 10 *mm* spacing it was 15 *mm*. The reduction in the depth of detection was due to, the total area of the blood vessel under the electrodes. In the parallel orientation, the blood vessel is under all the electrodes. Whereas in the perpendicular orientation, only the cross-sectional area of the blood vessel is part of the measurement, hence its influence on the impedance is much smaller. These results shows that depending on the orientation of the blood vessel with respect to the tetrapole orientation, the results obtained from the impedance measurement will vary. This shows that the SPVT scan implemented on model A will not be sufficient, and will require a slightly more complex scan. Therefore, the scanning sequence was altered to incorporate different tetrapole orientations, thus increasing the complexity of result analysis.

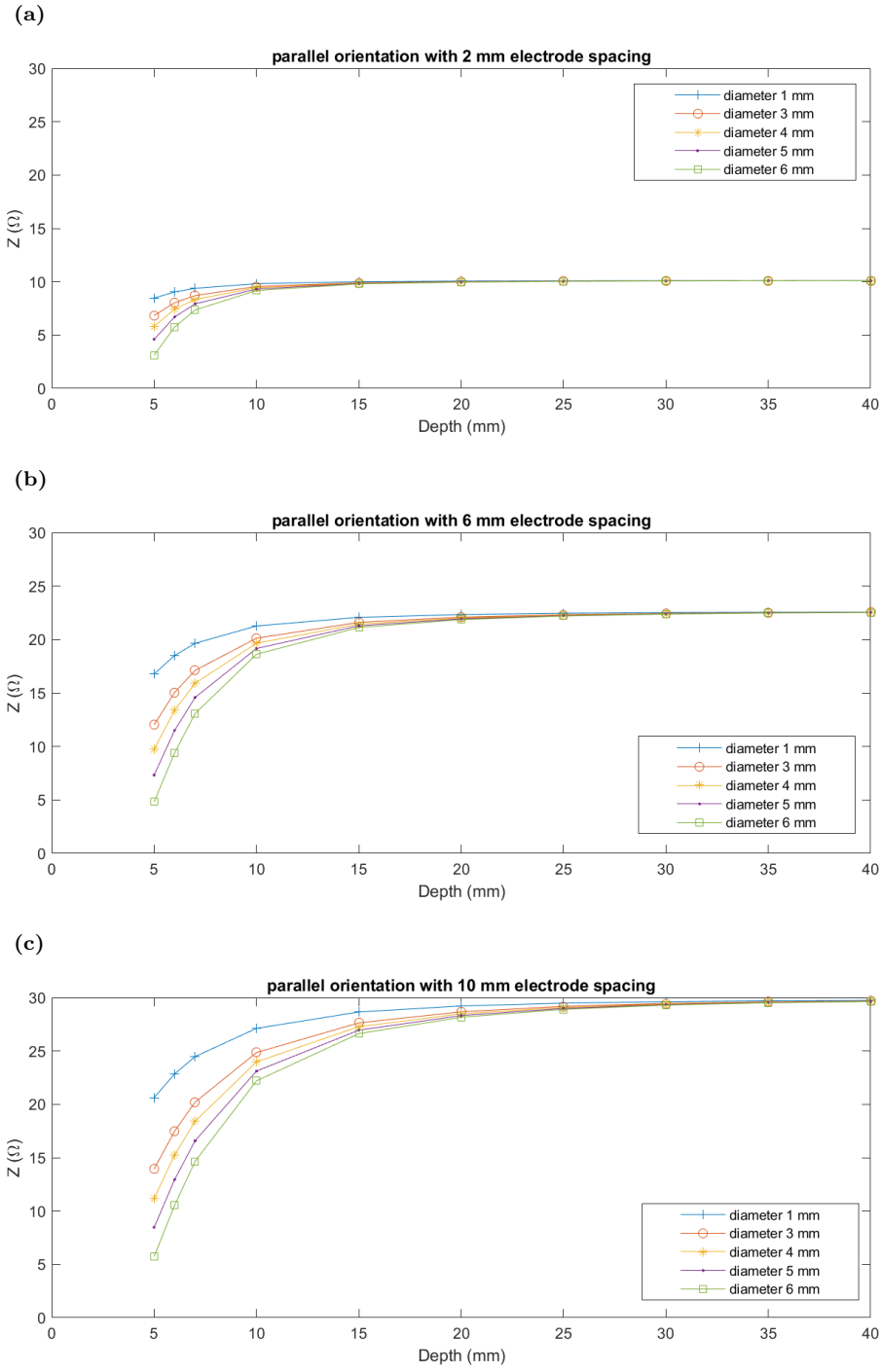


Figure 4.21: 2D Simulation parallel electrode configuration results. a) shows the results for 2 mm electrode spacing between PU electrodes, b) shows the results for 6 mm electrode spacing between PU electrodes, c) shows the results for 10 mm electrode spacing between PU electrodes.

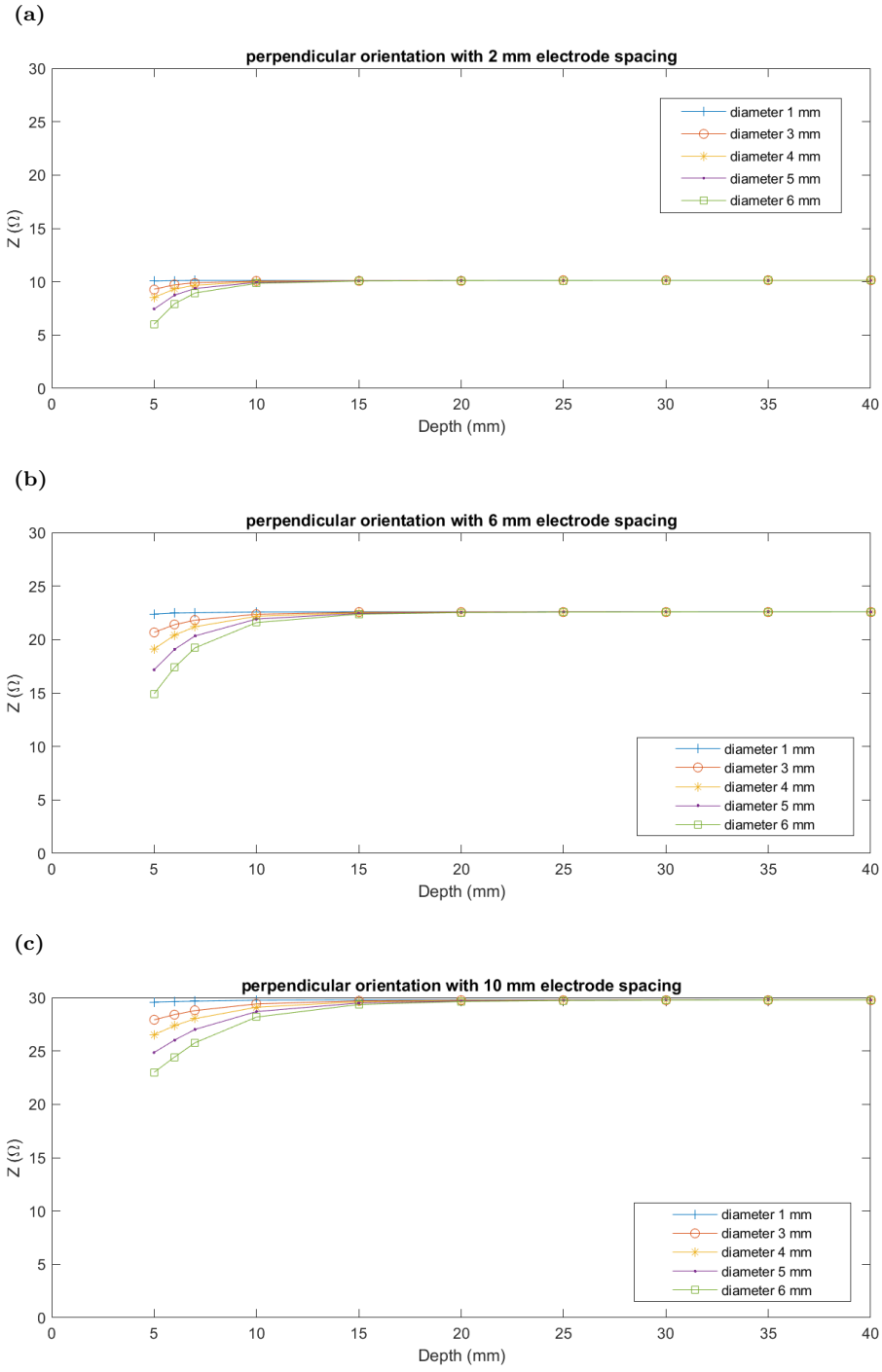


Figure 4.22: 2D Simulation perpendicular electrode configuration results. a) shows the results for 2 mm electrode spacing between PU electrodes, b) shows the results for 6 mm electrode spacing between PU electrodes, c) shows the results for 10 mm electrode spacing between PU electrodes.

4.6 Stage 4: Main Model Setup

Once the electrode parameters were identified, a standard model was made comprising of three different layers; the skin layer, the fat layer and the blood vessel. A length of 30 *mm* and a width of 50 *mm* was set for both the skin and fat layer (fig 4.23a), with a depth of 2 *mm* for the skin layer and 8 *mm* for the fat layer. In the layer of fat, a cylindrical structure with an initial diameter of 3*mm* was made to represent the blood vessel. The blood vessel was positioned at a depth of 5 *mm* from the surface (fig 4.23b), with an angular orientation θ of 37° . This angle was chosen to show that the system can be used irrespective of the orientation of the electrodes to the vessel. On the outer boundary of the skin, an array of 8×16 electrodes was made. In this array, each electrode was a circular boundary of 1 *mm* in diameter with a 2 *mm* spacing between the centres of each adjacent electrode. The circular boundaries act as the entry points for the current and do not represent actual electrodes. The conductivity and relative permittivity of wet skin was assigned to the skin layer, average fat assigned to the fat layer and blood assigned to the blood vessel [85]. Additional simulations with varying depth and diameter of the blood vessel were also carried out.

Similarly simulations with different orientation of the blood vessel were also implemented; this was done to identify how accurately the scanning sequence identified the orientation of the blood vessel with respect to the electrode array. To test the detection ability of the scanning sequence, the straight blood vessel was replaced with a bifurcation embedded in the fat layer at a depth of 7 *mm* from the electrodes. The angle of the bifurcation branches was kept at 75° from each other, as a worse-case scenario.

4.6.1 Single Pixel Variable Tetrapole (SPVT) Scanning Sequence

The SPVT scanning sequence was categorised into four types, which were labelled according to the direction they were carried out. To better explain the selection of the CC and PU electrodes for the different scans, the electrodes were labelled starting from the top left electrode. As can be seen in fig 4.24, the rows are assigned numbered 1 – 8, and the columns are assigned alphabets *a* – *p*.

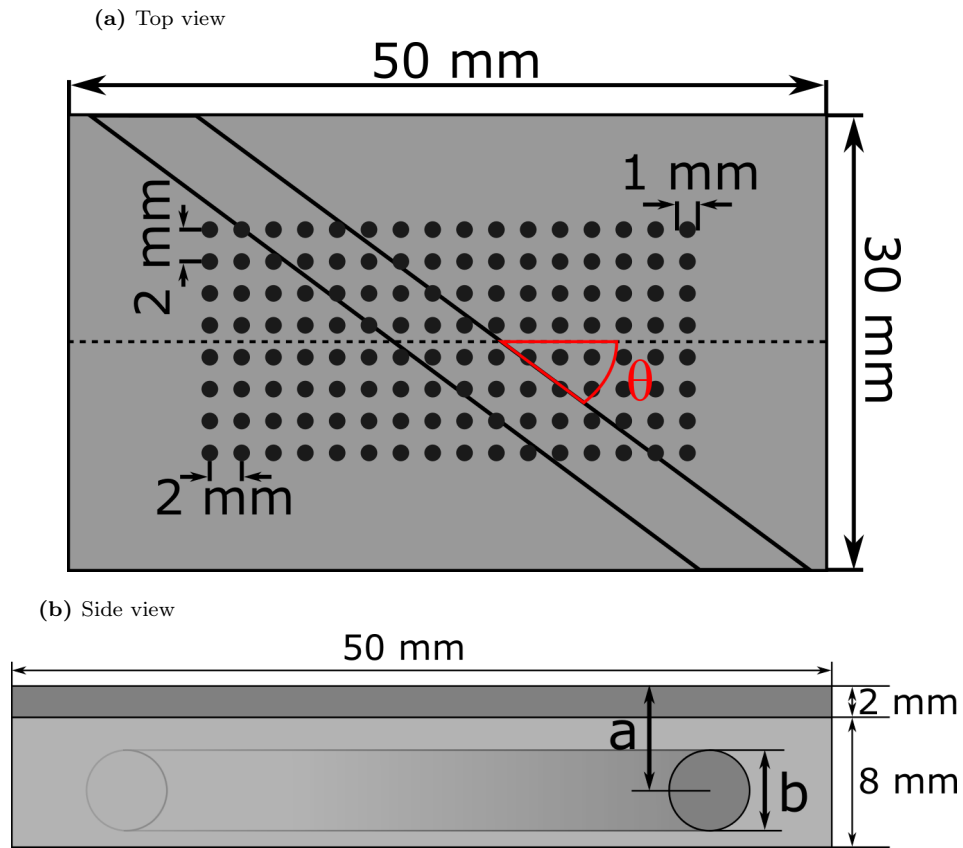


Figure 4.23: Main model setup. a) shows the top view of the 3D model, b) shows the side view of the 3D model, where the depth is denoted by 'a' and vessel diameter is designated by 'b'

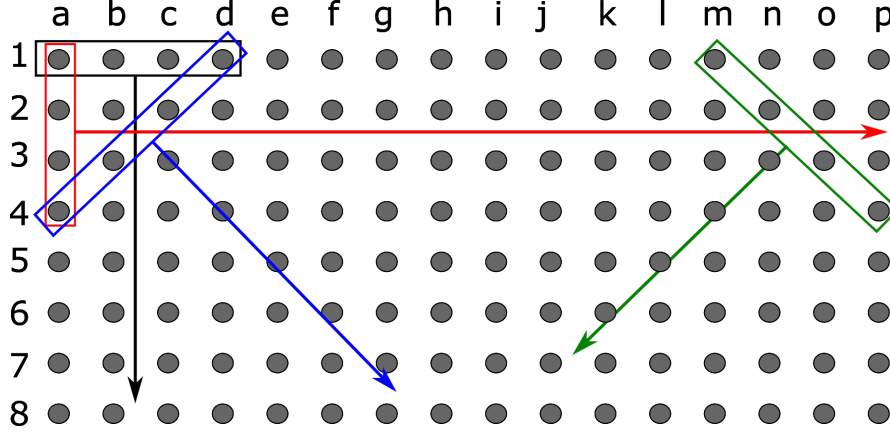


Figure 4.24: Single pixel variable tetrapole scanning sequence. The rows of electrodes are referenced using numbers '1-8'; the electrode columns are referenced using alphabets 'a-p'. Electrode orientation and direction of next electrodes for the: vertical scan is shown with a black arrow, the horizontal scan is shown with a red arrow, the diagonal right scan is shown with a green arrow, and the diagonal left scan is shown with a blue arrow.

Vertical Scan

For the vertical scan, four vertically adjacent electrodes $a1, b1, c1, d1$ were selected, $a1$ and $d1$ were used as the CC electrode pairs while $b1$ and $c1$ were used as PU electrode pairs. Once the transfer impedance of this set of electrode tetrapole was calculated, the electrode tetrapole was switched to the next row ($a2, b2, c2, d2$). In this manner, transfer impedance was calculated for all the possible combinations of electrode tetrapoles of the same orientation in the array. The orientation of electrodes and the direction of the next pair are shown with a black arrow in figure 4.24

Horizontal Scan

For the horizontal scan $a1, a2, a3$ and $a4$ were used as the starting position of the scan. In this orientation $a1$ and $a4$ were used as the CC electrode pairs and $a2$ and $a3$ as PU electrode pairs. The next position was $b1, b2, b3$ and $b4$, in this manner and orientation, the scan continued until all possible electrode combinations were used to calculate the transfer impedance. The orientation of electrodes and the direction of the next pair are shown with a red arrow in figure 4.24

Diagonal Right Scan

Electrodes $a4, b3, c2$ and $d1$ were used as the starting point for this scanning configuration. The $a4$ and $b1$ were used as CC electrode pairs and $b3$ and $c2$ as PU electrode pairs. The next set of electrodes used in this scan was $b5, c4, d3$ and $e2$ with similar CC and PU assignments. As in the other scans, the transfer impedance was calculated for all possible combinations of electrodes in the array. The orientation of electrodes and the direction of the next pair are shown with a blue in figure 4.24

Diagonal Left Scan

For this scan, the electrodes $m1, n2, o3$ and $p4$ were used as the starting point. As was done in the previous section, $m1$ and $n2$ were set as the CC electrode pairs and $o3$ and $p4$ were set as PU electrode pairs. The next set of electrodes used was $l2, m3, n4$ and $o5$, following this electrode orientation and assignment measurements were taken throughout the whole electrode array. The orientation of electrodes and the direction of the next pair are shown with a green arrow in figure 4.24

4.6.2 Image Analysis and Feature Recognition

The data obtained with the scanning system correspond to horizontal (0°), vertical (90°) and diagonal (45° and 135°) scanning directions. These result in arrays of size 8×13 for the vertical scan, 5×16 for the horizontal scan and 5×13 for each for the two diagonal scans, respectively. The impedance measurements include the (x, y) coordinates of the points on the surface of the volume. In order to reduce the effect of measurement noise, distance-based weighted averaging was performed, taking into account the effect of the scanning orientation. The Euclidean distance was used in the experiments, with the corresponding weights being proportional to 1 for the horizontal/vertical matrices, and $\sqrt{2}$ for the diagonal ones, respectively. The result of this process, which combines together the measurements from the four scanning directions, is an array of size 6×14 .

The image processing steps are as follows:

- a Thresholding is applied to separate the vessel from background tissues using Otsus

method [104]

- b The vessel boundaries are detected [105], followed by the application of thinning [106], using mathematical morphology operators. This results to single-pixel width vessel boundaries.
- c In order to detect the presence of bifurcations, skeletonization [106] is applied to the binary vessel region obtained in step a). The number of neighbours, N_{skel} , of the pixels belonging to the skeleton of the vessel is calculated and used to classify them as follows:

$$N_{skel} = \begin{cases} 1, & \text{pixel is an endpoint} \\ 2, & \text{pixel is part of the skeleton} \\ \text{otherwise,} & \text{pixel indicates the location of a bifurcation} \end{cases}$$

This produces a list of candidate bifurcation points, which could then be used to segment the object into main vessel and side branches.

- d Identification of the parts of the object which belong to the main vessel and side branches is performed by finding the intersection points of the normal vectors on either side of the bifurcation and end points belonging to the skeleton of the vessel, using the vessel boundaries detected in step b).
- e The width of each segment of the vessel object is determined by averaging the widths of the straight line segments, corresponding to the pixels on either side of the boundary. A calibration process is performed to convert Euclidean distances into physical units in mm.
- f The orientation of each segment of the vessel object is estimated by averaging the orientations of the left and right boundaries. Boundary orientation is determined by calculating the least squares estimates of the best fitting straight line to the boundary pixels.
- g The bifurcation angle is estimated by subtracting the orientations of the two vessel

branches, obtained in step f).

h To detect the presence and estimate the percentage of occlusion in a vessel, an occlusion-free vessel image model with the same geometric parameters is used. Specifically, the difference image between the vessel image with occlusion and the occlusion-free model is calculated. The difference image is thresholded using the method in step a), to identify the pixels associated with the region of the occlusion. We use a similar approach to that of step d) to identify the occlusion region in the vessel, i.e., detecting the start/end pixels of the occlusion along the vessel wall, thus segmenting the associated part of the vessel. Finally, the occlusion ratio is calculated as:

$$Occ(\%) = \frac{A_{occ}}{A_{total}} \cdot 100\%$$

where A_{occ} is the number of the pixels of the occlusion region, and A_{total} is the number of pixels belonging to the associated vessel area.

4.7 Simulation Procedure

4.7.1 Parameters Variations

The different parameters in the main model such as the vessel orientation, vessel diameter, vessel depth and occlusions were altered to analyse the capabilities of the novel scanning approach. The different parameters were altered as follows:

Vessel Orientation

While keeping the vessel diameter and depth fixed at 5 mm and 7 mm respectively and keeping the skin and fat layers constant, simulations were carried out for four additional models. The orientation of the vessel in the model was changed to 0°, 15°, 37° and 45° with respect to the longitudinal axis of symmetry of the electrode array. This was done in order to demonstrate the ability of the scanning sequence to identify the orientation of the vessel with respect to the position of the electrode array.

Vessel Diameter

Since the structure to be detected was the blood vessel, it was important to change the parameters of the blood vessel. Since the size of the carotid artery varies between 4.3 mm to 7.7 mm [107], It was decided to vary the size of the blood vessel to 3 mm , 4 mm , and 5 mm in the simulation model; this was done to identify the minimum thickness that could be detected using this setup and also to show how the different diameters would affect the impedance measurements. Figure 4.23b shows the side view of the 3D model, where ' b ' represents the diameter of the blood vessel. These values were chosen because they are very close to and below the minimum diameter of the artery.

Vessel Depth

The depth of a blood vessel varies from patient to patient; hence the depth of the blood vessel was varied to 5 mm , 6 mm and 7 mm . This will help demonstrate the ability of the scanning method to detect structures at different depths. In the side view of the 3D model shown in figure 4.23b, ' a ' represents the depth of the blood vessel.

4.7.2 Expanded Bifurcation Model

From the results of the bifurcation model, it was observed that the scanning resolution was insufficient to capture the whole bifurcation. Therefore, the dimensions of the simulation model were expanded, the length and width of the model were doubled to 100 mm and 60 mm , respectively keeping the depth consistent with the main model. The vessel diameter and angle of bifurcation were kept constant, to those of the main model, located at a depth of 7 mm positioned at the $x \times y$ centre of the model. The number of electrodes and the array orientation was changed from '128 electrode arranged in an 8×16 array' to '600 electrode arranged as a 20×30 array'. While the electrode size and inter-electrode spacing were kept constant at 1 mm and 2 mm , respectively. The model dimensions are shown in figure 4.25.

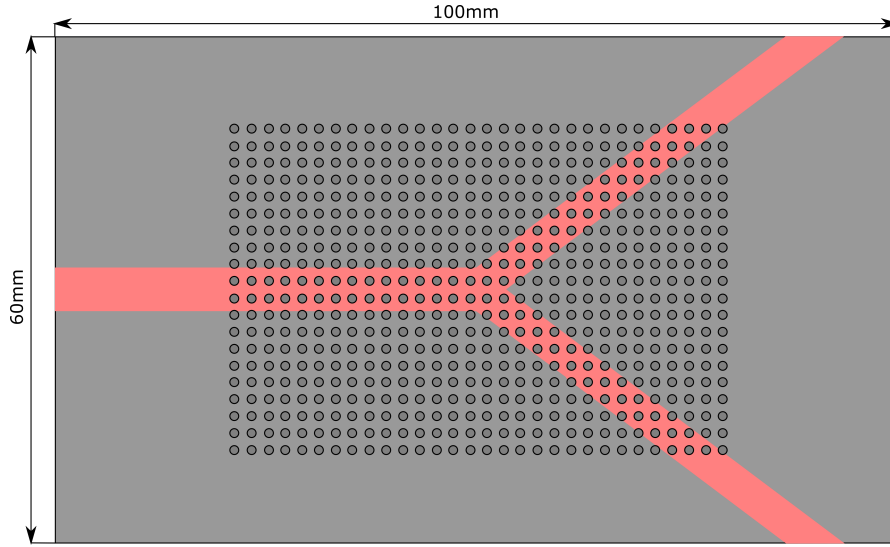


Figure 4.25: Expanded bifurcation model: 3D simulation model of bifurcation with increased dimensions with 20×30 electrode array.

4.7.3 Main Model: Identification of Vessel Orientation

To test the ability of the system to identify the correct orientation of the blood vessel with respect to the electrode geometry. The scans for the different vessel orientations were implemented in simulation only. Using the process described in section 4.6.2, where the four scans for one vessel orientation were combined to generate a new matrix. From this new matrix through thresholding, the vessel orientation was obtained. The actual vessel orientation angle and the angle measured from the impedance measurements are given in table 4.2. It was observed that for different vessel orientations, it is possible to detect them with an accuracy of $\pm 2^\circ$ for angles other than the orthogonal and 45° angles. This shows that the relative location and orientation of the blood vessels can be identified accurately.

Table 4.2: Orientation extracted with respect to the actual

| Actual angle | measured angle |
|--------------|----------------|
| 0° | 0° |
| -15° | -14° |
| -37° | -35° |
| -45° | -45° |
| 90° | 90° |

4.7.4 Main Model: Vessel Detection at different Depth

As the depth of the blood vessel varies from person to person, it is important to identify the capability of the scanning method proposed in this chapter. For this purpose, simulations were carried out where the depth of the blood vessel was varied. The resulting matrix from combining the four types of scans are shown in fig 4.26a, applying a threshold to the results in the indication of the general location of the blood vessel as shown in fig 4.26b. Applying this process to the results obtained from multiple simulations and experiments implemented with the blood vessel at different depths, resulted in the accurate detection of blood vessel location and orientation. Hence, indicating that this scanning method can be used to transcutaneously detect blood vessels at varying depths.

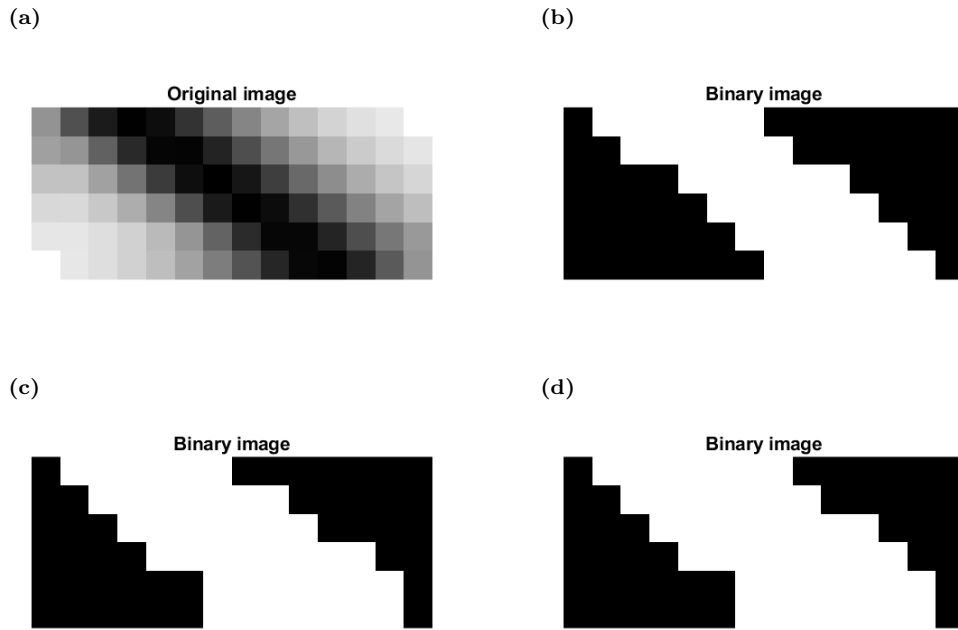


Figure 4.26: Main model: 3D simulation Vessel detection. a) shows the result from combining four scanning methods, b) shows the result of applying a threshold to 'a' highlighting the vessel boundary, c) shows the threshold result of a vessel at a depth of 6 *mm*, and d) shows the threshold result of a vessel at a depth of 7 *mm*.

4.7.5 Main Model: Feature Detection

Straight Line Vessel

In simulation the vessel diameter was varied. The scan results were processed and then threshold-ed similar to the previous simulation, highlighting the vessel location and orientation. Further to this, the vessel edge were extracted, resulting in fig 4.27. By measuring the euclidean distance between the two boundaries, the diameter of the vessel was calculated as shown in table 4.3. It was observed that due to the low resolution, the width of the blood vessel could not be measured accurately. Detection of vessel diameter still requires a more complex image processing technique, however, image processing is not looked at in great depth in this research.

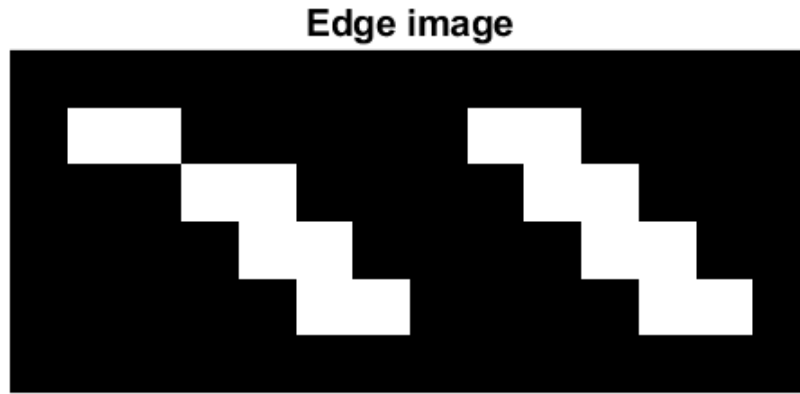


Figure 4.27: Main model: simulation vessel boundaries

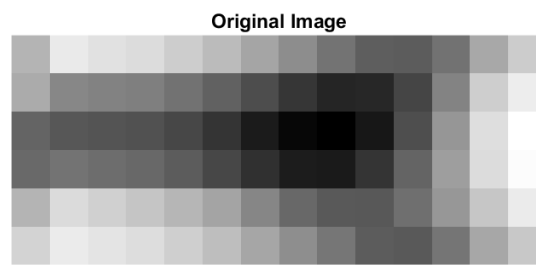
Table 4.3: Model B: vessel diameter actual vs measured

| Actual diameter | Measured diameter |
|-----------------|-------------------|
| 3 mm | 3.23 mm |
| 4 mm | 3.23 mm |
| 5 mm | 3.315 mm |

Bifurcated vessel

Using the process described in 4.6.2 resulted in the images shown in figure 4.28. Figure 4.28a shows the image obtained by combining the four types of scanning sequence. Figure 4.28b shows the result after thresholding the combined scan image, and fig 4.28c shows the outline extracted obtained after further processing. It was observed that the number and distribution of electrode pixels were insufficient to capture the whole bifurcation. Therefore, it was decided to increase the number of electrode pixels and arrange them in a 20×30 array configuration while leaving the electrode size and inter electrode spacing constant. To increase the number of electrode pixels, the dimensions of the model were also adjusted as described in section 4.7.2. Figure 4.29a shows the combined scan from the expanded array configuration, applying a threshold to it results in fig 4.29b and the outline obtained from it are shown in fig 4.29c. As can be seen, increasing the size of the electrode array results in better identification of the bifurcation. This shows that with a sufficient number of electrode pixels, features such as bifurcations and straight-line vessels can be identified using this scanning method.

(a)



(b)



(c)

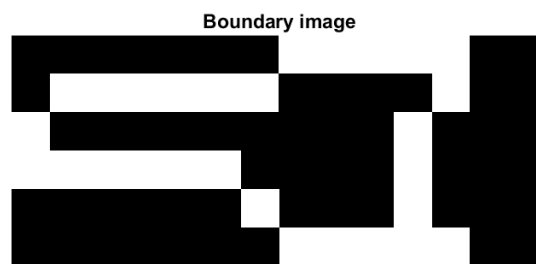
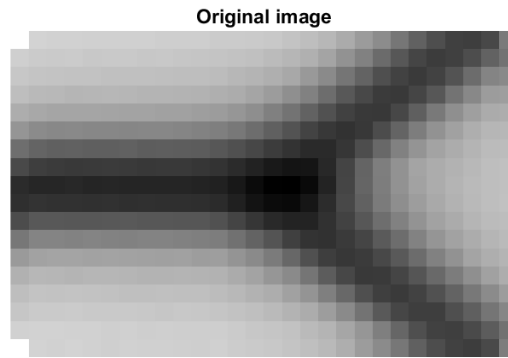
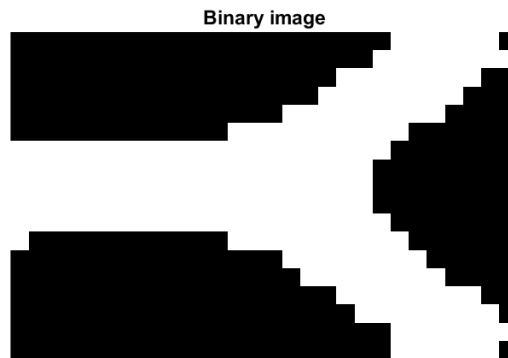


Figure 4.28: Main model: bifurcation vessel detection. a) shows the result from combining the four scans, b) shows the vessel after thresholding and c) shows the boundary of the vessel

(a)



(b)



(c)

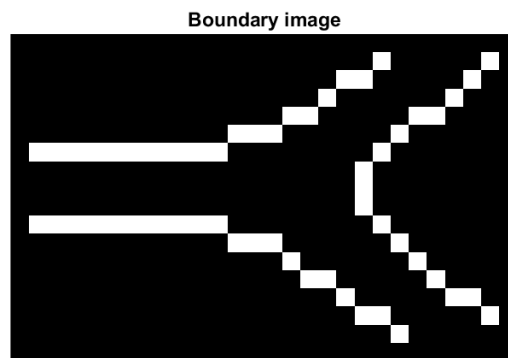


Figure 4.29: Expanded bifurcation model: expanded array bifurcation vessel detection. a) shows the result from combining the four scans, b) shows the vessel after thresholding and c) shows the boundary of the vessel

4.8 Discussion

Theoretically, impedance measurements are expected to be lower in an area where a blood vessel is present under the electrode tetrapole than in areas without a blood vessel. This theoretical concept was demonstrated by the simple scan implemented in stage 1. The conductivity variation simulations implemented using pseudo-stripe and localised electrode grouping in this stage reaffirmed the results obtained in chapter 3. In stage 2, it was observed that, an array of electrodes with an inter-electrode spacing of 1 *mm* could detect a blood vessel at a maximum depth of 4 *mm*. The smallest diameter blood vessel that could be detected with such an electrode array was 0.6 *mm*; here, changing the electrode size did not influence the depth of detection. However, changing the inter-electrode spacing did affect the depth of penetration of the electric field lines; these results follow what has been stated by other researchers [18]. For all localised electrode grouping used in this stage, it was observed that, using the maximum possible distance between the measurement electrodes gave the greatest impedance variations. The results obtained in stage 3 highlighted the influence of the electrode tetrapole orientation to that of the blood vessel. When the tetrapole was parallel to the blood vessel, there was a significant influence on measured impedance than when it is perpendicular to the blood vessel. The influence of the tetrapole orientation on the impedance measurement led to the development of the SPVT scanning sequence, which in turn inspired the idea of combining the different scans to create a single impedance map. In stage 4, the capabilities of the new SPVT scanning sequence and the accuracy of the features extracted from the impedance map were assessed. The orientation of the blood vessel could be extracted with a high level of accuracy from the impedance maps. Even though the diameter of the vessel was not calculated, due to low pixel resolution, it was still possible to detect the presence of a blood vessel at deeper depths. The feature recognition algorithm successfully detected the bifurcation; however, it was necessary to increase the number of electrodes in the array in order to accomplish this. The scanning and detection method developed with the help of the first three stages was assessed thoroughly, in simulation stage 4, for the majority of cases. The next logical step is to implement the

scanning and detection method experimentally. For experimental verification, custom circuitry and phantoms will need to be designed, which will be covered in the next chapter.

4.9 Conclusion

The aim of this chapter was to design and assess a new scanning method using electrode arrays to take impedance measurements. FEM simulation models were developed and used to investigate the effectiveness of the scanning method. The rationale of the simulations was to find the relative location and orientation of the blood vessel, to identify pixels in close proximity to the vessel, and to identify the presence of a bifurcation. In the simulations, single pixel variable tetrapole (SPVT) scans were implemented using different tetrapole orientations. The results obtained from the SPVT scans were then processed, and the vessel orientation, its relative location, pixels in the vicinity of the blood vessel, and confirmation of the presence of bifurcation were extracted. The results confirmed that in simulations, it was possible to extract blood vessel characteristics by using the proposed scanning method. The next stage in the assessment of the scanning method would be to validate it experimentally. Hence, the next chapter looks into designing and testing custom circuitry, which would then be used to replicate some simulation results along with additional flow studies.

Chapter 5

IREM Experimental verification and Flow Measurements

In the previous chapter, with the help of simulation, it was shown that SPVT scanning sequence could be used to detect vascular structures transcutaneously. It was also demonstrated that features such as the vessel orientation and bifurcations can be obtained from the scanning results. It was necessary to replicate the simulation experimentally to validate the results. For this purpose, a custom circuit has to be designed, that can be used to implement the SPVT scanning sequence while having a minimal influence on impedance measurements.

In this chapter, the design of a customised circuit (IREM) is described in detail. The IREM circuit will then be used to implement SPVT scans on phantoms mimicking the simulation model. The ability of IREM circuit to group electrodes to take localised measurements will also be tested using phantoms customised for flow studies. The software programs, data acquisition sequence, experimental procedure used to test the IREM circuit along with the construction of the phantom will also be described in detail.

5.1 Method

To verify the simulations, a PCB with an electrode array matching those used in the main model of chapter 4 was designed. The maximum number of electrodes that could be accommodated into the PCB was an array of 8×16 electrodes. Each electrode in the array had a diameter of 1 mm and an inter-electrode spacing of 2 mm between centres. These dimensions were limited due to the limitation of the PCB track and component placement. Once the PCB was designed and assembled, experiments were carried out using anatomical phantoms with matching dimensions to those of the main model of chapter 4. The experiments were carried out using four types of scans, on phantoms with different diameter blood vessels at different depths; this was done to verify the simulation through experiments.

After the scanning capabilities were verified through experiments, a new phantom was designed, which comprised of a conductive tube representing an artery. The new phantom was designed for taking impedance plethysmographic measurements continuously for over 60 seconds using localised electrode grouping. Experiments were also carried out while varying the flow parameters of the pump. The SV and BPM values were varied, where the SV was varied from 50 cc to 70 cc and the BPM from 20 BPM to 40 BPM . These parameter variation experiments were implemented for two main reasons; one was to monitor the influence of these parameters on the impedance measurements. The other reason was due to the fixed sampling rate of the measurement device. In order to increase the number of samples measured during one cycle of the pump, reducing the BPM was proposed.

5.2 IREM Block Diagram

To design an array of electrodes which allows SPVT scanning and also grouping electrodes to form electrodes of larger effective area, a block diagram was designed (figure 5.1). The design included a PC block, which sends electrode assignments and grouping signals to the switching control block as well as the trigger signal to the impedance

analyser to take impedance measurements. The switching control block interprets the signal from the PC block and sends the desired signal to the analogue switching array. The analogue switching array contains the switches which interface between the impedance analyser and the electrode array. Depending on the signals received from the switching control block, the analogue switching array connects the desired electrodes to their respective channels of the impedance analyser. The analogue switching array is supposed to allow the freedom of connecting any electrode to one or more channels of the impedance analyser or none of the channels. This will allow the measurement topology as well as scanning and grouping of the electrodes to be freely altered as desired.

5.3 IREM Circuit Design

The main concept for this design is to make it possible to connect any electrode pixel to any or none of the four channels, to facilitate multiple pixels to be connected to the same channel increasing the effective area of the active electrode. Unlike the DRE setup described in chapter 3, where each electrode site (A, B, C and D) connect to a single impedance channel. The flexibility of the IREM design requires each electrode pixel to be connected to all the four impedance channels. Therefore, the connection of electrode pixels to the ADG714 switch was altered (fig 5.2, A.5, A.6 and A.4). Since the ADG714 has eight SPST switches, connecting four channels of the impedance analyser (I1, V1, V2 and I2) to four switches while connecting the other ends of the switches to a single electrode pixel. This allows two electrode pixels to be connected to a single IC, making the total number of ADG714 ICs needed to be half the total number of pixels. In the case of the IREM, there were 128 electrode pixels used; therefore 64 ADG714 ICs were needed to be used to ensure all pixels could be connected to any of the four channels.

To address all the 64 ICs and reconfigure the switches in them, the use of a micro-controller is important. As the number of input/output (IO) pins on a micro-controller are limited, while each switch IC needs one IO pin dedicated to it. Three approaches can be used to address this connection problem. The first is to use a micro-controller with a large number of IO pins; however this increases the complexity of the PCB

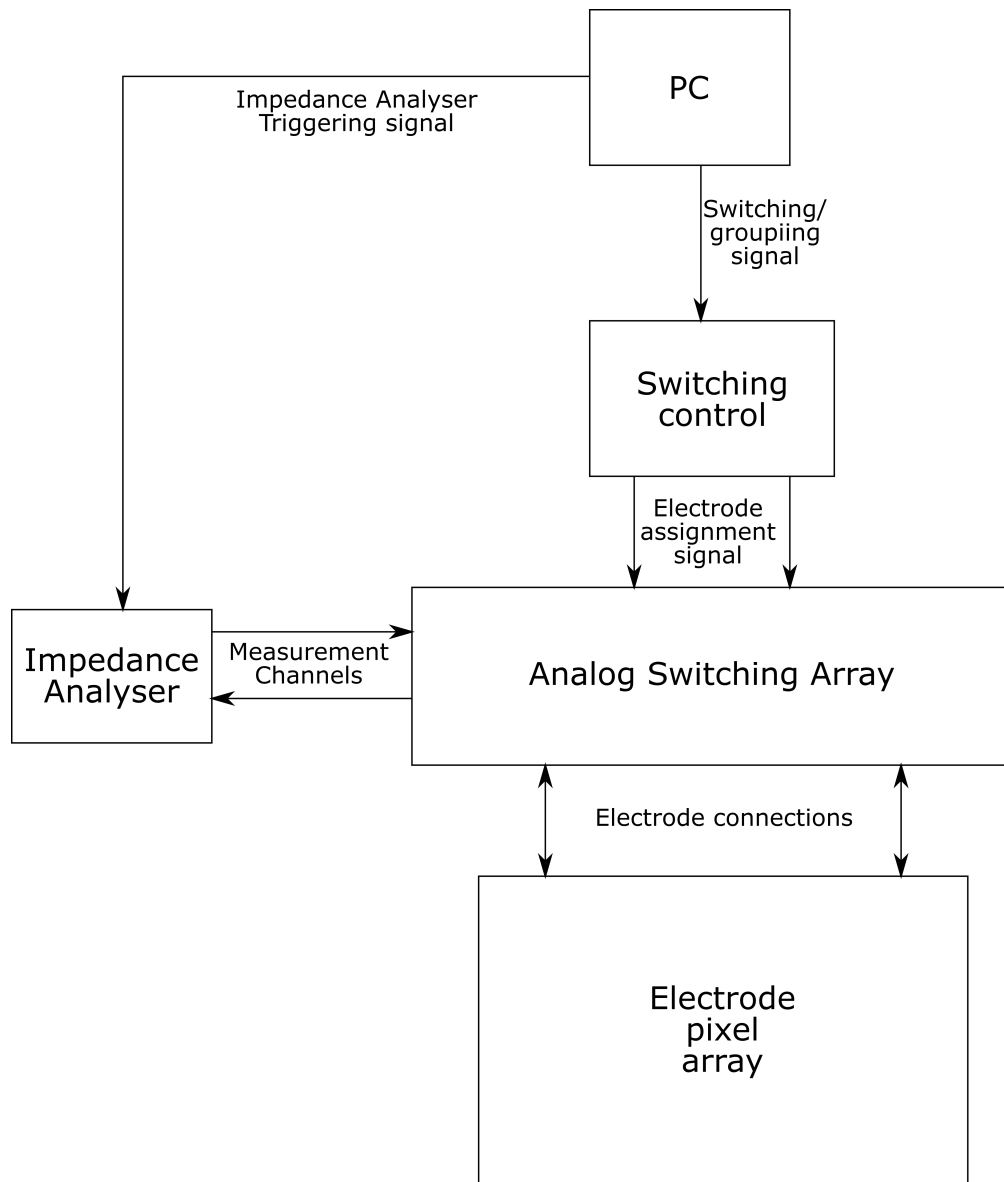


Figure 5.1: IREM block diagram

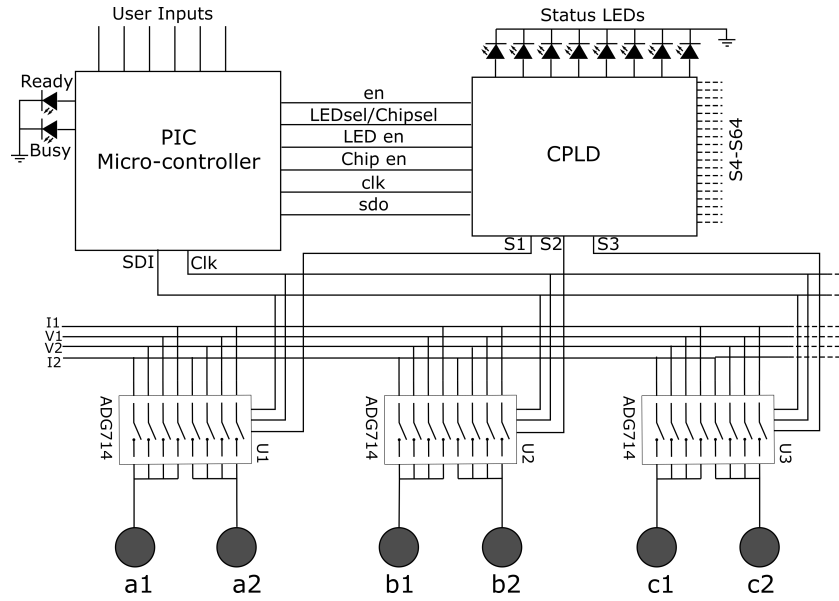


Figure 5.2: IREM circuit design. Shows the connection between the microcontroller (top left), the CPLD (top right) and three ADG714 switching ICs. The user inputs are six push-buttons used to trigger the programs. 'SDI' and 'Clk' are the SPI connection used to change the electrode configuration. 'en' is the channel used to activate SPI communication between the CPLD and microcontroller. 'LEDsel/Chipsel' is used for switching between chip addressing and LED addressing. 'LED en' and 'Chip en' are used to complete data transmission. 'clk' and 'sdo' are the serial communication between the microcontroller and the CPLD. 'S1 - S64' are used to enable the ADG714 ICs being addressed. 'I1, V1, V2, I2' are the impedance channels that connect to the electrodes through the switches. 'a1, a2, b1, b2, c1, c2' are individual electrodes/pixels from the electrode array.

design when connecting the other inputs and outputs. The second method is to use ICs that act as extension ports which increases the number of inputs and outputs; however the complexity of the program also increases. The third method is to use a complex programmable logic device (CPLD) which is an IC that can store hundreds of logic gates. It can be programmed to accept an address and select the switch associated to that address reducing the complexity of the program and also simplifies the PCB design. For the prototype used for experimentation, the third option for addressing the switches was used (fig 5.2).

The prototype was designed to have a PIC micro-controller which was programmed with the switching sequence, push-buttons were used as the user interface which connected directly to the PIC micro-controller. LEDs were also connected to the micro-controller, to indicate the busy and ready status; this allowed the user to monitor the progress of the sequence. One of the two serial communication ports of the PIC micro-controller was used to connect to all the serial ports of the 64 ADG714 switches, the other serial port and some control lines connected to the CPLD for addressing the different switches. A USB port was also included in the design which connected to the universal asynchronous receiver-transmitter (UART) port of the micro-controller. This allowed the program to also be controlled through a PC for full automation. The CPLD was programmed to have two functions. The first was to address the 64 switch ICs, the other was to connect to eight LEDs which indicate the progress of the switching sequence in 8-bit binary numbers. Since only one serial connection was used to send data to the CPLD from the micro-controller, four control lines were also used. One control line switched between the address function and LED display function, and the remaining three were used as enable and execute lines. If the enable pin was not set the serial data will not be accepted. The execute lines were used to hold data till the complete serial data was transmitted before being implemented. The execute lines were used to ensure no ICs were triggered accidentally while data was being serially received. This setup also allowed the topology used for the measurement to be easily changed by having one pixel connecting to multiple channels from the LCR meter.

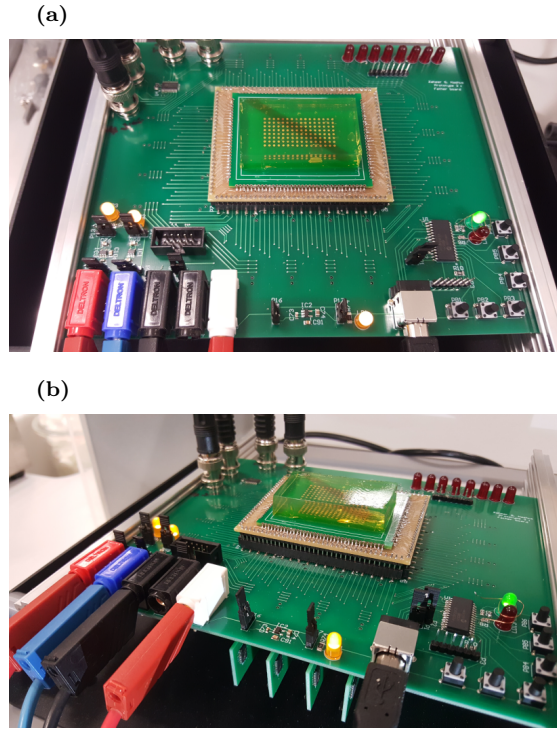


Figure 5.3: Phantom positioning over the electrode array used for experimentation

5.3.1 Electrode Array

An array of electrodes was constructed on a double-sided PCB to take impedance measurements experimentally. Each electrode on the PCB was a 1 *mm* diameter circular pad with a 0.2 *mm* hole in it. The hole was used to connect the electrode with the track leading to the edge of the PCB, and to allow for the connections to be made to the switching circuit. Figure 5.3a shows the positioning of the phantom on the electrodes from the top surface of the electrode array. Figure 5.3b shows the phantom positioned on the electrodes, viewed from the side .

5.3.2 Micro-controller Program

The program for the micro-controller is divided into; the initialisation section, the main loop and the different functions. The initialisation section is where the speed of the micro-controller is set, along with the input and output assignment. This is also the

section where different inbuilt functions of the micro-controller are initiated. The main loop is the program which dictates the actions executed by the micro-controller. This is where the different switching sequences are stored and executed. Functions are small sections of code which are executed multiple times. By storing these repeating sections of code into functions, they can be executed from anywhere in the main loop; this helps reduce the overall size of the program and also makes it more compact.

The program of the micro-controller of the IREM system was also divided into different sections. In the initialisation section, the speed, which is dependent on the clock frequency was set to 4 *MHz*, This speed was fast enough to switch between the states of the main loop. The IO ports, the serial communication features, and the UART feature were set up next. The main loop was designed to either be controlled through the USB port for automated sequence or through pressing the push button for pre-programmed sequence.

Pre-programmed Sequence

For the pre-programmed sequence, push-buttons 1 (PB1) and 2 (PB2) were used. PB1 was used to activate the switching sequence, and PB2 was used to activate the localised electrode sequence. The main loop waits for one of the two buttons to be pressed before moving forward. Red and green LEDs were used to indicate busy or ready status, respectively. The busy state indicated that the electrode pixels were being assigned to different channels; the ready state indicated that the assigning process was completed. Eight other LEDs were used to indicate the progression sequence of the scanning sequence using 8-bit binary counting. To change the progress indication LEDs, a function was created labelled *LEDSEL*, the flowchart of the function is shown in figure 5.4b. The function first sends a signal to the multiplexer in the CPLD to receive the serial byte containing the LED sequence. It then enables the serial transmission, followed by the enabling the LED input, the serial byte is then sent to the CPLD. The microcontroller then disables the serial transmission and LED input, this completes the transmission and switches the active LEDs. Similarly, a function was created to address the different

ADG714 ICs labelled *CHIPSEL*. Here the multiplexer in the CPLD was set to receive the serial byte containing the IC address. The serial transmission and address input were then enabled; the IC address was then serially transmitted. The serial transmission and the address input were then disabled, this ends the address transmission, and the addressed IC was selected as shown in figure 5.4c. Once the IC address had been sent to the CPLD, the pin allocations in the switch were sent to the ADG714 ICs directly through serial communication using a function called *TX*. The TX function sends a byte of data which directly relates to the eight SPST switches, where '0' indicates off and '1' indicates on.

Throughout the program, the above functions were executed multiple times to change the allocation of pixels to the different LCR meter channels following the scanning sequence or the localised electrode sequence. A snippet of one of the steps in the switching sequence is shown in figure 5.5. In the snippet of code, the *CALL* command is used to execute the function whose name is written after the command. Before each function is called the byte to be transmitted to the CPLD or the ADG714 IC are stored using the *MOVLW* command followed by the byte to transmit in hexadecimal form. Every time the pixel allocation is changed the format of the code is similar to the snippet shown with different bytes of data to be transmitted. The complete the scanning sequences described in section 4.6.1 was timed to take approximately 3 minutes. This timing can be reduced further by changing the delays between each step in the scanning sequence. However, a single impedance measurement from the LCR meter takes approximately 40 *ms*, therefore, the delay between each step of the scanning sequence was set to approximately 50 *ms*. The pre-programmed sequence is provided in the attached CD.

Automated Sequence

For the automated sequence, the microcontroller waits for an input from the UART port. It waits for one of four inputs '1', '2', '3' and '4' as an 8-bit binary word. When the micro-controller receives any of the four main inputs, it sends '10001000' in binary to the PC to indicate that it is ready to receive the next byte of data. Then it receives

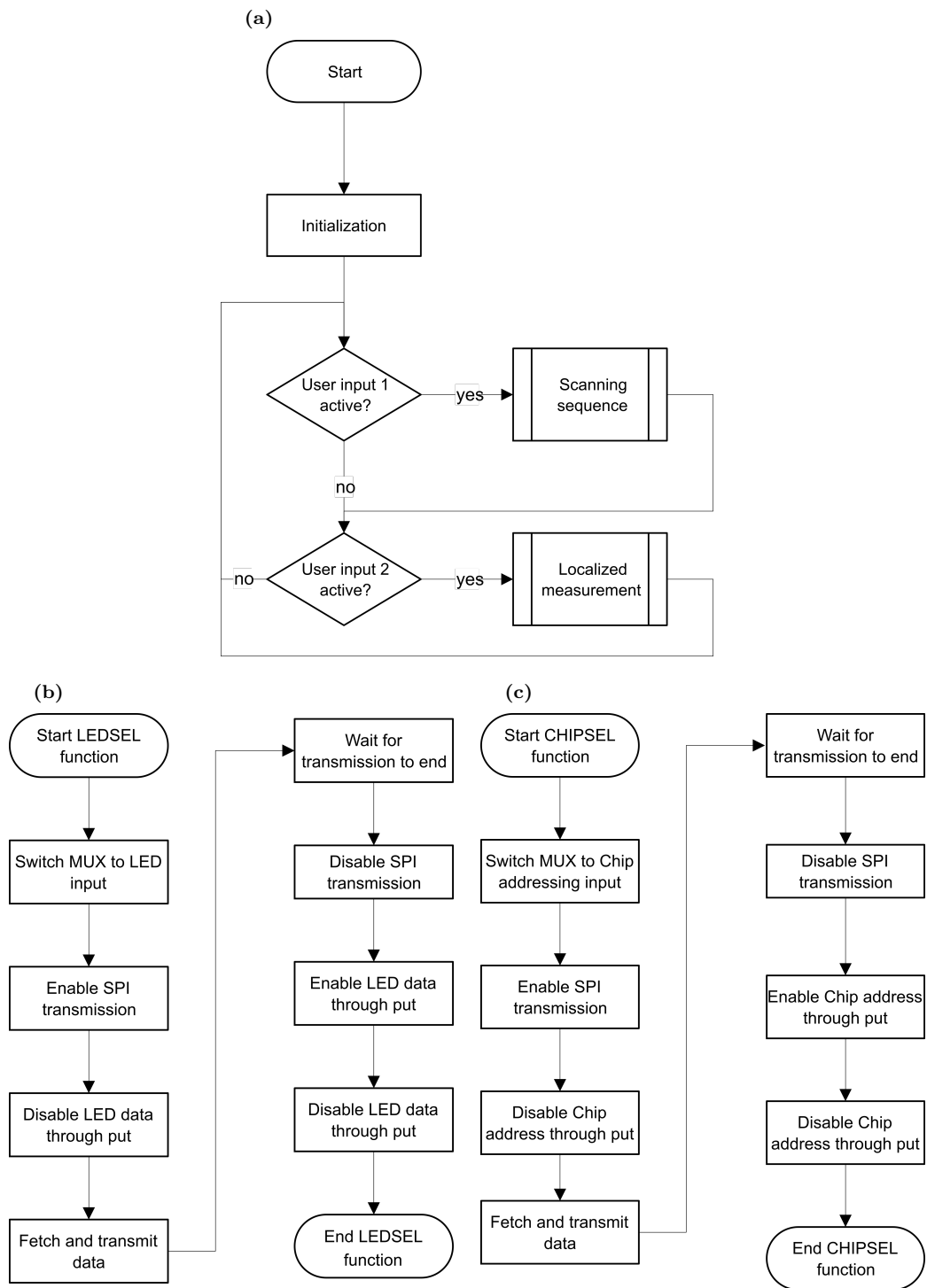


Figure 5.4: Flow chart for the micro-controller program. a) is the flow diagram of the main loop of the program. b) the flow diagram for the LED selection function. c) the flow diagram for the function used to select the different switching ICs.

```

S1      CALL      NEWT      ;
        MOVLW     0X01      ;LED FOR S1
        CALL      LEDSEL    ;
        MOVLW     0X02      ;CHIP FOR ELECTRODE (R1C1)
        CALL      CHIPSEL   ;
        MOVLW     0X80      ;MOVE VALUE OF A TO WREG
        CALL      TX        ;SEND SWITCH VALUE
        MOVLW     0X01      ;CHIP FOR ELECTRODE (R1C2)
        CALL      CHIPSEL   ;
        MOVLW     0X40      ;MOVE VALUE OF A TO WREG
        CALL      TX        ;SEND SWITCH VALUE
        MOVLW     0X40      ;CHIP FOR ELECTRODE (R1C3)
        CALL      CHIPSEL   ;
        MOVLW     0X20      ;MOVE VALUE OF A TO WREG
        CALL      TX        ;SEND SWITCH VALUE
        MOVLW     0X3E      ;CHIP FOR ELECTRODE (R1C4)
        CALL      CHIPSEL   ;
        MOVLW     0X08      ;MOVE VALUE OF A TO WREG
        CALL      TX        ;SEND SWITCH VALUE
        CALL      READY     ;
        CALL      DELAY10S

```

Figure 5.5: Program for first cycle of switching program

'1' the next byte received is used to set the eight LED using the *LEDSEL* function. When '2' is received, the next byte is used as the IC address which is sent to the CPLD using the *CHIPSEL* function. The byte received after '3' is used to assign the relevant electrode to the desired Impedance measurement channel through the *TX* function. '4' is used to disconnect all electrodes from the four channels. In this state the electrode selection and assignment is fully controlled by the PC, allowing for full automation of the IREM circuit. The automated sequence is provided in the attached CD.

5.3.3 CPLD Program

The CPLD can be programmed in many ways; one such method is to use logic block diagrams. This is the simplest method to program, understand and debug, as the program is similar to making a circuit diagram. In the CPLD, the first thing constructed was a serial to parallel converter; this was done by using eight D type flipflops. The pin where the serial data input (SDI) was received connects to the input of one D flip-flop. The output of one D flip-flop feeds into the next, in this manner, the eight D flipflops were

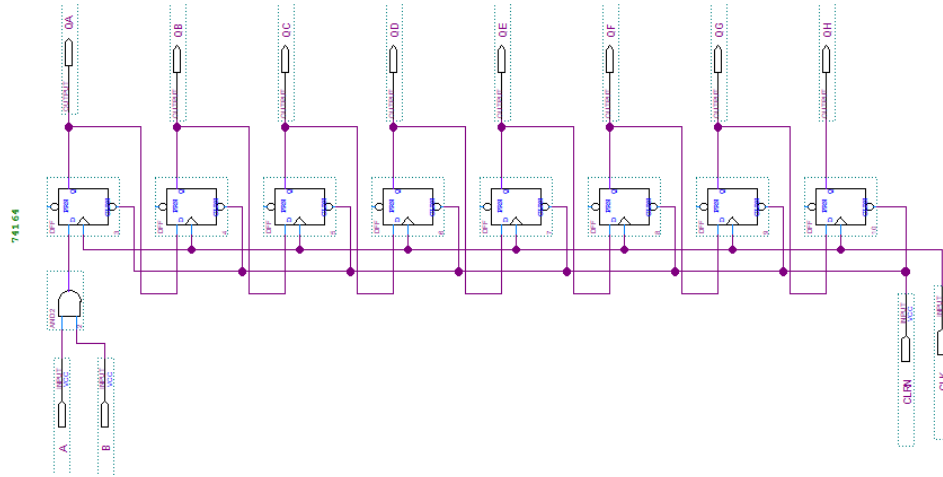


Figure 5.6: Design for the serial to parallel converter

connected. All the D flipflops were clocked using the clock pulse (CLK) transmitted from the micro-controller along with the serial data. The serially transmitted byte can be converted into a parallel output by taking the output of each D flipflop. Which is then used to perform different functions. Two such serial to parallel converters were constructed, one to control the eight LEDs and the other to address the different ICs. The serial to parallel converter is shown in figure 5.6. The next thing that was made was a simple 2 : 1 multiplexer (MUX) using two *AND* gates and an inverter. The MUX was directly incorporated into the design, without actually making a new component. Two 2 : 1 MUXs were used, one for the SDI and the other for CLK inputs. The output from the two MUX were fed into the two serial to parallel converters, and the control line for the two MUX were connected together and to the same input pin.

The outputs of the serial to parallel converters were connected to D flipflops which were used to hold the previous data. Which was done to ensure that during the data conversion, the previous data was held until after the complete serial word was received. The D flipflops used to hold the previous data, were clocked by the 'LED input' pin. The micro-controller controls the LED input pin. which needs to be set to high and then low again to transfer the data at the input of the D flip-flop to its output. The output of these D flipflops then fed directly to the output pins connecting to the LEDs. The clock inputs of the D flipflops on the IC addressing sides were also connected together and

connected to an input pin referred to as 'address input'. The outputs of these D flip-flops were connected to the control inputs of a 64-bit decoder and also a 4-bit decoder. The 64-bit decoder acts as a MUX whose input was set to logic 1, and the six control lines are used to connect the input to one of the 64 outputs. Since there are a total of 65 ICs to address and the first pin of the decoder was left floating, hence only 63 IC could be addressed using the 64-bit decoder. Therefore an additional 4-bit decoder was also used, the first pin of the 4-bit decoder was also left empty and the second pin was connected to the 64th IC. The third pin of the 4-bit decoder was connected to all the 64 ICs, this was done to allow all the 64-ICs to be addressed at the same time. The fourth pin of the 4-bit decoder was connected to the 65th IC, which was used to switch the connection of all the pixels between the LCR channels and ground to discharge any residual charge in the electrodes. The full design is shown in figure A.3.

5.3.4 Full Automation

In order to fully automate the system, a program was written in MATLAB R2018b. In the program, the electrode addresses and channel assignment were first saved in four arrays, one for each electrode in the tetrapole. A serial port was assigned for UART communication with the micro-controller and another for communication with the impedance analyser. The program cycles through the arrays and sends the electrode assignments to the micro-controller through the serial port. After sending the electrode assignment for the first tetrapole the program triggers the impedance analyser, it then receives the impedance measurements from the analyser and stores it in a matrix format. This process was implemented until all four tetrapole scanning orientations were completed. The results were then processed using the process described in section 4.6.2, which could be translated to the position of each electrode with respect to the vessel location. The program then identifies the electrodes located over the vascular structure; from those electrodes, the program selects the electrodes furthest apart and groups four electrodes to make a single active electrode. The electrode spacing was selected to cover the maximum length of the vessel under the electrode array. The electrode grouping was based

on the number of electrodes needed to cover the width of the vessel and selecting the same number of electrodes along the length to make a square electrode.

5.4 Experimental Setup

For the experiments, a phantom needed to be constructed matching the dimensions described in section 4.6. It was decided to use gelatin phantoms, as they are cheap, easily manufactured, allow the conductivity to be easily altered and allow layers of different concentrations to be stacked over one another to make a multi-layered phantom [88, 89]. The electrical properties of biological tissue are frequency-dependent and have conductive and reactive elements [91]. To create an accurate anatomical phantom, the conductivity of the different layers of the phantom needs to be matched to those of actual tissue. To change the conductivity of the different layers (5.1) was used [89] to obtain the concentration of NaCl needed to match the concentration. However, it is not as straightforward to replicate the reactive element [88, 89, 94]. For the phantom used in the experiments, the conductivity of the different tissues was calculated using (5.2) and values taken from [54]. Since the electrical properties of tissue are frequency-dependent and equation (5.1) can only use one conductivity value to give the NaCl concentration needed, a single frequency of 10 *KHz* was selected to make the gelatin phantom. The 10 *KHz* frequency was selected, as generally frequencies used in blood-related impedance measurements are usually between 10 – 100 *KHz* [41, 93]. Table 5.1 gives the NaCl concentrations used for constructing the gelatin phantom used in these experiments. A total of six phantoms were constructed, using two vessel diameters of 4 *mm* and 5 *mm*, each at three different depths of 5 *mm*, 6 *mm* and 7 *mm*. This was done to test whether the blood vessel close to the size of the carotid artery could be detected at different depths, as the depth and diameter of the carotid artery vary from person to person.

$$\sigma = 215 \times \frac{\text{grams of NaCl}}{\text{solution volume (ml)}} + 0.0529 \text{ (S/m)} \quad (5.1)$$

$$\varepsilon(\omega) = \varepsilon_{\infty} + \sum_{m=1}^4 \frac{\Delta\varepsilon_m}{1 + (j\omega\tau_m)^{(1-\alpha_m)}} + \frac{\sigma_i}{j\omega\varepsilon_0} \quad (5.2)$$

Table 5.1: NaCl Concentration

| Layer | Conductivity (S/m) | Concentration ($g/100\ ml$) |
|-------|------------------------|-------------------------------|
| Skin | 0.003 | 0.0014 |
| Fat | 0.043 | 0.02 |
| Blood | 0.70004 | 0.325 |

5.5 Phantom Design

The procedure to create the phantom was similar to that described in section 3.7.5. To create the final phantom, moulds were 3D printed containing the exact dimensions as used in the simulations. The mould consisted of multiple parts, the housing, spacers, mould holder and the moulds containing the necessary features for making complex phantoms. The housing was where the different layers were stacked together to make the phantom. The spacers were used to increase or decrease the depths of the features in the phantom. The mould holder was designed with a slot for easily swapping out different moulds, allowing for changing any feature of the phantom by simply changing the mould. Positive and negative moulds were made for different diameters of the blood vessel at a fixed angle. A featureless mould was also made to create the flat layers such as the top layer of the fat and skin layers.

The mould was designed such that it needed four stages to create the phantom matching the simulation model. In the first stage, a layer of fat was created with a groove in it. In the second stage, the groove in the fat layer was covered with a mirrored groove in the mould to create the blood vessel. In the third stage, the remaining layer of fat was created, embedding the blood vessel in the fat layer. The final stage creates the 2 mm layer of skin. With the help of the different moulds and spacers, the depth and diameter of the blood vessel were adjusted to match other simulations.

5.6 Flow Experiment Setup

For this set of experiments, a conductive silicon tube with a 5 *mm* outer diameter and 4 *mm* inner diameter was used. The tube's hardness was 60 shore, with a density of 1.17 *g/cm*³, a tensile strength of 6.2 *MPa*, tear strength of 13 *kN/m* and conductivity of $< 2 \Omega m$ [108]. This tubing was incorporated in the phantom to emulate a blood vessel, as it was the most flexible and conductive tubing available. The dimensions of the fat and skin layers were kept similar to those used in the scanning experiment. The depth at which the conductive tube was embedded into the phantom was set to 7 *mm* from the electrode surface. The orientation of the tubing was set to 0° to simplify the manufacturing process. The manufacturing process of the phantom will be described later in this chapter.

To emulate the pulsatile flow of blood, a pulsatile pump (Model 1423 PBP, Harvard Apparatus, US) was used, which mimics the pumping action of the heart. This pump allowed the SV, BPM and diastolic/systolic ratios to be controlled. The pump requires a reservoir of liquid to pump and two pipes, one leading from the reservoir to the pump (inlet) and the other leading from the pump back to the reservoir (outlet). The inlet of the pump was connected to a large pipe submerged in the reservoir. The outlet of the pump was connected to a pipe, which was split into two, creating a bifurcation. One end of the bifurcation led directly to the reservoir, the other end connected to a pressure transducer (Harvard Apparatus Pressure Transducer 60-3002, Serial # A-49837), the output of the pressure sensor was then connected to the conductive tube embedded in the phantom. The bifurcation was positioned at the outlet to reduce the volume of liquid passing through the conductive tubing. The length of the conductive tube was set to 2.5 *m*; this length was selected to allow the tube to easily be extended from the pump to the IREM circuit and then into the reservoir. a reservoir was used containing 600 *ml* of blood solution with a conductivity matching that of the conductive tubing.

5.7 Flow Phantom Design

The mould used for this experiment was different from the mould used previously; it consisted of a base and a lid. The base of the mould was designed to split in the centre along the length of the mould. It also contained two holes for the tubing to be placed into it. The lid for the mould consisted of the border used to ensure proper alignment, and the main section was a double-sided mould. The first side fits deeper into the base to make the fat layer and the second side which 2 *mm* shallower to make the skin layer. Since the conductivity of the tubing is 714.24% that of blood, the conductivity of the fat and skin solutions were also made 714.24% higher. The NaCl concentrations for the skin, fat and blood solutions are shown in table 5.2. The procedure used to set the phantoms is the same as that mentioned in section 5.5, however for this setup, only the skin and fat layers needed to be made.

Table 5.2: New NaCl Concentration

| Layer | Conductivity (<i>S/m</i>) | Concentration (<i>g/100 ml</i>) |
|-------|-----------------------------|-----------------------------------|
| Skin | 0.214 | 0.1 |
| Fat | 3.071 | 1.428 |
| Blood | 50 | 23.25 |

5.7.1 Impedance Analyzer Setup

The impedance analyser used to take impedance measurements was Keysight E4980A. The analyser was set up by going to the measurement setup option, the measurement type was changed to give the real and imaginary "R + X" values, the frequency was set to 10 *kHz*, and the trigger was set to bus driven, allowing the analyser to be triggered through MATLAB. The *Lcur* and *Hcur* were used as the current injection (CC) channels labelled I1 and I2 and *Lpot* and *Hpot* were used as the voltage measurement (PU) channels labelled V1 and V2. The channels were connected to the electrodes in the same order as those described in the scanning sequence.

5.7.2 Data Acquisition Program

Main Program and Functions

The program to interface with the LCR meter is similar to that described in section 3.7.4, however that program takes approximately 500 *ms* to execute. Since the number of steps for the complete scanning sequence was approximately 475 states, the scan would take approximately 1 hour to complete. In order to complete the scan as quickly and accurately as possible, it was necessary to speed up the time taken to take one measurement. Executing only the trigger command and extracting the impedance data takes approximately 40 *ms*, therefore, if the connection with the LCR meter was established beforehand it would reduce the time taken to complete the scan to approximately 3 minutes. For this purpose, the initial setup of the LCR meter and the parameter setup was stored in one function labelled *LCRmeterconnect* which was called before the start of the main program. The disconnection commands were stored in another function labelled *LCRmeterdc*, which was executed at the end of the main program.

Since the scanning sequence was pre-programmed, and there was no direct connection between the PCB and MATLAB program, synchronising the switching sequence with the triggering of the impedance measurement becomes very complicated. By using an Arduino UNO board that connects to the LED indicating the ready status of the micro-controller, the status of the scanning sequence could be monitored. Thus, the ready status of the micro-controller was used to indicate in the MATLAB program to trigger the impedance measurement. There were a total of six scans (vertical, horizontal, diagonal right, diagonal left) six different for-loops were included into the program. Each for loop was used as a means to address the location of the measurement in the corresponding matrix.

5.8 Experimental Procedure

Before placing the phantom on the electrode array, a 3D printed guide was placed over the electrodes to ensure that all phantoms were positioned in the exact same position.

This was done so that the electrodes were always positioned in the centre of the phantom. 150 *ul* of 0.9% saline solution was poured over the electrode array to ensure good contact between the electrodes and the phantom. The phantom was then positioned over the electrodes and let to rest for an hour to reach room temperature. This was done because it was discovered that as the temperature of the phantom goes from cold to room temperature, the conductivity of the phantom changes as shown in fig 5.7. After approximately one hour when the phantom reached room temperature, the scanning sequence described in section 4.7 was carried out using the electrode array. After the experiment, the phantom was removed, and the electrode array was wiped cleaned with de-ionised water and then with ethanol to ensure that there were no contaminants left behind that could interfere with the next experiment. The remaining sides of the phantom that didn't touch the electrode array were covered with clean film to prevent exposure to air to prevent loss of moisture during measurement.

5.9 Flow Experiment Procedure

Similar to the experiment procedure explained in the previous section, the phantom once set was positioned using the guide and left to reach room temperature for one hour. After one hour, the electrodes were grouped to form the localised electrodes for taking flow measurements. The localised electrodes were set to have the maximum distance between them. This was done, in order to obtain the maximum magnitude variation in impedance measurements, due to flow-related volume change. As it was discovered from conductivity variation simulations shown in section 4.4.8. The electrode pixels were grouped together to form localised electrodes over the tubing as shown in figure 5.8, and continuous impedance measurements were taken over 60 seconds.

The solution representing blood was pumped through the tubing with a SV of 50 *cc* at 40 *BPM*. In order to monitor the response of the continuous measurements, the SV was changed to three values 50 *cc*, 60 *cc* and 70 *cc* and the BPM was changed to three rates 20, 30 and 40 beats per minute. The low BPM used in the experiments was due to the limitation in the acquisition rate of the LCR meter.

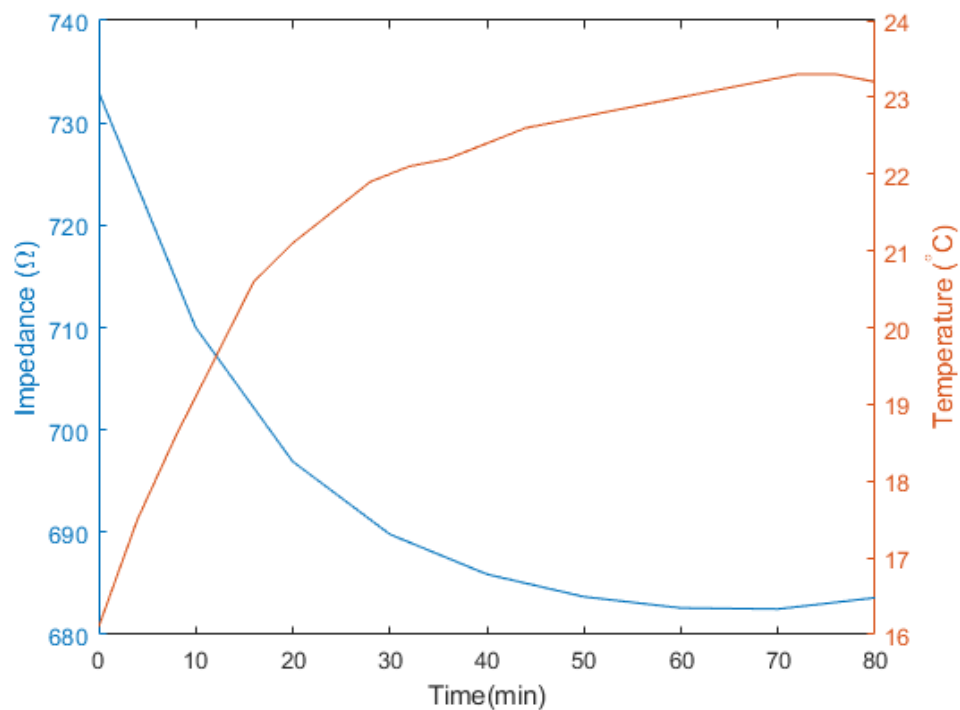


Figure 5.7: Relation between impedance and temperature over time. As temperature increases from cold to room temperature over time the measured impedance decreases as well, showing that impedance and temperature have an inverse relation

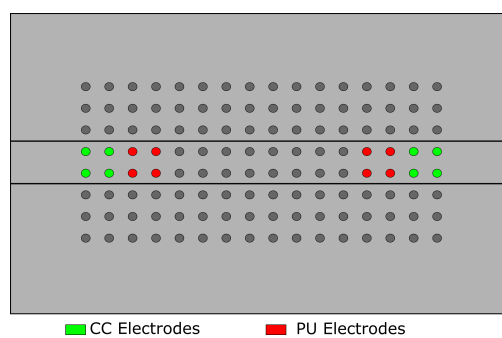


Figure 5.8: Localised electrode grouping, here CC electrodes are highlighted in green and PU electrodes are highlighted in red.

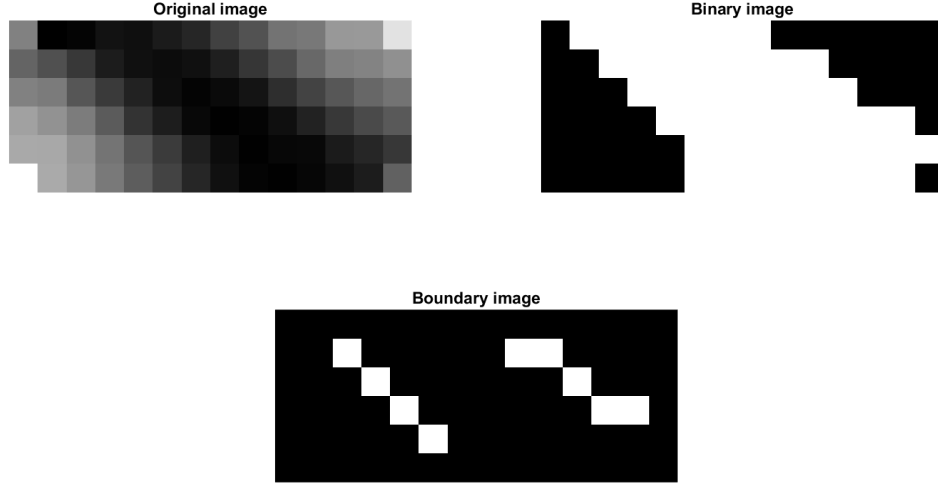


Figure 5.9: IREM experiment scan result. a) is the result obtained by combining the four scans, b) is the result after thresh holding and c) is the boundary obtained from the thresholded result

5.10 Results and Discussion

5.10.1 IREM Scanning Sequence

The results obtained from the IREM scan on the phantoms, were processed using the same process as that used on the simulation results. The result obtained after processing one of the phantoms are shown in figure 5.9. It was observed that the baseline impedance of the phantom was lower than that of the simulation model; however the trend obtained from the scans matched that of the simulation. Experimental results for the vessel detection at different depths matched those of the simulations as well as those of vessel diameter detection. These results proved the functioning of the IREM circuit and also proved that the phantoms used in the experiments matched the models used in simulations. The vessel orientation calculated from the experimental results had an 80% accuracy, based on the table shown in table 5.3.

Table 5.3: Blood vessel Orientation, expected vs measured

| Phantom Number | Orientation | |
|-------------------|-------------|--------------|
| | Actual (°) | Measured (°) |
| 1 | -37 | -38.4 |
| 2 | | -40.26 |
| 3 | | -40.26 |
| 4 | | -38.38 |
| 5 | | -31.87 |
| 6 | | -35.13 |
| Average angle | | -37.37 |

5.10.2 Flow Parameter Variation

The LCR meter used allows a fixed number of samples per second to be taken. Therefore, most feasible way to increase the sampling rate is to reduce the BPM of the pump. For this purpose, three BPM values were used to test if the resolution would improve. For these experiments, measurements were taken from both the pressure sensor as well as with the impedance analyser. From the results shown in fig 5.10, it was observed that for every pulse of the pump, a voltage spike appeared in the pressure measurement(top graph). The impedance measurement(bottom graph), on the other hand, showed a decrease in impedance for each pulse. The pressure measurements also showed that the pressure output from the pump was not constant, which also influenced the impedance measurement making it difficult to identify the variation in the pulse waveform. Therefore the impedance measurements corresponding to peaks in the pressure measurement greater than 95% of the largest peak were averaged to obtain a single pulse measurement (fig 5.11). The averaging was carried out on three data sets of the same setup. Taking the minimum impedance and maximum impedance from the averaged single pulse and subtracting them resulted in the total magnitude change due to the impedance of a single pulse. Implementing this method on the different parameter variation and plotting them together resulted in figure 5.12. It was observed that increasing the BPM while keeping the SV constant, increased the magnitude change in impedance measured, the same was also observed when BPM was fixed, and SV was increased. These experiments showed that the waveform captured correspond to the pulsatile output of the pump and that

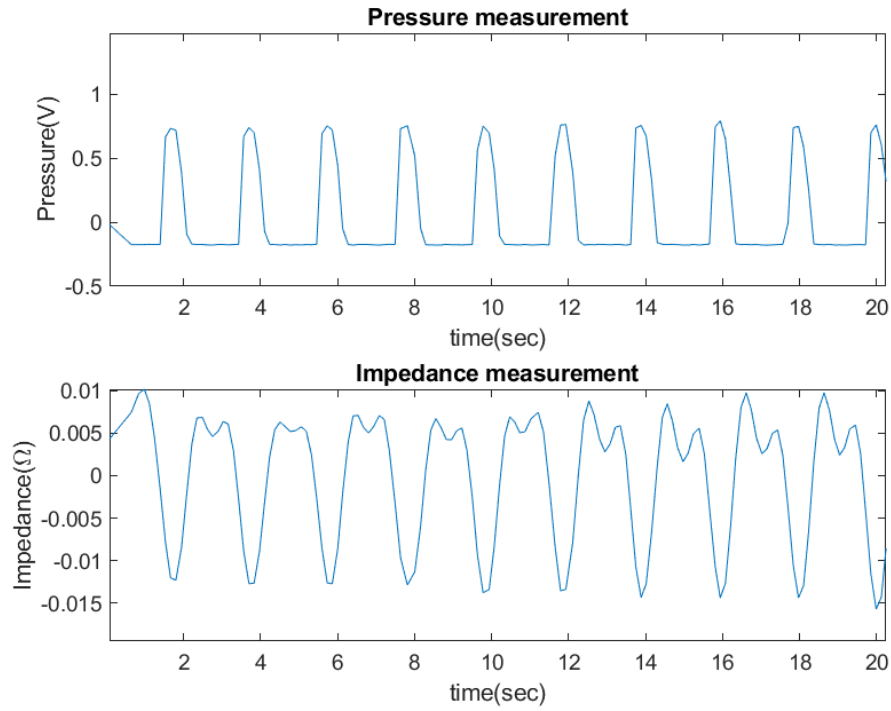


Figure 5.10: Pressure vs impedance measurement, the top graph shows the output of the pressure sensor and the bottom graph shows the measured impedance value after filtering

variations made to the settings of the pump influence the measured impedance magnitude. The change in impedance magnitude was attributed to the change in pressure as the same change was observed in the pressure transducer measurements. The results of varying the BPM showed that, by decreasing the BPM the pulse wave could be captured efficiently. However, it was also observed that the pump started to malfunction at 20 BPM. Therefore for further experiments it was decided to keep the BPM fixed at 30.

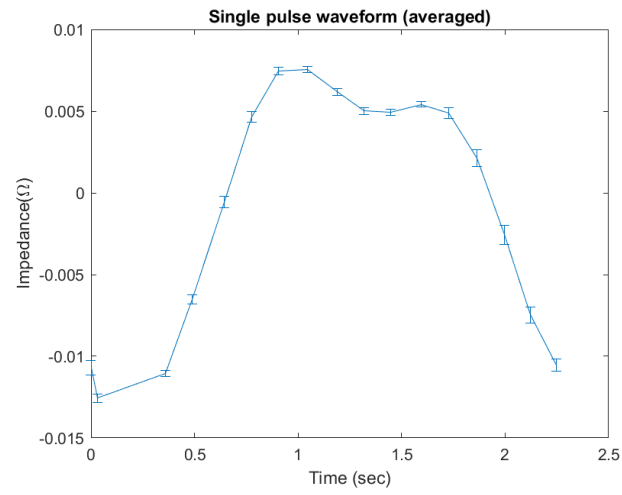


Figure 5.11: Single pulse after averaging multiple pulses

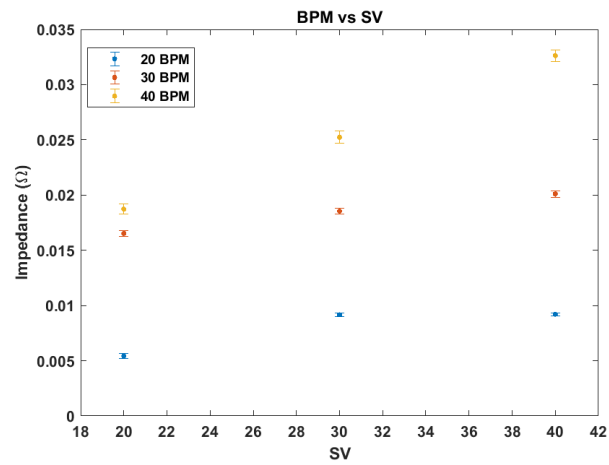


Figure 5.12: Variation of SV and BPM. The graph shows the variation of SV for each BPM value.

5.11 Conclusion

In this chapter, the design of the IREM circuit was described in detail. The scanning experiment results obtained using the circuit showed a good correlation between the simulation and experimental results. It has been demonstrated that blood vessels can be identified using SPVT scans, and IPG measurements can be obtained using localised measurements. The next phase would be to test whether occlusions in blood vessels can be identified using SPVT scans and localised IPG measurements which will be covered in the next chapter.

Chapter 6

Using IREM for Occlusion Detection

In the previous chapter, a detailed description of the IREM circuit was introduced. The scanning ability and the ability to take localised measurement of the IREM system were explored experimentally with the help of phantoms in the previous chapter. It was shown that by using the SPVT scan, vascular structures could be detected transcutaneously. From the scans, various details about the vascular structures can also be extracted, such as; the orientation and the thickness. It was also demonstrated that localised flow measurements using the IREM circuit have a higher sensitivity to flow variation than pseudo-stripe electrodes.

In this chapter, the ability of the IREM system to detect occlusions will be explored through simulations and experiments. The phantom and models used in the previous chapters will be altered to include occlusions of varying sizes. This is done to identify the influence of occlusion on SPVT scans. Flow experiments will also be conducted, where an occlusion will be incorporated into the phantom, to identify whether it can be detected through localised flow measurements.

6.1 Occlusion Study Method

The ability of the IREM system to detect occlusions through SPVT scans was tested through simulations. In these simulations, the dimensions of the model were altered, whereby, the length and width were doubled, the size of the electrode array was increased to 20×30 , and an occlusion was introduced in the blood vessel. The reason for making these changes was due to the inability of the previous SPVT scan to detect the whole vessel with a bifurcation, and to increase the resolution. This also increased the scan area, making it easier to locate an occlusion from the rest of the vessel. As a correlation between simulation and experiments was already demonstrated in the previous chapter, these simulations were not implemented experimentally. Since flow experiments could not be performed in simulations, the influence of the occlusion on flow parameter was explored through experiments. An occlusion was then introduced in the tube, by tying a string around a section of the tube. The percentage of occlusion was varied by altering how tightly the string was tied. The tube with the occlusion was then included in the phantom, measurements were taken similar to those taken during the flow experiment in the previous chapter.

6.2 Occlusion Scanning Simulation

In order to increase the resolution and to make the occlusion more realistic, the dimensions of the length and width of the model were doubled to 100 mm and 60 mm . The diameter of the blood vessel was fixed to 5 mm , located at a depth of 7 mm with an angular orientation of 37° . The number of electrodes pixels and the array orientation was changed from '128 electrode pixels arranged as a 8×16 array' to '600 electrode pixels arranged as a 20×30 array', like the expanded bifurcation model described in section 4.7.2. The occlusion was set to an ellipsoid of ' $x \times y \times z$ ' diameters of ' $12\text{ mm} \times c \times 6\text{ mm}$ ', where ' c ' is the diameter of the vessel in millimetres multiplied by percentage occlusion. The ellipsoid was rotated by 37° such that the x-axis of the ellipsoid was parallel with the length of the blood vessel. The percentage occlusion was then altered to go from 20% to

80% occlusion with a step change of 20% occlusion. This process was also implemented for the bifurcation, the centre of the ellipsoid was moved further down the right branch of the bifurcation, such that the occlusion was positioned approximately 4 *mm* from the point where the blood vessel splits into two branches (fig. 6.1b).

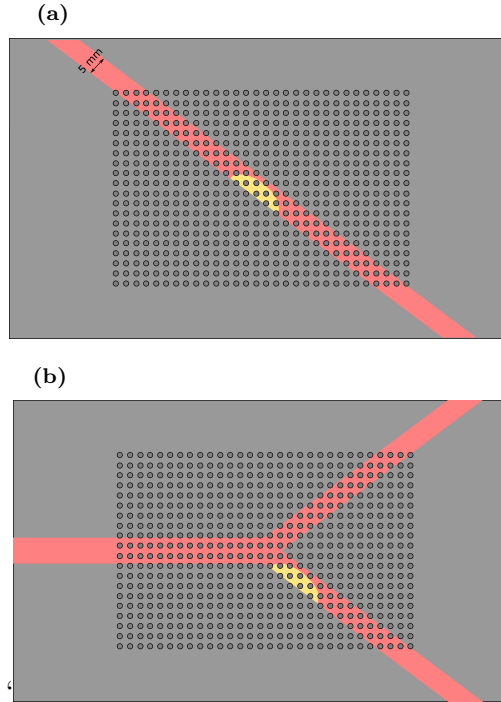


Figure 6.1: Expanded model: Occlusion positioning. a) Location of occlusion in straight line vessel model. b) Location of occlusion on the right branch of the bifurcation

6.3 Occluded Flow Phantom Design

For the phantom used in the occluded flow experiment, an occlusion was created by tying a string around the tube. For this, the circumference of the tube was calculated, using the outer diameter of the tube. The diameter was then reduced to 4 *mm*, and the circumference was calculated, to get the 20% occlusion. Similarly, the circumference was calculated for a diameter of 3 *mm* to get the 40% occlusion. Markings were made on the string at the desired length using the calculated circumference for the two occlusions. The strings were tied to create the occlusion in the tubing using the markings as a guide.

Table 6.1: Circumference of tube and the occlusions

| Diameter of tubing (<i>mm</i>) | circumference (<i>mm</i>) |
|----------------------------------|-----------------------------|
| 5 | 15.71 |
| 4 | 12.57 |
| 3 | 9.42 |

The tube was then embedded into the phantom, keeping the occlusion in the centre of the phantom. The circumference of the original tube and the two occlusions are given in table 6.1. The tube with the occlusion was then used to create the phantom, as described in section 5.7.

6.4 Occluded Flow Experimental Procedure

Similar to the experiment procedure explained in section 5.9, the phantom once set was positioned using the guide and left to reach room temperature for one hour. After one hour, the electrodes were grouped to form the localised electrodes for taking flow measurements. The localised electrodes were set to have the maximum distance between them. The electrode pixels were formed into grouping that was made up of pixels localised over the tubing, as shown in figure 5.8 and continuous measurements were taken over 60 seconds. Occlusion flow studies were carried out with the SV and BPM values fixed to 50 cc at 30 BPM based on the results obtained from the experiment in section 5.10.2. The occlusions used for the flow experiments were set to 0% 20% and 40%. This was done to observe how the occlusion influences the flow impedance in any detectable way.

6.5 Results and Discussion

6.5.1 Detection of Occlusion

Straight Line Vessel

The results obtained from the simulation described in section 6.2 were analysed using the process described in section 4.6.2 to measured the occlusion percentage. Figure 6.2 shows

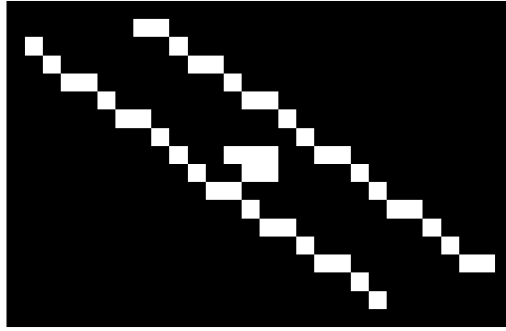


Figure 6.2: 3D simulation: 20% occlusion scan result after processing

Table 6.2: Actual versus measured occlusion percentage in a straight line vessel

| Actual occlusion (%) | Occlusion Detected |
|----------------------|--------------------|
| 0 | no |
| 20 | yes |
| 40 | yes |
| 60 | yes |
| 80 | yes |

the image obtained after processing, the area with white within the vessel boundary indicates the occlusion. The percentage of occlusion was calculated by measuring the vessel diameter across the occlusion site and dividing it by the vessel diameter from a site with no occlusion. This process was implemented for all the different occlusions simulations to create table 6.2, which show the actual occlusion percentage versus the measured occlusion percentage. From the table it was observed that the percentage of occlusion could be measured for straight-line vessels with an accuracy of 98%.

Bifurcation

Simulations with occlusions implemented on the vessel with a bifurcation were processed as previously, the boundary and occlusion were extracted from the scans, as shown in fig 6.3. Table 6.3 shows the actual occlusion percentage vs the measured occlusion percentage. It was observed that for a bifurcation with occlusion, the scanning method could detect the occlusion percentage with an accuracy of 98%.

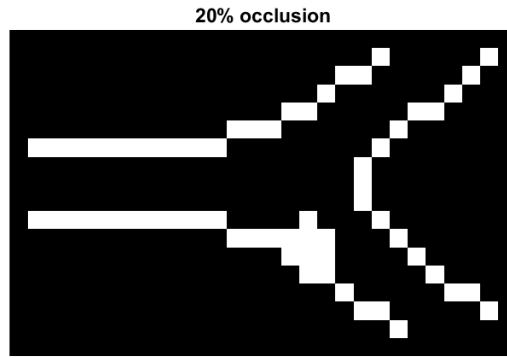


Figure 6.3: 3D simulation: 20% occlusion scan result after processing in a bifurcation

Table 6.3: Actual versus measured occlusion percentage in a bifurcation

| Actual occlusion (%) | Occlusion Detected |
|----------------------|--------------------|
| 0 | no |
| 20 | yes |
| 40 | yes |
| 60 | yes |
| 80 | yes |

6.5.2 Occlusion flow Study

Using the same filtering and averaging method used in section 5.10.2, the total change in impedance between the different occlusions was compared. Experiments were implemented using 0%, 20% and 40% occlusions. Since the occlusions were created using a thread tied around the tube, the accuracy of the created occlusion was low. The results obtained for the 20% occlusion were not consistent, therefore they were excluded from the results shown here. Figure 6.4, shows the change in impedance with respect to percentage occlusion. Here, the change is shown for measurements taken using localised electrode grouping. It was observed that, as the percentage occlusion increases, the impedance change obtained increases. This change in impedance can be attributed to the increase in pressure of blood flowing through the blood vessel due to the presence of the occlusion. To further assess the morphology of the pulsatile waveform was analysed. For this purpose a ratio between the two peaks and the dicrotic notch was taken for different occlusion percentages (fig 6.5). The blue bar represents the initial peak and

the red bar represents the peak after the dicrotic notch. Bars shown in 1 belong to 0% occlusion, and bars in 2 are for 40% occlusion. The peak ratios for different occlusion percentages were compared and it was observed that for a 40% occlusion the two peaks were closer to each other. Whereas, for 0% occlusion, the difference between the two peaks was larger. The results obtained indicate that in the presence of occlusion the pressure and the morphology of the plethysmographic waveform change and this leads to the conclusion that localised IPG measurements can be used to identify occlusion.

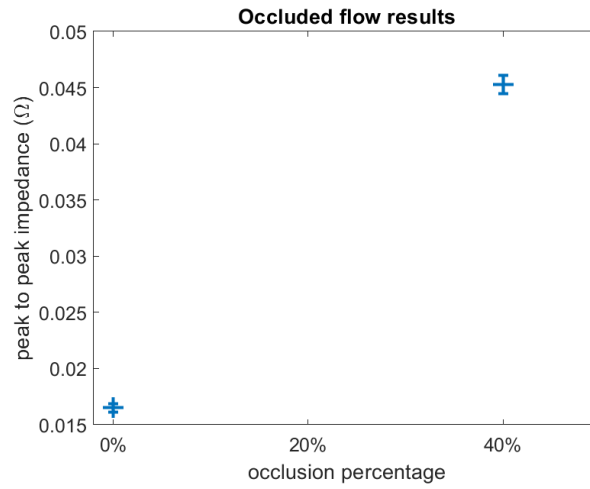


Figure 6.4: Flow study with occlusion.

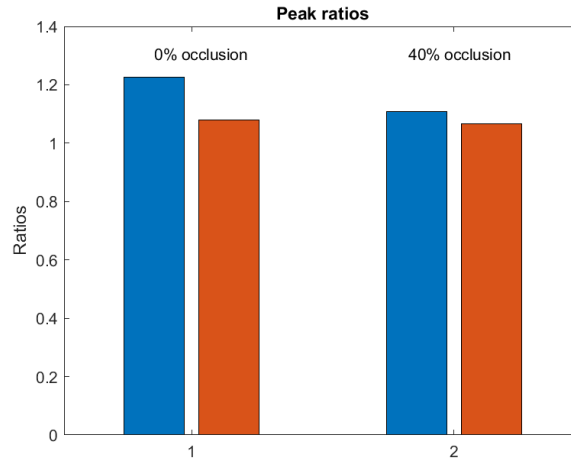


Figure 6.5: Ratio of two peaks with the dicrotic notch. The blue and red bars are the first and second peak respectively

6.6 Conclusion

The aim of the simulations and experiments covered in this chapter was to determine whether it was possible to detect occlusion in the blood vessel through scanning and localised measurements. The scanning simulations on a straight line and bifurcated blood vessels showed that detection of occlusions was possible with some degree of error. The flow experiment showed that as the occlusion was increased, the magnitude of the pulse measured increased, resulting from the increase in pressure and volume in the blood vessel. The flow results also showed that the morphology of the pulsatile waveform changed with a change in occlusion percentage. The aim of this part of the work - to assess IREM for occlusion detection - is positively conclusive, mainly through the SPVT scans but also through localised IPG measurements. Still, the author feels that further future research is needed to solidify the latter method, possibly using a more repeatable occlusion fabrication and with a range of degrees of occlusions. Overall, the work carried out in this chapter, confirmed the possibility of using the IREM system for detection of occlusion in vascular structures.

Chapter 7

Conclusion And Future Work

7.1 Conclusion

The motivation behind this work was to make available diagnostic technology that will potentially enable routine screenings for assessing the carotid artery, thus potentially saving thousands of lives by reducing stroke incidents. This thesis explored the merits of a method that allows for electrodes to be automatically addressed for the purpose of localising them over the desired vessel and take measurements relevant to the indicators of arteriosclerosis through simulations and experiments. In order to accomplish this, idealised models were designed and tested in simulations, and custom circuitry was also designed for addressing the electrode array for experimental testing of the method.

Before proceeding with the complete method, it was essential to assess whether groups of small electrodes shorted together perform similarly to larger electrodes of the same effective area. To test this, simulations were designed in chapter 3, where stripe electrodes were replaced with segmented electrodes covering approximately the same area termed as pseudo-stripe electrodes. These simulations showed that pseudo-stripe electrodes gave the same impedance measurements as those obtained using stripe electrodes. To further test this setup, the single segment variable tetrapole (SSVT) scan was also implemented to test the possibility of identifying electrode segments located over the vascular structure, which gave positive results as long as the electrode segments

were positioned over the electrodes. Comparisons were also made between measurements taken using pseudo-stripe electrodes and electrode segments identified through the simple scan termed as localised electrodes, which showed that measurements taken using localised electrodes had a higher sensitivity than those made using pseudo-stripe electrodes. Custom addressing circuitry was also covered in this chapter, and a number of simulations were also implemented experimentally with the help of anatomical phantoms. The results obtained experimentally were in agreement with those obtained through simulations. This helped verify that it is possible to create electrodes of varying size by grouping a number of small electrode segments together. It also helped prove that it is possible to identify electrode segments positioned over a targeted vascular structure using the SSVT scan. However, the DRE system still required the electrodes to be manually positioned over the vessel of interest and could only be used to identify the electrodes segments positioned over the vascular structure. This is helpful when taking plethysmographic measurements but does not give any detail about the features of the vascular structure.

Due to the limitations of DRE, further simulations were implemented where the area previously covered by a tetrapole - segmented or stripe - electrodes was fully covered by a two-dimensional matrix array of electrode pixels. This was described in chapter 4, where simulations were carried out on a novel scanning method using single-pixel variable tetrapole (SPVT) scans with different scanning orientations. Simulations were also performed on blood vessels with different parameters and features. The results from the simulations demonstrated that the proposed SPVT scan could identify vessel orientation, vessel feature and electrode pixels located over the vascular structure with high accuracy. However, more research in image analysis is needed to extract the vessel diameter and depth variation accurately.

To test the method implemented in simulations with phantom experimental studies, a new addressing circuitry was designed. This was covered in chapter 5, where the circuit design, MATLAB, CPLD and assembly programs were described. The design of the phantoms used for experiments, which mimicked the simulation models were also described. The results obtained from the experimental implementation of the SPVT scan

were in agreement with the results obtained from simulation, confirming the accuracy of the simulations. The phantom experiments confirmed the validity of the simulations as well as proving that localised electrodes can be used to perform impedance plethysmography measurements. Therefore, it confirmed that the addressing system could be used to automatically reconfigure the electrodes, so that they could be localised only to the vessels of interest.

The ability of the system to identify the indicators of arteriosclerosis was tested next through simulations and experiments were covered in chapter 6. Here an occlusion was introduced in the simulation model of a straight line vessel as well as a bifurcated vessel. This was done to test the ability of the SPVT scan for detecting the occlusion. Similarly, the possibility of detecting the occlusion through flow measurements was also explored, by introducing an occlusion to the pipe used in the phantom. The scanning simulations on the straight line and bifurcated blood vessels showed that it was possible to detect the occlusion with an accuracy of 98%. The flow experiment showed that as the occlusion was increased, the magnitude of the pulse measured increased, resulting from the increase in pressure and volume in the blood vessel. The morphology of the pulsatile waveform also changed for different occlusion percentages. This showed that the occlusion could be detected mainly through the SPVT scans but also through localised IPG measurements.

Even though the models and phantoms used in simulations and experiments were idealised, they were sufficient to prove the concept explored in this thesis. They showed that the vessel orientation and features could be identified through SPVT scans as well as identify the electrodes localised over the vessel. It also showed that the electrodes could be reconfigured to be localised only over the blood vessel of interest, and take measurements that are relevant to the arteriosclerosis indicators that can be used for early detection. A working IREM circuit was also designed and tested to be used for this purpose. There is still room for more work that can be carried out when it comes to more complex simulations, in-vivo studies and the feature recognition. However, the work presented in this thesis is sufficient proof that impedance measurements could potentially be used as an early detection method. Which is: rapid, potentially inexpensive, safe and

operator-independent diagnostic method, which will ultimately allow for frequent routine tests to be carried out for detection of arteriosclerosis.

7.2 Future work

The IREM circuit is at such a stage that it can now be used for a volunteer study to detect vascular structures in the arm, with the aid of additional circuitry it can even be powered by a 9V battery making it more portable. Another important step would be to design a simulation model using MRI images to build an anatomically consistent model to identify the influence of other tissue types on the scanning methods. The author feels that further future research is needed to solidify the localised IPG measurement, possibly using a more repeatable occlusion fabrication and with a range of degrees of occlusions.

From the circuitry point of view, the next steps would be to miniaturise the circuit, this can be achieved by creating an integrated circuit containing all the switching circuitry in it. In order to allow the user to increase the number of electrodes to be used, it is necessary to have a way to use two or more switching circuits in conjunction with one another. Another aspect would be to design a disposable flexible array of electrodes that can be placed on the desired site without causing discomfort to the patient.

The scanning and localisation capabilities of IREM are not limited to vascular structures, and it can also be used for identification of cancer cells on the skin, in breasts and other areas closer to the surface of the skin. The IREM circuit could also be used along with EIT with a larger number of electrodes allowing of a virtually moving electrodes rather than fixed location electrodes; this might increase the spatial resolution of the EIT scans currently being implemented. It can be used along with a stimulation circuit for scanning wound areas and electrically stimulate the wound

The switching system is not limited to impedance measurements, and it can also be used with other modalities such as optics. Through this switching method, it might even be possible to combine two modalities such as impedance and optics such as having an array which contains electrodes as well as optic sensors and emitters.

Bibliography

- [1] E. Cowles Andrus, E. V. Allen, H. Houston Merritt, G. Lyman Duff, R. A. Moore, F. E. Kendall, H. B. Shumacker, R. L. Levy, and I. S. Wright, “The pathogenesis of arteriosclerosis,” *International Journal of Epidemiology*, vol. 44, no. 6, pp. 1791–1793, 12 2015.
- [2] D. Lukanova, N. Nikolov, K. Genova, M. Stankev, and E. Valcheva, “The accuracy of noninvasive imaging techniques in diagnosis of carotid plaque morphology,” *Rentgenologiya i Radiologiya*, vol. 53, no. 4, pp. 258–265, 2014.
- [3] J. Park, A. Razuk, P. Saad, G. Telles, W. Karakhanian, A. Fioranelli, A. Rodrigues, G. Volpiani, P. Campos, R. Yamada, V. Castelli, and R. Caffaro, “Carotid stenosis: what is the high-risk population?” *Clinics*, vol. 67, no. 8, pp. 865–870, 8 2012.
- [4] V. C. Scanlon and T. Sanders, *Essentials of Anatomy and Physiology*. F. A. Davis, 5 2007.
- [5] K. Van de Graaff, R. W. Rhees, and S. L. Palmer, *Schaum’s Outline of Human Anatomy and Physiology, Third Edition (Schaum’s Outline Series)*. Schaums Outline Series, 2009.
- [6] S. S. Mader, *Understanding Human Anatomy and Physiology (5th Edition)*. The McGrawHill Companies, 2005.
- [7] E. M. Tuzcu, S. R. Kapadia, E. Tutar, K. M. Ziada, R. E. Hobbs, P. M. McCarthy, J. B. Young, and S. E. Nissen, “High Prevalence of Coronary Atherosclerosis in

- Asymptomatic Teenagers and Young Adults : Evidence From Intravascular Ultrasound,” *Circulation*, vol. 103, no. 22, pp. 2705–2710, 2001.
- [8] D. H. Peters, A. Garg, G. Bloom, D. G. Walker, W. R. Brieger, and M. Hafizur Rahman, “Poverty and access to health care in developing countries,” *Annals of the New York Academy of Sciences*, vol. 1136, pp. 161–171, 2008.
- [9] S. Choi, “Powering point-of-care diagnostic devices,” *Biotechnology Advances*, vol. 34, no. 3, pp. 321–330, 2016. [Online]. Available: <http://dx.doi.org/10.1016/j.biotechadv.2015.11.004>
- [10] M. Zarei, “Portable biosensing devices for point-of-care diagnostics: Recent developments and applications,” *TrAC - Trends in Analytical Chemistry*, vol. 91, pp. 26–41, 2017. [Online]. Available: <http://dx.doi.org/10.1016/j.trac.2017.04.001>
- [11] MayoClinic, “Ischemic stroke - Mayo Clinic.” [Online]. Available: <https://www.mayoclinic.org/ischemic-stroke/img-20009031>
- [12] T. Adla and R. Adlova, “Multimodality imaging of carotid stenosis,” *International Journal of Angiology*, vol. 24, no. 3, pp. 179–184, 2014.
- [13] M. M. Horrow, J. Stassi, A. Shurman, J. D. Brody, C. L. Kirby, and H. K. Rosenberg, “The limitations of carotid sonography: Interpretive and technology- related errors,” *American Journal of Roentgenology*, vol. 174, no. 1, pp. 189–194, 2000.
- [14] M. Anzidei, A. Napoli, F. Zaccagna, P. Di Paolo, L. Saba, B. Cavallo Marincola, C. Zini, G. Cartocci, L. Di Mare, C. Catalano, and R. Passariello, “Diagnostic accuracy of colour Doppler ultrasonography, CT angiography and blood-pool-enhanced MR angiography in assessing carotid stenosis: a comparative study with DSA in 170 patients,” *La radiologia medica*, vol. 117, no. 1, pp. 54–71, 2012. [Online]. Available: <http://link.springer.com/10.1007/s11547-011-0651-3>
- [15] E. S. Bartlett, T. D. Walters, S. P. Symons, and A. J. Fox, “Quantification of carotid stenosis on CT angiography,” *American Journal of Neuroradiology*, vol. 27, no. 1, pp. 13–19, 2006.

- [16] T. J. Kaufmann and D. F. Kallmes, “Utility of MRA and CTA in the evaluation of carotid occlusive disease,” *Seminars in Vascular Surgery*, vol. 18, no. 2, pp. 75–82, 2005.
- [17] B. M. Dale, M. A. Brown, and R. C. Semelka, *MRI Basic Principles and Applications*. Chichester, UK: John Wiley & Sons, Ltd, 10 2015, vol. 3.
- [18] S. Grimnes and . G. Martinsen, *Bioimpedance and Bioelectricity Basics*. Elsevier, 2015.
- [19] A. Ikarashi, M. Nogawa, T. Yamakoshi, S. Tanaka, and K. I. Yamakoshi, “An optimal spot-electrodes array for electrical impedance cardiography through determination of impedance mapping of a regional area along the medial line on the thorax,” *Annual International Conference of the IEEE Engineering in Medicine and Biology - Proceedings*, pp. 3202–3205, 2006.
- [20] M. Theodor, D. Ruh, M. Ocker, D. Spether, K. Förster, C. Heilmann, F. Beyersdorf, Y. Manoli, H. Zappe, and A. Seifert, “Implantable impedance plethysmography,” *Sensors (Switzerland)*, vol. 14, no. 8, pp. 14 858–14 872, 2014.
- [21] S. Ansari, A. Belle, K. Najarian, and K. Ward, “Impedance plethysmography on the arms: Respiration monitoring,” *2010 IEEE International Conference on Bioinformatics and Biomedicine Workshops, BIBMW 2010*, no. 1, pp. 471–472, 2010.
- [22] “Dräger PulmoVista® 500.” [Online]. Available: http://www.draeger.com/sites/en_uk/Pages/Hospital/PulmoVista-500.aspx
- [23] B. H. Brown, D. C. Barber, a. H. Morice, and a. D. Leathard, “Cardiac and respiratory related electrical impedance changes in the human thorax.” *IEEE transactions on bio-medical engineering*, vol. 41, no. 8, pp. 729–34, 1994.
- [24] D. C. Barber and B. H. Brown, “Applied potential tomography.” *Journal of the British Interplanetary Society*, vol. 42, no. 7, pp. 391–393, 1989.

- [25] S. a. Weber, N. Watermann, J. Jossinet, J. A. Byrne, J. Chantrey, S. Alam, K. So, J. Bush, S. O’Kane, and E. T. McAdams, “Remote wound monitoring of chronic ulcers,” *IEEE Transactions on Information Technology in Biomedicine*, vol. 14, no. 2, pp. 371–377, 2010.
- [26] Y. H. Shash, M. A. A. Eldosoky, and M. T. Elwakad, “The effect of vascular diseases on bioimpedance measurements: mathematical modeling,” *Biomedical Research and Therapy*, vol. 5, no. 6, pp. 2414–2431, 6 2018.
- [27] J.-J. Wang, W.-C. Hu, T. Kao, C.-P. Liu, and S.-K. Lin, “Development of forearm impedance plethysmography for the minimally invasive monitoring of cardiac pumping function,” *Journal of Biomedical Science and Engineering*, vol. 04, no. 02, pp. 122–129, 2011.
- [28] J. J. McGrath, W. H. O’Brien, H. J. Hassinger, and P. Shah, “Comparability of spot versus band electrodes for impedance cardiography,” *Journal of Psychophysiology*, vol. 19, no. 3, pp. 195–203, 2005.
- [29] R. W. Gotshall and W. R. Sexson, “Comparison of band and spot electrodes for the measurement of stroke volume by the bioelectric impedance technique,” *Critical Care Medicine*, vol. 22, no. 3, pp. 420–425, 1994.
- [30] M. Qu, Y. Zhang, J. G. Webster, and W. J. Tompkins, “Motion Artifact from Spot and Band Electrodes During Impedance Cardiography,” *IEEE Transactions on Biomedical Engineering*, vol. BME-33, no. 11, pp. 1029–1036, 1986.
- [31] S. Standring, *Gray’s Anatomy, The Anatomical Basis of Clinical Practice, Expert Consult , 40th Edition*. Elsevier, 2008.
- [32] E. G. Grant, C. B. Benson, G. L. Moneta, A. V. Alexandrov, J. D. Baker, E. I. Bluth, B. A. Carroll, M. Eliasziw, J. Gocke, B. S. Hertzberg, S. Katarick, L. Needleman, J. Pellerito, J. F. Polak, K. S. Rholl, D. L. Wooster, and E. Zierler, “Carotid artery stenosis: grayscale and Doppler ultrasound diagnosis–Society of Radiolo-

- gists in Ultrasound consensus conference.” in *Ultrasound quarterly*, vol. 19. Lippincott Williams & Wilkins, 2003, pp. 190–198.
- [33] P. R. Hoskins, K. Martin, and A. Thrush, *Diagnostic Ultrasound Physics and Equipment*, 2nd ed. Cambridge: Cambridge University Press, 2010.
- [34] C. Fahrion, R. Barg, and Mayfield Rob, “Vascular & Endovascular Surgery - Carotid Ultrasound.” [Online]. Available: <https://vascular.surgery.ucsf.edu/conditions--procedures/carotid-ultrasound.aspx>
- [35] C. H. McCollough, S. Leng, L. Yu, and J. G. Fletcher, “REVIEW: Dual-and Multi-Energy CT McCollough et al,” *Radiology*, vol. 276, no. 3, pp. 637–653, 2015.
- [36] L. Blanks and D. D. Boxer, “CT scan — Health Information — Bupa UK.” [Online]. Available: <https://www.bupa.co.uk/health-information/your-appointment/ctscan>
- [37] D. I. Tudor, S. D. Pastrama, and A. Hadar, “The use of computed tomography and ultrasonic imaging for assessment of defects in plates made of a polyester resin,” *Engineering Transactions*, vol. 62, no. 1, pp. 17–31, 2014.
- [38] M. Kvet and K. Matiaszko, “Epsilon temporal data in MRI results processing,” in *The 10th International Conference on Digital Technologies 2014*. IEEE, 7 2014, pp. 198–206.
- [39] K. Budidha, “In vivo investigations of photoplethysmograms and arterial oxygen saturation from the auditory canal in conditions of compromised peripheral perfusion by,” Ph.D. dissertation, City, University of London, 2016.
- [40] T. Tamura, Y. Maeda, M. Sekine, and M. Yoshida, “Wearable Photoplethysmographic Sensors Past and Present,” *Electronics*, vol. 3, no. 2, pp. 282–302, 2014.
- [41] C. Corciova, M. Turnea, and A. Salceanu, “A measurement system for the blood flow in peripheral territory,” *International Conference on E-Health and Bioengineering*, vol. 3, no. 4, pp. 1–4, 2011.

- [42] T. H. Huynh, R. Jafari, and W. Y. Chung, “Noninvasive Cuffless Blood Pressure Estimation Using Pulse Transit Time and Impedance Plethysmography,” *IEEE Transactions on Biomedical Engineering*, vol. PP, no. c, p. 1, 2018.
- [43] S. H. Liu, D. C. Cheng, and C. H. Su, “A Cuffless Blood Pressure Measurement Based on the Impedance Plethysmography Technique,” *Sensors (Basel, Switzerland)*, vol. 17, no. 5, pp. 1–13, 2017.
- [44] J. Malmivuo and R. Plonsey, *Bioelectromagnetism Principles and Applications of Bioelectric and Biomagnetic Fields*. Oxford University Press, 10 1995, no. November.
- [45] B. D. Nenova, I. T. Iliev, and A. Photoplethysmography, “Non-Invasive Methods of Peripheral Pulse Detection : Advantages and Disadvantages,” *Annual Journal of Electronics*, pp. 57–60, 2009.
- [46] S. Kahraman and M. Alber, “Electrical impedance spectroscopy measurements to estimate the uniaxial compressive strength of a fault breccia,” *Bulletin of Material Science*, vol. 37, no. 6, pp. 1543–1550, 2014.
- [47] D. S. Holder, *Electrical Impedance Tomography: Methods, History and Applications*. CRC Press, 2004.
- [48] B. Brown, “Electrical impedance tomography (EIT): a review,” *Journal of Medical Engineering & Technology*, vol. 27, no. 3, pp. 97–108, 2003.
- [49] X. B. Li, “Impedance Spectroscopy for Manufacturing Control of Material Physical Properties,” Ph.D. dissertation, University of Washington, 2003.
- [50] A. Lasia, “Electrochemical Impedance Spectroscopy and its Applications,” *Modern Aspects Of Electrochemistry*, vol. 32, pp. 143–248, 1999.
- [51] G. Xu, R. Wang, S. Zhang, S. Yang, G. a. Justin, M. Sun, and W. Yan, “A 128-electrode three dimensional electrical impedance tomography system,” *An-*

- nual International Conference of the IEEE Engineering in Medicine and Biology - Proceedings*, pp. 4386–4389, 2007.
- [52] P. B. Filho, “Tissue Characterisation using an Impedance Spectroscopy Probe,” Ph.D. dissertation, University of Sheffield, 2002.
 - [53] E. T. McAdams and J. Jossinet, “Tissue impedance: a historical overview.” *Physiological measurement*, vol. 16, no. 3 Suppl A, pp. A1–A13, 1995.
 - [54] C. Gabriel, S. Gabriel, and E. Corthout, “The dielectric properties of biological tissues: {I. Literature} survey,” *Physics in medicine and biology*, vol. 41, no. 11, p. 2231, 1996.
 - [55] A. K. Agrawal, Z. Grzebieniak, J. Rudnicki, E. Nienartowicz, J. Kibler, G. Marek, M. Masalski, and P. Zukrowski, “Impedance Tomography in Diagnosing Breast Cancer,” *Advances in Clinical and Experimental Medicine*, pp. 1313–1317, 2005.
 - [56] T. E. Kerner, K. D. Paulsen, A. Hartov, S. K. Soho, and S. P. Poplack, “Electrical impedance spectroscopy of the breast: Clinical imaging results in 26 subjects,” *IEEE Transactions on Medical Imaging*, vol. 21, no. 6, pp. 638–645, 2002.
 - [57] E. Malone, G. Sato Dos Santos, D. Holder, and S. Arridge, “Multifrequency Electrical Impedance Tomography using spectral constraints.” *IEEE transactions on medical imaging*, vol. 33, no. c, pp. 1–12, 2013.
 - [58] E. Barsoukov and J. R. Macdonald, *Impedance Spectroscopy: Theory, Experiment, and Applications*, 2nd ed. Hoboken, NJ, USA: John Wiley & Sons, Inc., 4 2005.
 - [59] A. D. Seagar, D. C. Barber, and B. H. Brown, “Theoretical limits to sensitivity and resolution in impedance imaging,” *Clinical Physics and Physiological Measurement*, vol. 8, no. 4A, pp. 13–31, 1987.
 - [60] A. Seagar, D. Barber, and B. Brown, “Electrical impedance imaging,” *IEE Proceedings A Physical Science, Measurement and Instrumentation, Management and Education, Reviews*, vol. 134, no. 2, p. 201, 1987.

- [61] E. Teschner, M. Imhoff, and S. Leonhardt, “Electrical Impedance Tomography: The realisation of regional ventilation monitoring 2nd edition,” no. 2, pp. 81–87, 9 2010.
- [62] C. Huang, F. Yu, P. Shih, and H. Chung, “Noise Reduction of Electrical Impedance Tomography via Movable Electrodes,” *Instrumentation Science & Technology*, vol. 35, no. 5, pp. 543–550, 2007.
- [63] S. C. Murphy and T. a. York, “Electrical impedance tomography with non-stationary electrodes,” *Measurement Science and Technology*, vol. 17, pp. 3042–3052, 2006.
- [64] M. Birkemose, A. J. Moller, M. L. Madsen, S. Brantlov, H. Sorensen, K. Overgaard, and P. Johansen, “Electrode placement in bioimpedance spectroscopy,” *Proceedings of the Annual International Conference of the IEEE Engineering in Medicine and Biology Society, EMBS*, pp. 3028–3031, 2013.
- [65] P. Linderholm and R. Schoch, “Microelectrical Impedance Tomography for Biophysical Characterization of Thin Film Biomaterials,” *The 12th International Conference on Solid State Sensors, Actuators, and Microsystems*, vol. 1, pp. 1–4, 2003.
- [66] M. O. Heuschkel, M. Fejtl, M. Raggenbass, D. Bertrand, and P. Renaud, “A three-dimensional multi-electrode array for multi-site stimulation and recording in acute brain slices,” *Journal of Neuroscience Methods*, vol. 114, pp. 135–148, 2002.
- [67] D. R. Merrill, M. Bikson, and J. G. Jefferys, “Electrical stimulation of excitable tissue: design of efficacious and safe protocols,” *Journal of Neuroscience Methods*, vol. 141, no. 2, pp. 171–198, 2005.
- [68] R. Bayford, “Bioimpedance Tomography (Electrical Impedance Tomography),” *Annual Review of Biomedical Engineering*, vol. 8, no. 1, pp. 63–91, 2006.
- [69] D. S. Holder, “Electrical impedance tomography (EIT) of brain function,” *Brain Topography*, vol. 5, no. 2, pp. 87–93, 1992.

- [70] a. J. Wilson, P. Milnes, a. R. Waterworth, R. H. Smallwood, and B. H. Brown, "Mk3.5: a modular, multi-frequency successor to the Mk3a EIS/EIT system." *Physiological measurement*, vol. 22, no. 1, pp. 49–54, 2001.
- [71] M. Grossi and B. Riccò, "Electrical impedance spectroscopy (EIS) for biological analysis and food characterization : a review," 2017.
- [72] F. Lu, C. Wang, R. Zhao, L. Du, Z. Fang, X. Guo, and Z. Zhao, "Review of stratum corneum impedance measurement in non-invasive penetration application," *Biosensors*, vol. 8, no. 2, 2018.
- [73] A. J. Bard and L. R. Faulkner, *Fundamentals and applications of needle trap devices*, 2nd ed., D. Harris, E. Swain, C. Roby, and E. Aiello, Eds. New York: John Wiley & Sons, Inc., 2001, vol. 2.
- [74] P. Hua, E. J. Woo, J. G. Webster, and W. J. Tompkins, "Using compound electrodes in electrical impedance tomography." *IEEE transactions on bio-medical engineering*, vol. 40, no. 1, pp. 29–34, 1993.
- [75] S. Minnikanti, "Implantable Electrodes with Carbon Nanotube Coatings," *Carbon Nanotubes on Electron Devices*, pp. 143–168, 2011.
- [76] "How Many Sensors Inside A Sports Smart Bracelet? April 6, 2015." [Online]. Available: http://webcache.googleusercontent.com/search?q=cache:http://blog.banggood.com/how-many-sensors-inside-a-sports-smart-bracelet-28536.html&gws_rd=cr&ei=lk43VomzFYuSaeCSi6gD
- [77] P. Kauppinen, J. Hyttinen, and J. Malmivuo, "Sensitivity Distribution Visualizations of Impedance Tomography Measurement Strategies," *International Journal of Bioelectromagnetism*, vol. 8, 2006.
- [78] T. Keller and A. Kuhn, "Electrodes for transcutaneous (surface) electrical stimulation," *Journal of Automatic Control*, vol. 18, no. 2, pp. 35–45, 2008.

- [79] O. T. Ogunnika, S. B. Rutkove, H. Ma, P. M. Fogerson, M. Scharfstein, R. C. Cooper, and J. L. Dawson, "A portable system for the assessment of neuromuscular diseases with electrical impedance myography," *Journal of Medical Engineering & Technology*, vol. 34, no. 7-8, pp. 377–385, 10 2010. [Online]. Available: <http://www.tandfonline.com/doi/full/10.3109/03091902.2010.500347>
- [80] K. W. Meacham, R. J. Giuly, L. Guo, S. Hochman, and S. P. DeWeerth, "A lithographically-patterned, elastic multi-electrode array for surface stimulation of the spinal cord," *Biomedical Microdevices*, vol. 10, no. 2, pp. 259–269, 2008.
- [81] T. J. Denison, H. Versnel, M. Peckerar, and S. a. Shamma, "Multi-Electrode Array for Measuring Evoked Pote From Surface of Ferret Primary Auditory Torte," *Journal of Neuroscience Methods*, vol. 58, pp. 209–220, 1995.
- [82] A. Popovic-Bijelic, G. Bijelic, N. Jorgovanovic, D. Bojanic, M. B. Popovic, D. B. Popovic, A. Popović-Bijelić, G. Bijelić, N. Jorgovanović, D. Bojanić, M. B. Popović, and D. B. Popović, "Multi-field surface electrode for selective electrical stimulation," in *Artificial Organs*, vol. 29, no. 6, 2005, pp. 448–452.
- [83] D. A. Wagenaar, J. Pine, and S. M. Potter, "Effective parameters for stimulation of dissociated cultures using multi-electrode arrays." *Journal of neuroscience methods*, vol. 138, no. 1-2, pp. 27–37, 2004.
- [84] A. Mercanzini, P. Colin, J.-C. Bensadoun, A. Bertsch, and P. Renaud, "In vivo electrical impedance spectroscopy of tissue reaction to microelectrode arrays." *IEEE transactions on bio-medical engineering*, vol. 56, no. 7, pp. 1909–1918, 2009.
- [85] F.-J. Pettersen and J. O. Høgetveit, "From 3D tissue data to impedance using Sim-pleware ScanFE+IP and COMSOL Multiphysics a tutorial," *Journal of Electrical Bioimpedance*, vol. 2, no. 1, pp. 13–32, 2011.
- [86] "COMSOL Multiphysics® Product Suite." [Online]. Available: <https://uk.comsol.com/products>

- [87] J. O. Wilkes, "Introduction to COMSOL Multiphysics," p. 168, 2009. [Online]. Available: <http://cdn.comsol.com/documentation/5.1.0.145/IntroductionToCOMSOLMultiphysics.pdf>
- [88] A. T. Mobashsher and A. M. Abbosh, "Artificial human phantoms: Human proxy in testing microwave apparatuses that have electromagnetic interaction with the human body," *IEEE Microwave Magazine*, vol. 16, no. 6, pp. 42–62, 2015.
- [89] D. Bennett, "NaCl doping and the conductivity of agar phantoms," *Materials Science and Engineering C*, vol. 31, no. 2, pp. 494–498, 2011.
- [90] Z. Q. Hashim, L. Constantinou, and I. F. Triantis, "Modelling Dynamically Re-Sizeable Electrodes (DRE) for Targeted Transcutaneous Measurements in Impedance Plethysmography," *IEEE Transactions on Biomedical Circuits and Systems*, vol. 14, no. 1, pp. 104–112, 2 2020. [Online]. Available: <https://ieeexplore.ieee.org/document/8931541/>
- [91] C. Gabriel, "Compilation of the Dielectric Properties of Body Tissues at RF and Microwave Frequencies," *Tech. Report, Dep. Physics, King's Coll. London*, vol. Report No., no. June, p. 21, 1996.
- [92] A. Seo, M. Rys, and S. Konz, "Measuring lower leg swelling: Optimum frequency for impedance method," *Medical and Biological Engineering and Computing*, vol. 39, no. 2, pp. 185–189, 2001.
- [93] F. A. Anderson, "Impedance plethysmography in the diagnosis of arterial and venous disease," *Annals of Biomedical Engineering*, vol. 12, no. 1, pp. 79–102, 1 1984.
- [94] T. J. Kao, G. J. Saulnier, D. Isaacson, T. L. Szabo, and J. C. Newell, "A versatile high-permittivity phantom for EIT," *IEEE Transactions on Biomedical Engineering*, vol. 55, no. 11, pp. 2601–2607, 2008.
- [95] S. Gabriel, R. W. Lau, and C. Gabriel, "The dielectric properties of biological

- tissues: III. Parametric models for the dielectric spectrum of tissues,” *Physics in Medicine and Biology*, vol. 41, no. 11, pp. 2271–2293, 11 1996.
- [96] J.-j. Huang, Y.-m. Huang, and A. R. See, “Velocity Using Bio-impedance Plethysmography and Regression Analysis,” *ECTI Transactions on Computer and Information Technology (ECTI-CIT)*, vol. 11, no. 1, pp. 63–70, 2017.
- [97] V. De Santis, V. Martynyuk, A. Lampasi, M. Fedula, and M. D. Ortigueira, “Fractional-order circuit models of the human body impedance for compliance tests against contact currents,” *AEU - International Journal of Electronics and Communications*, vol. 78, pp. 238–244, 2017.
- [98] R. Ivanic, I. Novotny, V. Rehacek, V. Tvarozek, and M. Weis, “Thin film non-symmetric microelectrode array for impedance monitoring of human skin,” *Thin Solid Films*, vol. 433, no. 1-2 SPEC., pp. 332–336, 2003.
- [99] J. Petrofsky, E. Schwab, M. Cúneo, J. George, J. Kim, A. Almalty, D. Lawson, E. Johnson, and W. Remigo, “Current distribution under electrodes in relation to stimulation current and skin blood flow: Are modern electrodes really providing the current distribution during stimulation we believe they are?” *Journal of Medical Engineering and Technology*, vol. 30, no. 6, pp. 368–381, 2006.
- [100] A. Lozano, J. Rosell, and R. Pallás-Areny, “Two-frequency impedance plethysmograph: real and imaginary parts,” *Medical & Biological Engineering & Computing*, vol. 28, no. 1, pp. 38–42, 1 1990.
- [101] S. Ray, J. Mukherjee, and S. Mandal, “Modelling nitrogen and carbon cycles in Hooghly estuary along with adjacent mangrove ecosystem,” 2015, pp. 289–320. [Online]. Available: <https://linkinghub.elsevier.com/retrieve/pii/B9780444635365000132>
- [102] Keysight, “Keysight E4980A/AL Precision LCR Meter,” 2017.
- [103] Z. Q. Hashim, L. Constantinou, P. A. Kyriacou, and I. F. Triantis, “A novel approach to transcutaneous localization of blood vessels using a dynamically

- reconfigurable electrode (DRE) array,” in *2016 IEEE Biomedical Circuits and Systems Conference (BioCAS)*, vol. 44, no. 0. IEEE, 10 2016, pp. 424–427. [Online]. Available: <http://ieeexplore.ieee.org/document/7833822/>
- [104] N. Otsu, “A Threshold Selection Method from Gray-Level Histograms,” *IEEE Transactions on Systems, Man, and Cybernetics*, vol. 9, no. 1, pp. 62–66, 1 1979. [Online]. Available: <http://ieeexplore.ieee.org/document/4310076/>
- [105] J. Yang and X. Li, “Boundary detection using mathematical morphology,” *Pattern Recognition Letters*, vol. 16, no. 12, pp. 1277–1286, 1995.
- [106] R. Gonzalez and R. Woods, *Digital Image Processing*, 4th ed. Pearson, 2017.
- [107] Y. R. Limbu, G. Gurung, R. Malla, R. Rajbhandari, and S. R. Regmi, “Assessment of carotid artery dimensions by ultrasound in non-smoker healthy adults of both sexes.” *Nepal Medical College journal : NMCJ*, 2006.
- [108] Primasil, “PR 610 / 60 Conductive Grade.”

Appendix A

Appendix A

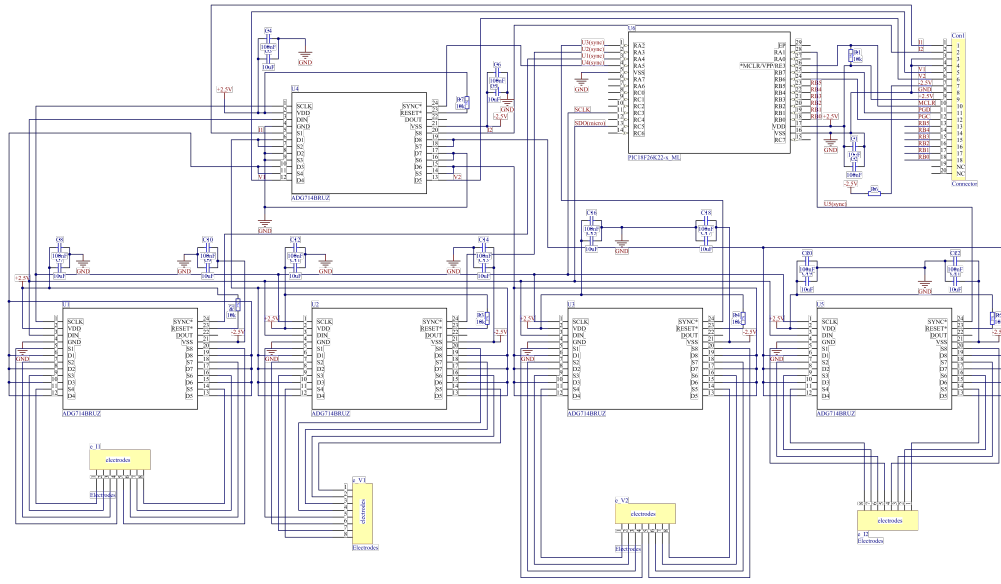


Figure A.1: Prototype 1 DRE electrode circuit design

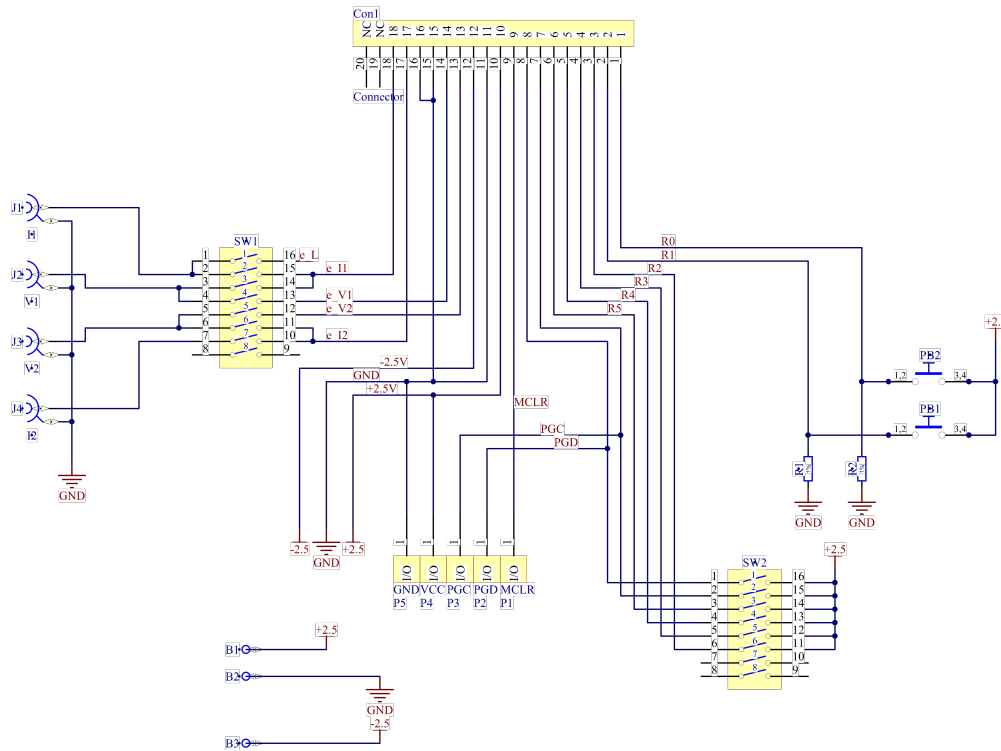


Figure A.2: Prototype 1 DRE user interface board circuit design

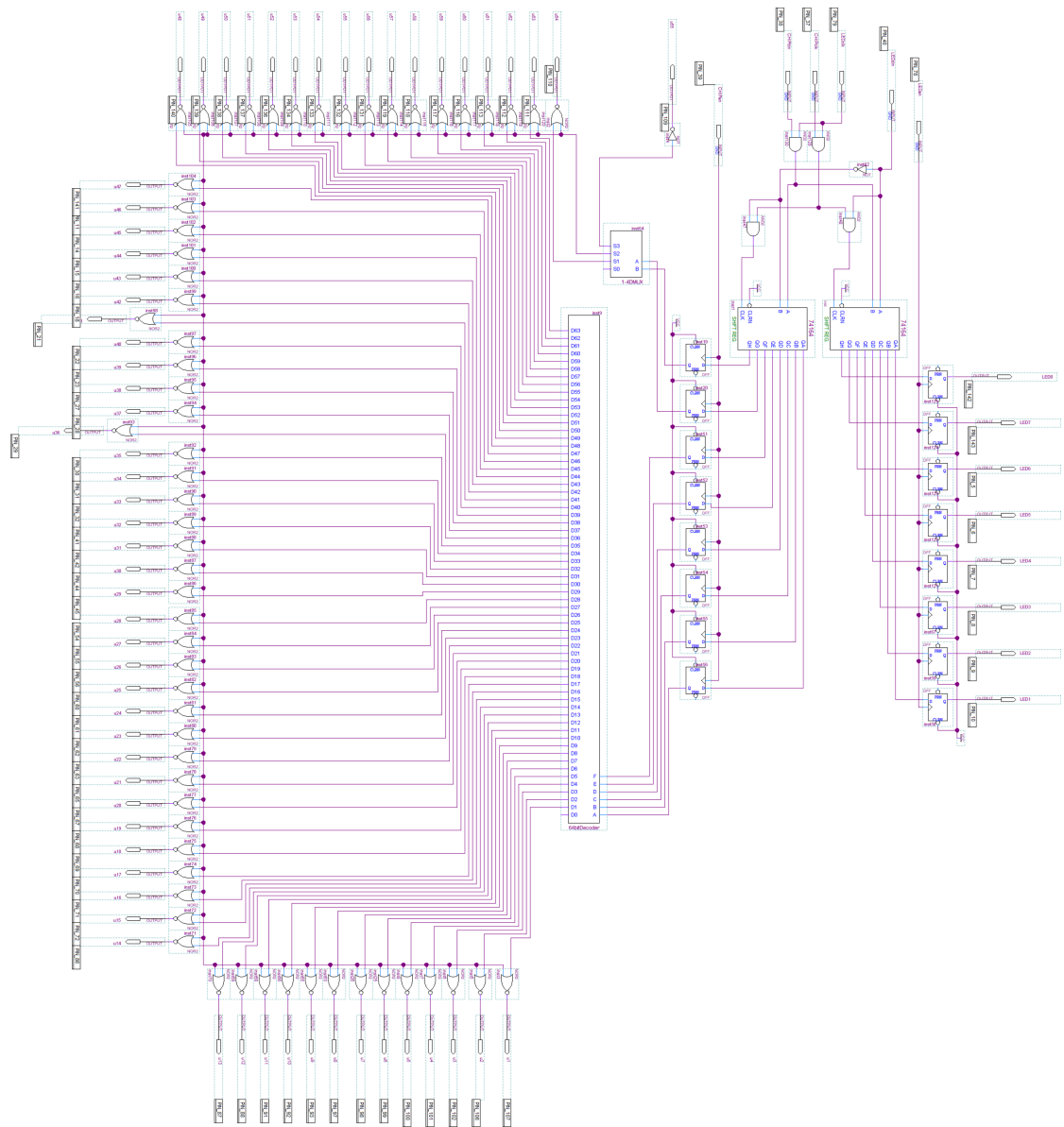


Figure A.3: Design for CPLD program.

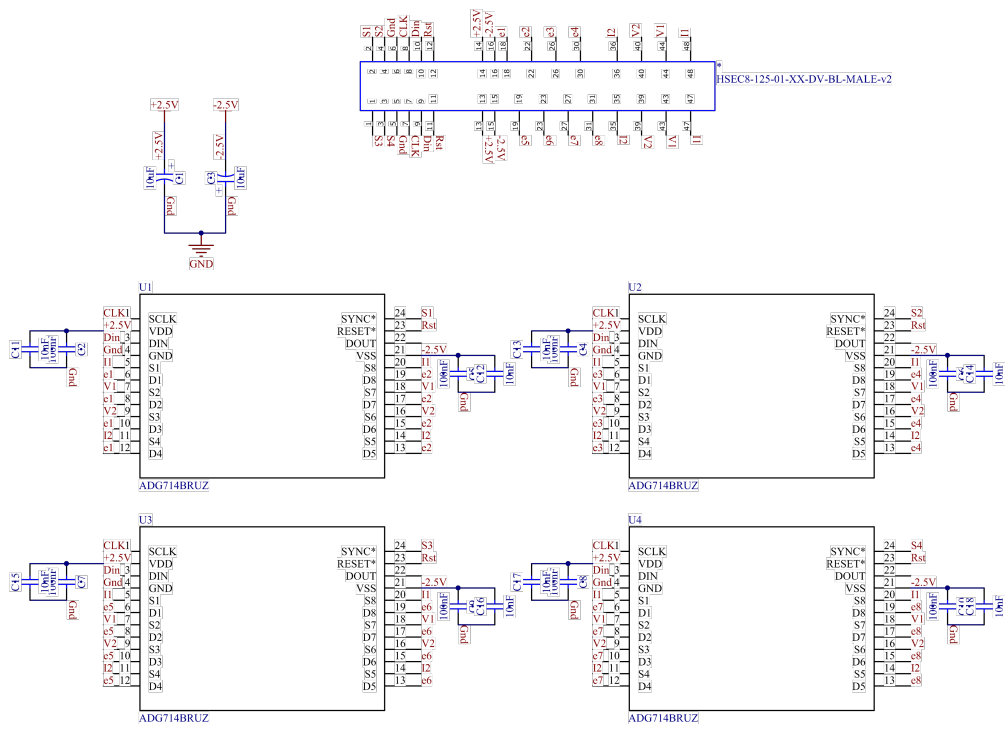


Figure A.4: IREM prototype 3 daughter board circuit design

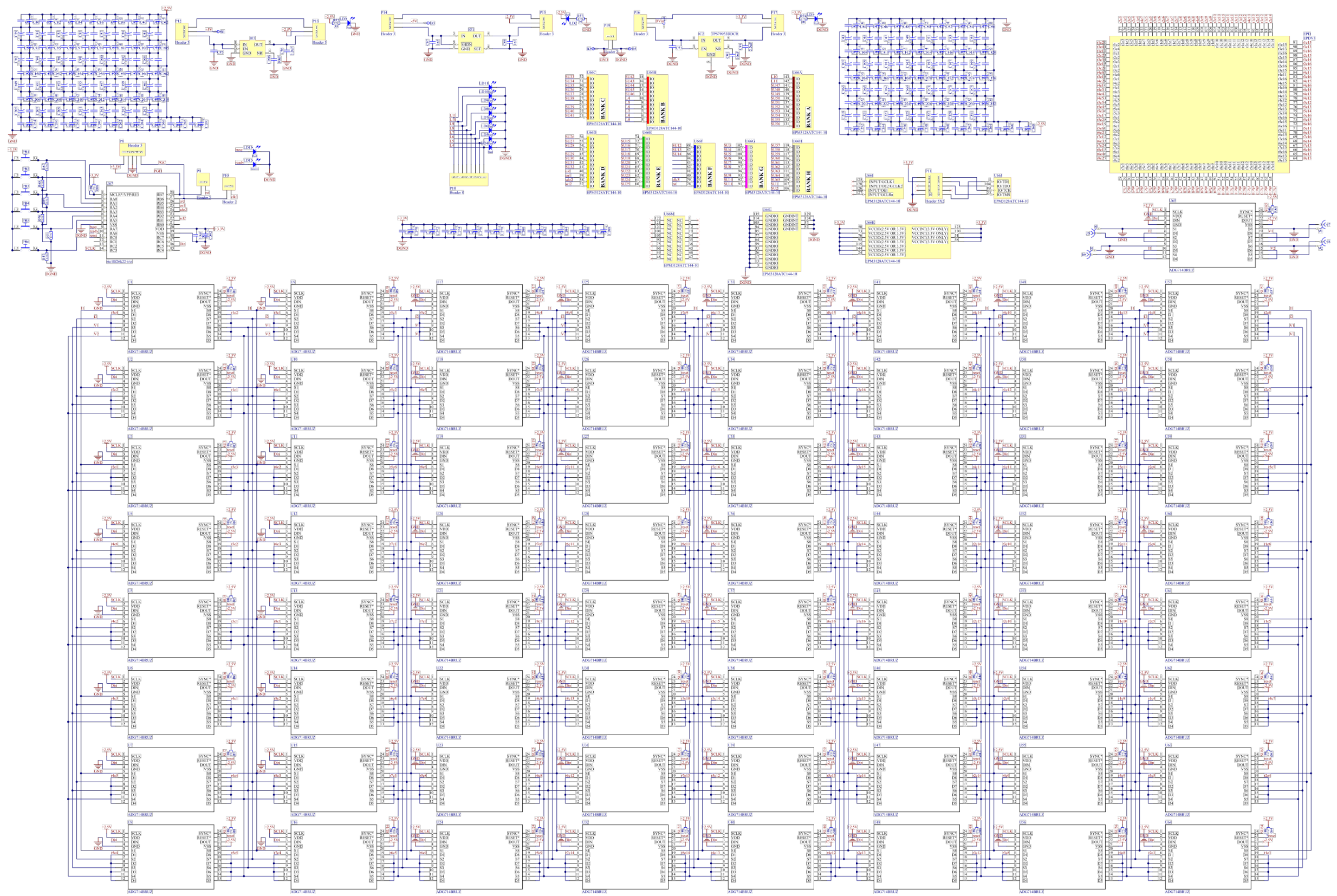


Figure A.5: IREM prototype 2 circuit design

Appendix B

Appendix B

B.1 MATLAB programs

B.1.1 LCR Data Accusation Program

```
function [ReZ, ImZ] = LCRtrig(freq, samples)
E4980A = visa('agilent',
'USB0::0x0957::0x0909::MY46309532::0::INSTR');
E4980A.InputBufferSize = 388608;
E4980A.ByteOrder = 'littleEndian';
fopen(E4980A);
fprintf(E4980A, sprintf(':TRIGger:SOURce_%s', 'HOLD'));
fprintf(E4980A, sprintf(':FUNctIon:IMPedance:TYPE_%s',
'RX'));
fprintf(E4980A, sprintf(':FREQuency:CW_%g', freq));
fprintf(E4980A, sprintf(':APERture_%s,%d', 'SHORT',
samples));
fprintf(E4980A, ':TRIGger:IMMediate');
C = textscan(query(E4980A, ':FETCh:IMPedance:CORRected?'),
'%f%f', 'Delimiter', ',');
ReZ = C{1};
```

```
ImZ = C{2};
```

```
fclose(E4980A);
```

```
delete(E4980A);
```

```
clear E4980A;
```

```
end
```

B.1.2 Prototype 1 Scan Program

```
segscanR = zeros(8,8);
```

```
segscanI = zeros(8,8);
```

```
for i=1:1:8
```

```
    for j = 1:1:8
```

```
        [ReZ,ImZ] = LCRtrig(10000,200)
```

```
        segscanR(j,i) = ReZ;
```

```
        segscanI(j,i) = ImZ;
```

```
        pause();
```

```
    end
```

```
end
```

```
Z = complex(segscanR, segscanI);
```

```
mag = abs(Z);
```

```
figure; imagesc(segscanR);
```

```
figure; imagesc(mag);
```

B.1.3 Pre-programmed sequence

```
% this programe is used to collect data from all scans and
```

```
% assign them to matrix and then post process them to get the
```

```
%thresholded data points
```

```

%a = arduino('COM4', 'Uno');
x = readDigitalPin(a, 'D2');
VReZ10K = zeros(8,13);
VImZ10K = zeros(8,13);
HReZ10K = zeros(5,16);
HImZ10K = zeros(5,16);
D1ReZ10K = zeros(5,13);
D1ImZ10K = zeros(5,13);
D2ReZ10K = zeros(5,13);
D2ImZ10K = zeros(5,13);
SVReZ10K = zeros(8,12);
SVImZ10K = zeros(8,12);
SHReZ10K = zeros(4,16);
SHImZ10K = zeros(4,16);
while x == 1
    x = readDigitalPin(a, 'D2');
end
while x == 0
    x = readDigitalPin(a, 'D2');
end
for vj = 1:1:13
    for vi = 1:1:8
        [ReZ10K, ImZ10K] = zaheer(10000, 10);
        VReZ10K(vi, vj) = ReZ10K;
        VImZ10K(vi, vj) = ImZ10K;
        while x == 1
            x = readDigitalPin(a, 'D2');
        end
    end
end

```

```

        while x == 0
            x = readDigitalPin(a, 'D2');
        end
        % pause(.01)
    end
end

for hj = 1:1:16
    for hi = 1:1:5
        [ReZ10K, ImZ10K] = zaheer(10000, 10);
        HReZ10K(hi, hj) = ReZ10K;
        HImZ10K(hi, hj) = ImZ10K;
        while x == 1
            x = readDigitalPin(a, 'D2');
        end
        while x == 0
            x = readDigitalPin(a, 'D2');
        end
        % pause(.01)
    end
end

for d1j = 1:1:13
    for d1i = 1:1:5
        [ReZ10K, ImZ10K] = zaheer(10000, 10);
        D1ReZ10K(d1i, d1j) = ReZ10K;
        D1ImZ10K(d1i, d1j) = ImZ10K;
        while x == 1
            x = readDigitalPin(a, 'D2');

```

```

        end
        while x == 0
            x = readDigitalPin(a, 'D2');
        end
        % pause(.01)
    end
end

for d2j = 1:1:13
    for d2i = 1:1:5
        [ReZ10K, ImZ10K] = zaheer(10000, 10);
        D2ReZ10K(d2i, d2j) = ReZ10K;
        D2ImZ10K(d2i, d2j) = ImZ10K;
        while x == 1
            x = readDigitalPin(a, 'D2');
        end
        while x == 0
            x = readDigitalPin(a, 'D2');
        end
        %pause(.01)
    end
end

for svj = 1:1:12
    for svi = 1:1:8
        [ReZ10K, ImZ10K] = zaheer(10000, 10);
        SVReZ10K(svi, svj) = ReZ10K;
        SVImZ10K(svi, svj) = ImZ10K;
        while x == 1

```

```

        x = readDigitalPin(a, 'D2');
    end
    while x == 0
        x = readDigitalPin(a, 'D2');
    end
    %pause(.01)
end
end

for shj = 1:1:15
    for shi = 1:1:4
        [ReZ10K, ImZ10K] = zaheer(10000, 10);
        SHReZ10K(shi, shj) = ReZ10K;
        SHImZ10K(shi, shj) = ImZ10K;
        while x == 1
            x = readDigitalPin(a, 'D2');
        end
        while x == 0
            x = readDigitalPin(a, 'D2');
        end
        %pause(.01)

    end
end

for shi=1:1:3
    [ReZ10K, ImZ10K] = zaheer(10000, 10);
    SHReZ10K(shi, 16) = ReZ10K;
    SHImZ10K(shi, 16) = ImZ10K;

```

```

    while x == 1
        x = readDigitalPin(a, 'D2');
    end
    while x == 0
        x = readDigitalPin(a, 'D2');
    end
    %pause(.01)
end

```

```

[ReZ10K, ImZ10K] = zaheer(10000, 10);
SHReZ10K(4,16) = ReZ10K;
SHImZ10K(4,16) = ImZ10K;
ExpProcess

```

B.1.4 Full Automation

```

%% loading electrode addresses and scanning sequence address
load('C:\Users\user\Documents\MATLAB\Arraymap.mat');

%% initialization serial port
s = serial('COM7');
s.InputBufferSize = 1;
s.ReadAsyncMode = 'continuous';
s.Baudrate = 9600;
s.StopBits = 2;
fopen(s);

%% initializing LCR meter
lcrmeterconnect;

```

```

%% Vertical scan
ss=1;
Vscanr=zeros(8,13);
Vscani=zeros(8,13);
for j = 1:13
    for i = 1:8
        sending(s,ss,VE1,VE2,VE3,VE4);
        fprintf(E4980A, ' :TRIGger:IMMediate ');
        C = textscan(query(E4980A, ' :FETCh:IMPedance:CORRected? '),
            '%f%f', 'Delimiter', ',',');
        Vscanr(i,j) = C{1};
        Vscani(i,j)= C{2};
        ss=ss+1;
    end
end

%% Horizontal scan
ss=1;
Hscanr=zeros(5,16);
Hscani=zeros(5,16);
for j = 1:16
    for i = 1:5
        sending(s,ss,HE1,HE2,HE3,HE4);
        fprintf(E4980A, ' :TRIGger:IMMediate ');
        C = textscan(query(E4980A, ' :FETCh:IMPedance:CORRected? '),
            '%f%f', 'Delimiter', ',',');
        Hscanr(i,j) = C{1};
        Hscani(i,j)= C{2};
        ss=ss+1;
    end
end

```



```

        end
    end

    %% Diagonal right scan
    ss=1;
    DRscanr=zeros(5,13);
    DRscani=zeros(5,13);
    for j = 1:13
        for i = 1:5
            sending(s,ss,DRE1,DRE2,DRE3,DRE4);
            fprintf(E4980A, ' :TRIGger:IMMediate ');
            C = textscan(query(E4980A, ' :FETCh:IMPedance:CORRected? '),
                '%f%f ', 'Delimiter ', ',');
            DRscanr(i,j) = C{1};
            DRscani(i,j)= C{2};
            ss=ss+1;
        end
    end

    %% Diagonal left scan
    ss=1;
    DLscanr=zeros(5,13);
    DLscani=zeros(5,13);
    for j = 1:13
        for i = 1:5
            sending(s,ss,DLE1,DLE2,DLE3,DLE4);
            fprintf(E4980A, ' :TRIGger:IMMediate ');
            C = textscan(query(E4980A, ' :FETCh:IMPedance:CORRected? '),
                '%f%f ', 'Delimiter ', ',');

```

```

        DLscanr(i , j) = C{1};
        DLscani(i , j)= C{2};
        ss=ss+1;
    end
end

%% combining
[Vr,Hr,DLr,DRr] = coordinate_scan(Vscanr,Hscanr,DLscanr,DRscanr);
[Vi,Hi,DLi,DRi] = coordinate_scan(Vscani,Hscani,DLscani,DRscani);
[NScanr]=imest(Hr,Vr,DLr,DRr);
[NScani]=imest(Hi,Vi,DLi,DRi);

%% terminating connections
lcrmeterdc
fclose(s); delete(s);

```

B.1.5 Sending function

```

function sending(s,ss,E1,E2,E3,E4)
    status = 'idle';
    fwrite(s,4,'int8','async');
    pause(0.05);
    out = s.TransferStatus;
    while out ~= status
        out = s.TransferStatus;
    end
    input = fread(s,1);
    if input ~= 136
        error('Error0.\condirm_not_received')
    end
end

```

```

end
fwrite(s,1,'int8','async');
pause(0.05)
out = s.TransferStatus;
while out ~= status
    out = s.TransferStatus;
end
input = fread(s,1);
if input == 136
    fwrite(s,ss,'int8','async');
    pause(0.05)
    out = s.TransferStatus;
    while out ~= status
        out = s.TransferStatus;
    end
else
    error('Error1._confirm_not_received')
end

if E1(ss,1)~=E2(ss,1)&&E1(ss,1)~=E3(ss,1)&&E1(ss,1)~=E4(ss,1)
    input = fread(s,1);
    if input == 136
        fwrite(s,2,'int8','async');
    else
        error('Error2._confirm_not_received')
    end
    pause(0.05)
    out = s.TransferStatus;
    while out ~= status

```

```

        out = s.TransferStatus;
    end
    input = fread(s,1);
    if input == 136
        fwrite(s,E1(ss,1),'int8','async');
    else
        error('Error3._confirm_not_received')
    end
    pause(0.05);
    out = s.TransferStatus;
    while out ~= status
        out = s.TransferStatus;
    end
    input = fread(s,1);
    if input == 136
        fwrite(s,3,'int8','async');
    else
        error('Error4._confirm_not_received')
    end
    pause(0.05);
    out = s.TransferStatus;
    while out ~= status
        out = s.TransferStatus;
    end
    input = fread(s,1);
    if input == 136
        if E1(ss,2)==1
            fwrite(s,0,'int8','async');
            pause(0.05);
        end
    end
end

```

```

        out = s.TransferStatus;
        while out ~= status
            out = s.TransferStatus;
        end
        input2=fread(s,1);
        if input2==136
            fwrite(s,1,'int8','async');
        else
            error('Error41._confirm_not_received')
        end
        pause(0.05);
        out = s.TransferStatus;
        while out ~= status
            out = s.TransferStatus;
        end
    else
        fwrite(s,8,'int8','async');
        pause(0.05);
        out = s.TransferStatus;
        while out ~= status
            out = s.TransferStatus;
        end
        input2=fread(s,1);
        if input2==136
            fwrite(s,0,'int8','async');
        else
            error('Error41._confirm_not_received')
        end
        pause(0.05);
    end
end

```

```

        out = s.TransferStatus;
        while out ~= status
            out = s.TransferStatus;
        end
    end
else
    error('Error5. _confirm_not_received')
end

elseif E1(ss,1)==E2(ss,1)&&E1(ss,1)~=E3(ss,1)&&E1(ss,1)~=E4(ss,1)
    input = fread(s,1);
    if input == 136
        fwrite(s,2,'int8','async');
    else
        error('Error2. _confirm_not_received')
    end
    pause(0.05);
    out = s.TransferStatus;
    while out ~= status
        out = s.TransferStatus;
    end
    input = fread(s,1);
    if input == 136
        fwrite(s,E1(ss,1),'int8','async');
    else
        error('Error3. _confirm_not_received')
    end
    pause(0.05);
    out = s.TransferStatus;

```

```

while out ~= status
    out = s.TransferStatus;
end
input = fread(s,1);
if input == 136
    fwrite(s,3,'int8','async');
else
    error('Error4. _confirm_not_received')
end
pause(0.05);
out = s.TransferStatus;
while out ~= status
    out = s.TransferStatus;
end
input = fread(s,1);
if input == 136
    if E1(ss,2)==1
        fwrite(s,4,'int8','async');
        pause(0.05);
        out = s.TransferStatus;
        while out ~= status
            out = s.TransferStatus;
        end
        input2=fread(s,1);
        if input2==136
            fwrite(s,1,'int8','async');
        else
            error('Error41. _confirm_not_received')
        end
    end
end

```

```

        pause(0.05);
        out = s.TransferStatus;
        while out ~= status
            out = s.TransferStatus;
        end
    else
        fwrite(s,8,'int8','async');
        pause(0.05);
        out = s.TransferStatus;
        while out ~= status
            out = s.TransferStatus;
        end
        input2=fread(s,1);
        if input2==136
            fwrite(s,2,'int8','async');
        else
            error('Error41. _confirm_not_received')
        end
        pause(0.05);
        out = s.TransferStatus;
        while out ~= status
            out = s.TransferStatus;
        end
    end
end
else
    error('Error5. _confirm_not_received')
end

elseif E1(ss,1)~=E2(ss,1)&&E1(ss,1)==E3(ss,1)&&

```



```

E1(ss,1)~=E4(ss,1)
    input = fread(s,1);
    if input == 136
        fwrite(s,2,'int8','async');
    else
        error('Error2._confirm_not_received')
    end
    pause(0.05);
    out = s.TransferStatus;
    while out ~= status
        out = s.TransferStatus;
    end
    input = fread(s,1);
    if input == 136
        fwrite(s,E1(ss,1),'int8','async');
    else
        error('Error3._confirm_not_received')
    end
    pause(0.05);
    out = s.TransferStatus;
    while out ~= status
        out = s.TransferStatus;
    end
    input = fread(s,1);
    if input == 136
        fwrite(s,3,'int8','async');
    else
        error('Error4._confirm_not_received')
    end
end

```

```

pause(0.05);
out = s.TransferStatus;
while out ~= status
    out = s.TransferStatus;
end
input = fread(s,1);
if input == 136
    if E1(ss,2)==1
        fwrite(s,2,'int8','async');
        pause(0.05);
        out = s.TransferStatus;
        while out ~= status
            out = s.TransferStatus;
        end
        input2=fread(s,1);
        if input2==136
            fwrite(s,1,'int8','async');
        else
            error('Error41: _confirm_not_received')
        end
        pause(0.05);
        out = s.TransferStatus;
        while out ~= status
            out = s.TransferStatus;
        end
    else
        fwrite(s,8,'int8','async');
        pause(0.05);
        out = s.TransferStatus;
    end

```

```

        while out ~= status
            out = s.TransferStatus;
        end
        input2=fread(s,1);
        if input2==136
            fwrite(s,4,'int8','async');
        else
            error('Error41. _confirm_not_received')
        end
        pause(0.05);
        out = s.TransferStatus;
        while out ~= status
            out = s.TransferStatus;
        end
    end
else
    error('Error5. _confirm_not_received')
end

elseif E1(ss,1)~=E2(ss,1)&&E1(ss,1)~=E3(ss,1)&&E1(ss,1)==E4(ss,1)
    input = fread(s,1);
    if input == 136
        fwrite(s,2,'int8','async');
    else
        error('Error2. _confirm_not_received')
    end
    pause(0.05);
    out = s.TransferStatus;
    while out ~= status

```

```

        out = s.TransferStatus;
    end
    input = fread(s,1);
    if input == 136
        fwrite(s,E1(ss,1),'int8','async');
    else
        error('Error3._confirm_not_received')
    end
    pause(0.05);
    out = s.TransferStatus;
    while out ~= status
        out = s.TransferStatus;
    end
    input = fread(s,1);
    if input == 136
        fwrite(s,3,'int8','async');
    else
        error('Error4._confirm_not_received')
    end
    pause(0.05);
    out = s.TransferStatus;
    while out ~= status
        out = s.TransferStatus;
    end
    input = fread(s,1);
    if input == 136
        if E1(ss,2)==1
            fwrite(s,1,'int8','async');
            pause(0.05);
        end
    end
end

```

```

        out = s.TransferStatus;
        while out ~= status
            out = s.TransferStatus;
        end
        input2=fread(s,1);
        if input2==136
            fwrite(s,1,'int8','async');
        else
            error('Error41._confirm_not_received')
        end
        pause(0.05);
        out = s.TransferStatus;
        while out ~= status
            out = s.TransferStatus;
        end
    else
        fwrite(s,8,'int8','async');
        pause(0.05);
        out = s.TransferStatus;
        while out ~= status
            out = s.TransferStatus;
        end
        input2=fread(s,1);
        if input2==136
            fwrite(s,8,'int8','async');
        else
            error('Error41._confirm_not_received')
        end
        pause(0.05);
    end
end

```

```

        out = s.TransferStatus;
        while out ~= status
            out = s.TransferStatus;
        end
    end
else
    error('Error5. _confirm_not_received')
end

end

if E2(ss,1)~=E1(ss,1)&&E2(ss,1)~=E3(ss,1)&&
E2(ss,1)~=E4(ss,1)
    input = fread(s,1);
    if input == 136
        fwrite(s,2,'int8','async');
    else
        error('Error6. _confirm_not_received')
    end
    pause(0.05);
    out = s.TransferStatus;
    while out ~= status
        out = s.TransferStatus;
    end
    input = fread(s,1);
    if input == 136
        fwrite(s,E2(ss,1),'int8','async');
    else
        error('Error7. _confirm_not_received')
    end
end

```

```

end
pause(0.05);
out = s.TransferStatus;
while out ~= status
    out = s.TransferStatus;
end
input = fread(s,1);
if input == 136
    fwrite(s,3,'int8','async');
else
    error('Error8. _confirm_not_received')
end
pause(0.05);
out = s.TransferStatus;
while out ~= status
    out = s.TransferStatus;
end
input = fread(s,1);
if input == 136
    if E2(ss,3)==2
        fwrite(s,0,'int8','async');
        pause(0.05);
        out = s.TransferStatus;
        while out ~= status
            out = s.TransferStatus;
        end
        input2=fread(s,1);
        if input2==136
            fwrite(s,2,'int8','async');

```

```

        else
            error( 'Error41. _confirm_not_received ')
        end
        pause(0.05);
        out = s.TransferStatus;
        while out ~= status
            out = s.TransferStatus;
        end
    else
        fwrite(s,4,'int8','async');
        pause(0.05);
        out = s.TransferStatus;
        while out ~= status
            out = s.TransferStatus;
        end
        input2=fread(s,1);
        if input2==136
            fwrite(s,0,'int8','async');
        else
            error( 'Error41. _confirm_not_received ')
        end
        pause(0.05);
        out = s.TransferStatus;
        while out ~= status
            out = s.TransferStatus;
        end
    end
end
else
    error( 'Error9. _confirm_not_received ')
end

```



```

end

elseif E2(ss,1)~=E1(ss,1)&&E2(ss,1)==E3(ss,1)&&
E2(ss,1)~=E4(ss,1)
    input = fread(s,1);
    if input == 136
        fwrite(s,2,'int8','async');
    else
        error('Error6._confirm_not_received')
    end
    pause(0.05);
    out = s.TransferStatus;
    while out ~= status
        out = s.TransferStatus;
    end
    input = fread(s,1);
    if input == 136
        fwrite(s,E2(ss,1),'int8','async');
    else
        error('Error7._confirm_not_received')
    end
    pause(0.05);
    out = s.TransferStatus;
    while out ~= status
        out = s.TransferStatus;
    end
    input = fread(s,1);
    if input == 136
        fwrite(s,3,'int8','async');

```

```

else
    error( 'Error8. _confirm_not_received ' )
end
pause(0.05);
out = s.TransferStatus;
while out ~= status
    out = s.TransferStatus;
end
input = fread(s,1);
if input == 136
    if E2(ss,3)==2
        fwrite(s,2,'int8','async');
        pause(0.05);
        out = s.TransferStatus;
        while out ~= status
            out = s.TransferStatus;
        end
        input2=fread(s,1);
        if input2==136
            fwrite(s,2,'int8','async');
        else
            error( 'Error41. _confirm_not_received ' )
        end
        pause(0.05);
        out = s.TransferStatus;
        while out ~= status
            out = s.TransferStatus;
        end
    end
else

```

```

        fwrite(s,4,'int8','async');
        pause(0.05);
        out = s.TransferStatus;
        while out ~= status
            out = s.TransferStatus;
        end
        input2=fread(s,1);
        if input2==136
            fwrite(s,4,'int8','async');
        else
            error('Error41. \condirm \not \received')
        end
        pause(0.05);
        out = s.TransferStatus;
        while out ~= status
            out = s.TransferStatus;
        end
    end
else
    error('Error9. \condirm \not \received')
end

elseif E2(ss,1)~=E1(ss,1)&&E2(ss,1)~=E3(ss,1)&&
E2(ss,1)==E4(ss,1)
    input = fread(s,1);
    if input == 136
        fwrite(s,2,'int8','async');
    else
        error('Error6. \condirm \not \received')
    end
end

```

```

end
pause(0.05);
out = s.TransferStatus;
while out ~= status
    out = s.TransferStatus;
end
input = fread(s,1);
if input == 136
    fwrite(s,E2(ss,1),'int8','async');
else
    error('Error7. _confirm_not_received')
end
pause(0.05);
out = s.TransferStatus;
while out ~= status
    out = s.TransferStatus;
end
input = fread(s,1);
if input == 136
    fwrite(s,3,'int8','async');
else
    error('Error8. _confirm_not_received')
end
pause(0.05);
out = s.TransferStatus;
while out ~= status
    out = s.TransferStatus;
end
input = fread(s,1);

```

```

if input == 136
    if E2(ss,3)==2
        fwrite(s,1,'int8','async');
        pause(0.05);
        out = s.TransferStatus;
        while out ~= status
            out = s.TransferStatus;
        end
        input2=fread(s,1);
        if input2==136
            fwrite(s,2,'int8','async');
        else
            error('Error41. _confirm_not_received')
        end
        pause(0.05);
        out = s.TransferStatus;
        while out ~= status
            out = s.TransferStatus;
        end
    else
        fwrite(s,4,'int8','async');
        pause(0.05);
        out = s.TransferStatus;
        while out ~= status
            out = s.TransferStatus;
        end
        input2=fread(s,1);
        if input2==136
            fwrite(s,8,'int8','async');

```

```

        else
            error( 'Error41. _confirm_not_received ')
        end
        pause(0.05);
        out = s.TransferStatus;
        while out ~= status
            out = s.TransferStatus;
        end
    end
else
    error( 'Error9. _confirm_not_received ')
end

end

if E3(ss,1)~=E1(ss,1)&&E3(ss,1)~=E2(ss,1)&&
E3(ss,1)~=E4(ss,1)
    input = fread(s,1);
    if input == 136
        fwrite(s,2, 'int8 ', 'async ');
    else
        error( 'Error6. _confirm_not_received ')
    end
    pause(0.05);
    out = s.TransferStatus;
    while out ~= status
        out = s.TransferStatus;
    end
    input = fread(s,1);

```

```

if input == 136
    fwrite(s,E3(ss,1),'int8','async');
else
    error('Error7. \_confirm\_not\_received')
end
pause(0.05);
out = s.TransferStatus;
while out ~= status
    out = s.TransferStatus;
end
input = fread(s,1);
if input == 136
    fwrite(s,3,'int8','async');
else
    error('Error8. \_confirm\_not\_received')
end
pause(0.05);
out = s.TransferStatus;
while out ~= status
    out = s.TransferStatus;
end
input = fread(s,1);
if input == 136
    if E3(ss,4)==4
        fwrite(s,0,'int8','async');
        pause(0.05);
        out = s.TransferStatus;
        while out ~= status
            out = s.TransferStatus;

```

```

end
input2=fread(s,1);
if input2==136
    fwrite(s,4,'int8','async');
else
    error('Error41. _confirm_not_received')
end
pause(0.05);
out = s.TransferStatus;
while out ~= status
    out = s.TransferStatus;
end
else
    fwrite(s,2,'int8','async');
    pause(0.05);
    out = s.TransferStatus;
    while out ~= status
        out = s.TransferStatus;
    end
    input2=fread(s,1);
    if input2==136
        fwrite(s,0,'int8','async');
    else
        error('Error41. _confirm_not_received')
    end
    pause(0.05);
    out = s.TransferStatus;
    while out ~= status
        out = s.TransferStatus;

```



```

        end
    end
else
    error('Error9. \confirm\not\nreceived')
end

elseif E3(ss,1)~=E1(ss,1)&&E3(ss,1)~=E2(ss,1)&&E3(ss,1)==E4(ss,1)
    input = fread(s,1);
    if input == 136
        fwrite(s,2,'int8','async');
    else
        error('Error6. \confirm\not\nreceived')
    end
    pause(0.05);
    out = s.TransferStatus;
    while out ~= status
        out = s.TransferStatus;
    end
    input = fread(s,1);
    if input == 136
        fwrite(s,E3(ss,1),'int8','async');
    else
        error('Error7. \confirm\not\nreceived')
    end
    pause(0.05);
    out = s.TransferStatus;
    while out ~= status
        out = s.TransferStatus;
    end
end

```

```

input = fread(s,1);
if input == 136
    fwrite(s,3,'int8','async');
else
    error('Error8. _confirm_not_received')
end
pause(0.05);
out = s.TransferStatus;
while out ~= status
    out = s.TransferStatus;
end
input = fread(s,1);
if input == 136
    if E3(ss,4)==4
        fwrite(s,1,'int8','async');
        pause(0.05);
        out = s.TransferStatus;
        while out ~= status
            out = s.TransferStatus;
        end
        input2=fread(s,1);
        if input2==136
            fwrite(s,4,'int8','async');
        else
            error('Error41. _confirm_not_received')
        end
        pause(0.05);
        out = s.TransferStatus;
        while out ~= status

```

```

        out = s.TransferStatus;
    end
else
    fwrite(s,2,'int8','async');
    pause(0.05);
    out = s.TransferStatus;
    while out ~= status
        out = s.TransferStatus;
    end
    input2=fread(s,1);
    if input2==136
        fwrite(s,8,'int8','async');
    else
        error('Error41. _confirm_not_received')
    end
    pause(0.05);
    out = s.TransferStatus;
    while out ~= status
        out = s.TransferStatus;
    end
end
end
else
    error('Error9. _confirm_not_received')
end

end

if E4(ss,1)~=E1(ss,1)&&E4(ss,1)~=E2(ss,1)&&
E4(ss,1)~=E3(ss,1)
    input = fread(s,1);

```

```

if input == 136
    fwrite(s,2,'int8','async');
else
    error('Error6. _confirm_not_received')
end
pause(0.05);
out = s.TransferStatus;
while out ~= status
    out = s.TransferStatus;
end
input = fread(s,1);
if input == 136
    fwrite(s,E4(ss,1),'int8','async');
else
    error('Error7. _confirm_not_received')
end
pause(0.05);
out = s.TransferStatus;
while out ~= status
    out = s.TransferStatus;
end
input = fread(s,1);
if input == 136
    fwrite(s,3,'int8','async');
else
    error('Error8. _confirm_not_received')
end
pause(0.05);
out = s.TransferStatus;

```

```

while out ~= status
    out = s.TransferStatus;
end
input = fread(s,1);
if input == 136
    if E4(ss,5)==8
        fwrite(s,0,'int8','async');
        pause(0.05);
        out = s.TransferStatus;
        while out ~= status
            out = s.TransferStatus;
        end
        input2=fread(s,1);
        if input2==136
            fwrite(s,8,'int8','async');
        else
            error('Error41. _confirm_not_received')
        end
        pause(0.05);
        out = s.TransferStatus;
        while out ~= status
            out = s.TransferStatus;
        end
    else
        fwrite(s,1,'int8','async');
        pause(0.05);
        out = s.TransferStatus;
        while out ~= status
            out = s.TransferStatus;
    end
end

```

```

        end
        input2=fread(s,1);
        if input2==136
            fwrite(s,0,'int8','async');
        else
            error('Error41. _confirm_not_received')
        end
        pause(0.05);
        out = s.TransferStatus;
        while out ~= status
            out = s.TransferStatus;
        end
    end
else
    error('Error9. _confirm_not_received')
end
pause(0.05);
out = s.TransferStatus;
while out ~= status
    out = s.TransferStatus;
end
input = fread(s,1);
if input ~= 136
    error('Error9. _confirm_not_received')
end
end
end

```

B.1.6 Coordinate Scan Function

```

function [V,H,DL,DR]=coordinate_scan(V_in,H_in,DL_in,DR_in)
% elec=ones(8,16);

```

```

V=cell(8,13,3);
verscan1=0;
verscan2=[0 0];
verscan3=[0 0];
H=cell(5,16,3);
horscan1=0;
horscan2=[0 0];
horscan3=[0 0];
DL=cell(5,13,3);
DR=cell(5,13,3);
d11 = 0;
d12 = [0 0];
d13 = [0 0];
d21 = 0;
d22 = [0 0];
d23 = [0 0];
for i=1:8
    for j=1:13
        verscan1=V_in(i,j);
        verscan2=[i j+1];
        verscan3=[i j+2];
        V(i,j,:)= {verscan1 verscan2 verscan3};
    end
end

for i=1:5
    for j=1:16
        horscan1=H_in(i,j);
        horscan2=[i+1 j];

```

```

        horscan3=[i+2 j];
        H(i,j,:)= {horscan1 horscan2 horscan3};
    end
end
for i=1:5
    for j=1:13
        d11=DL_in(i,j);
        d12=[i+1 j+1];
        d13=[i+2 j+2];
        d21=DR_in(i,j);
        d22=[i+2 j+1];
        d23=[i+1 j+2];
        DL(i,j,:)= {d11 d12 d13};
        DR(i,j,:)= {d21 d22 d23};
    end
end
end
end

```

B.1.7 LCR meter connection function

```

E4980A = visa('agilent',
'USB0::0x0957::0x0909::MY46309532::0::INSTR');
E4980A.InputBufferSize = 388608;
E4980A.ByteOrder = 'littleEndian';
fopen(E4980A);
fprintf(E4980A, sprintf(':TRIGger:SOURce_%s', 'HOLD'));
fprintf(E4980A, sprintf(':FUNCtion:IMPedance:TYPE_%s', 'RX'));
fprintf(E4980A, sprintf(':FREQuency:CW_%g', 10000));
fprintf(E4980A, sprintf(':APERture_%s,%d', 'SHORT', 10));

```

B.1.8 LCR meter disconnection function


```

fclose (E4980A);
delete (E4980A);
clear E4980A;

```

B.1.9 Image estimation function

```

function [NScan]=imest(horizontal_scan , vertical_scan ,
diagonal_Left_scan , diagonal_Right_scan)

```

```

Hm=imped(horizontal_scan ,8 ,16);

```

```

%Produce a weight matrix as per distance
Wh=binmat(Hm,8 ,16 ,1);

```

```

%Arranging the values of the vertical scan
Vm=imped(vertical_scan ,8 ,16);

```

```

%Produce a weight matrix as per distance
Wv=binmat(Vm,8 ,16 ,1);

```

```

%Arranging the values of the DL scan
DLm=imped(diagonal_Left_scan ,8 ,16);

```

```

%Produce a weight matrix as per distance
Wdl=binmat(DLm,8 ,16 ,sqrt(2));

```

```

%Arranging the values of the DR scan
DRm=imped(diagonal_Right_scan ,8 ,16);

```

```

%Produce a weight matrix as per distance
Wdr=binmat(DRm,8 ,16 ,sqrt(2));

```

```

SSum=Wh.*Hm+Wv.*Vm+Wdl.*DLm+Wdr.*DRm;
WSum=Wh+Wv+Wdl+Wdr;

NScan1=zeros(8,16);
for i=1:8,
    for j=1:16,
        if WSum(i,j)~=0
            NScan1(i,j)=SSum(i,j)/WSum(i,j);
        end;
    end;
end;

%Exclude 1st/last row/column
NScan=NScan1(2:7,2:15);
%imshow(NScan,[]);
figure; imagesc(NScan);

end

```